A NEW LOOK AT THE PERIODIC TABLE

Fathi Habashi

As science advances, its laws become fewer but of greater scope. In this respect the Periodic Law, which is the basis of the Periodic Table, represents a major step in the progress of chemistry — it affords the natural classification of the elements. The Periodic Table was developed by chemists more than one hundred years ago as a correlation for the properties of the elements. With the discovery of the internal structure of the atom, it became recognized by physicists as a natural law. When the crystalline structure of solids was studied, the nature of the chemical bonds was understood, and the theory of metals was put forward, it became an essential tool not only for chemists and physicists, but for metallurgists as well. Of the 87 naturally occurring elements, 63, i.e., about three fourth are described as *metals*, 16 as *nonmetals*, and 9 as *metalloids*. Chemists should abandon numbering the groups in the Periodic Table and to give descriptive names instead.

* Corresponding Author
E-Mail: Fathi.Habashi@arul.ulaval.ca
[a] Department of Mining, Metallurgical, and Materials Engineering, Laval University, Quebec City, Canada

INTRODUCTION

Metals are the most common articles in everyday life; they are usually used in form of alloys, which are a combination of two or more metals. They are the basis of the metallurgical industry. Nonmetals, except carbon, are hardly used by an average person. Air, a mixture of nonmetals is known to exist but is not seen by people. Nonmetals are the basis of the chemical industry. Metalloids are the basis of advanced technology and the electronics industry (Figure 1). In the solid state metals are composed of crystals made of closely packed atoms whose outer electrons are so loosely held that they are free to move throughout the crystal lattice. This structure explains their mechanical, physical, and chemical properties.

Nonmetals include the inert gases[1], hydrogen, oxygen, nitrogen, fluorine, and chlorine, liquid bromine, and the solid elements carbon, sulfur, phosphorus, and iodine. These elements do not have the properties of a metal. Nonmetals except the inert gases readily share electrons. Their atoms are united together by covalent bond, i.e., atoms that share their outer electrons. They often form diatomic molecules such as H_2, Cl_2, N_2 or larger molecules such as P_4 and S_g, or giant molecules, i.e. a network of atoms of indefinitely large volume such as carbon in form of graphite or diamond.

Figure 1. The periodic table

Figure 2. Electronic configuration of the metals.

---

[1] Inert gases is a historical name for the group of gases starting with helium and ending with radon. They were until the 1960's considered inert when few compounds of xenon with fluorine were prepared.

Table 1. General characteristics of metals, metalloids, and nonmetals.

Metals	Metalloids	Nonmetals
Crystalline solids (except mercury) with metallic lustre	May be crystalline or amorphous sometimes have metallic lustre	Form volatile or non-volatile molecules having no metallic lustre
Do not readily share electrons, their vapours are monoatomic	Readily share electrons even in the elemental form	Readily share electrons; form diatomic, large or giant molecules; inert gases are monatomic
Exhibit electrical and thermal conductivity. Electrical resistance usually increases with increased temperature	Low electrical and thermal conductivity	Do not conduct electricity or heat. Electrical resistance decreases with increased temperature
Have high density and useful mechanical properties	Moderate density, no useful mechanical properties	Low density of no useful mechanical properties
Electropositive, form cations, e.g., Cu^{2+}, Na^+, etc.	Sometimes electropositive, sometimes electronegative	Electronegative, form anions, e.g., S^{2-}, Cl^-, etc.
Form basic oxides, e.g., CaO	Form acidic oxides	Form acidic oxides, e.g., SO_2
Deposit on the cathode during electrolysis	Deposit on the cathode	Deposit on the anode, e.g., O_2, Cl_2
Either form no compounds with hydrogen or form unstable compounds usually nonvolatile (metal hydrides)	Form stable compounds with hydrogen, e.g., AsH_3, H_2Se	Form stable compounds with hydrogen, usually volatile, e.g., NH_3, PH_3, H_2S, etc.

Metalloids have covalent bond like nonmetals, but have intermediate properties between metals and nonmetals. Table 1 summarizes the properties of metals, nonmetals, and metalloids.

CLASSIFICATION OF METALS

Since metals are those elements capable of losing electrons, therefore, they can be divided into typical, less typical, transition, and inner transition. This division is a result of their electronic structure (Figure 2).

Typical metals

These are the alkali metals, the alkaline earths, and aluminum. They have the following characteristics:

• They have an electronic structure similar to that of the inert gases with one, two, or three electrons in the outermost shell.

• They have single valency, i.e., they lose their outermost electrons in a single step.

• They are reactive, i.e., react readily with water and oxygen. The driving force for this reactivity is the inclination to achieve maximum stability by attaining the electronic structure of an inert gas. A reactive metal such as aluminum or magnesium may be used as a material of construction because of the protective oxide film that is formed rapidly on its surface.

• They form only colorless compounds.

• Within a certain vertical group the atomic radius increases with increasing atomic number because of the added electron shells.

• Within a certain vertical group the reactivity increases with increasing atomic number because of the ease with which the outermost electrons will be lost since they are further away from the nucleus. Thus cesium is more reactive than rubidium, and rubidium more than potassium, etc.

• With increasing charge on the nucleus, the electrostatic attraction for the electrons increases and the outermost electrons will not be easily lost hence the reactivity decreases. Thus magnesium is less reactive than sodium, calcium less than potassium, and so on.

• With increased electrostatic attraction for the electrons as a result of increasing charge on the nucleus, the size of the atom decreases. Thus, aluminum has a smaller radius than magnesium, and magnesium smaller than sodium.

• With decreased radius and increased atomic weight the atom becomes more compact, i.e. the density increases. Thus, aluminum has higher density than magnesium, and magnesium higher than sodium.

• They have appreciable solubility in mercury and form compounds with it except beryllium and aluminum.

Less typical metals

These metals are: copper, silver, gold, zinc, cadmium, mercury, gallium, indium, thallium, tin, and lead. They differ from the typical metals in that they do not have an electronic structure similar to the inert gases; the outermost shell may contain up to four electrons and the next inner shell contains 18 instead of 8 electrons as in the inert gas structure. As a result of their electronic configuration they are characterized by the following:

• The atomic radius is less than the corresponding typical metals in the same horizontal group because the presence of 18 electrons in one shell results in an increased

electrostatic attraction with the nucleus. Thus, the atomic radius of copper is less than potassium, silver less than rubidium, and gold less than cesium. However, the atomic radius increases with increased number of electrons in the outermost shell (which is contrary to the typical metals), i.e. the atomic radius of gallium is larger than that of zinc, and zinc is larger than copper. This is demonstrated in Figure 3: The atomic volume[2] of the typical metals decreases with increased atomic number while the reverse is true for the less typical metals. the reason for this is the shielding effect of the 18-electron shell, the increased repulsion of the additional electron in the outmost shell and that shell, and also the increased repulsion between the electrons themselves in that shell.
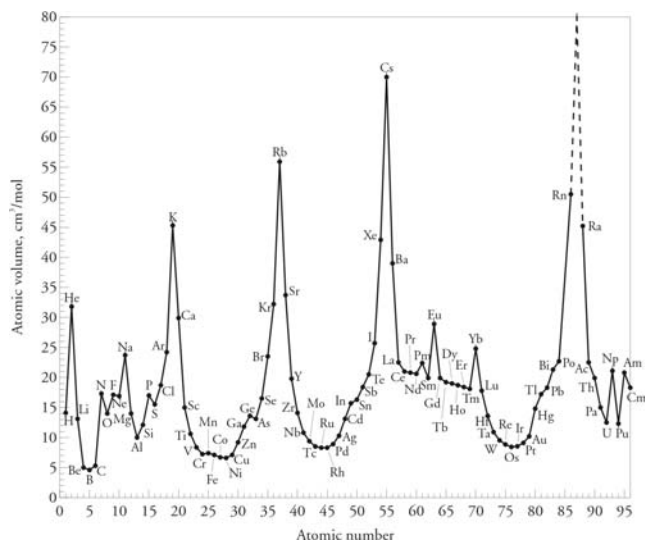

Figure 3. Atomic volume of elements.

• The outermost electrons will not be easily lost, i.e. these metals are less reactive than their corresponding typical metals for two reasons:

❍ There is no driving force to lose electrons since an inert gas electronic structure will not be achieved.

❍ There is a stronger electrostatic attraction due to the smaller atomic radius as compared to that of the typical metals.

• Because of the higher atomic weight and the smaller atomic radius these metals are more dense than their corresponding typical metals.

• Some of these metals show two different valency states, e.g., copper as Cu^{I} and Cu^{II}, gold as Au^{I} and Au^{III}, mercury as Hg^{I} and Hg^{II}, tin as Sn^{II} and Sn^{IV}, and lead as Pb^{II} and Pb^{IV}. This is because of the possibility of removing one or two electrons from the 18-electron shell.

---

[2]   Atomic volume is the volume in cubic centimeters occupied by one gram atomic weight of the element in the solid state. It can be used as qualitative guides to the relative volumes of the individual atoms since all gram atomic weights contain the same number of atoms.

• Few of these metals from colored ions in solution, e.g., Cu^{II} and Au^{III}, or colored compounds, e.g., copper sulfate pentahydrate (blue), cadmium sulfide (yellow), etc. (Table 2). This is due to the possibility of movement of electrons from the 18 electrons shell to a higher level.

• They have the highest solubility in mercury since their electronic structure is similar as that of mercury. Also, they do not form compound with mercury.

Table 2. Colour of the less typical metal ions in solution.

	M^{+}	M^{2+}	M^{3+}	M^{4+}
Cu	colourless	blue	—	—
Zn	—	colourless	—	—
Ga	—	—	colourless	—
Ag	colourless	—	—	—
Cd	—	colourless	—	—
In	—	—	colourless	—
Sn	—	colourless	—	colourless
Au	yellow	—	red	—
Hg	colourless	colourless	—	—
Tl	colourless	—	colourless	—
Pb	—	colourless	—	colourless

Transition metals

These are the metals in the vertical groups in the Periodic Table from scandium to nickel. They not only have electronic configuration different from the inert gases but they are characterized by having the same number of electrons in their outermost shell and a progressively greater number of electrons in the next inner shell. There are, however, some apparent irregularities in the number of electrons in the outermost electron shells. This is due to energy levels, which are determined from spectroscopic measurements. As their name implies the transition metals have properties between the typical and less typical metals.

They are less reactive than the typical metals because they will not achieve the inert gas structure when they lose their outermost electrons, but they are nevertheless more reactive than the less typical metals. They share the following properties:

❍ They resemble each other quite closely besides showing the usual group relationships because they have the same number of the outermost electrons.

❍ They may lose additional electrons from the next lower shell to form ions with higher charges. As a result they show a variable valence. For example, vanadium exists in +2, +3, +4, and +5 oxidation states, and titanium in +2, +3, and +4.

❍ The atomic radius of the successive metals in a certain horizontal period decreases slightly as the atomic number rises because when an electron is added to an inner shell it decreases slightly the size of the atom as a result of increased electrostatic attraction.

❍ Most of them form colored ions in solution due to electronic transition with the exception of the group Sc, Y, La and Ac that form only colorless compounds (Table 3).

Table 3. Colour of transition metal ions in solution. Incomplete list because many compounds are insoluble or when soluble, hydrolyse and precipitate

	M^{2+}	M^{3+}	MO^{2+}	MO_2^+	MO_2^{2+}
Sc	—	colourless	—	—	—
Ti	—	violet	colourless	—	—
V	violet	green	blue	yellow	—
Cr	blue	green	—	—	—
Mn	pink	violet	—	—	—
Fe	green	yellow	—	—	—
Co	red	blue	—	—	—
Ni	green	—	—	—	—
Y	—	colourless	—	—	—
Zr	—	—	colourless	—	—
Nb	—	—	—	colourless	—
Mo	—	red	green	blue	—
Ru	red	—	—	—	—
Rh	red	red	—	—	—
Pb	yellow	—	—	—	—
La	—	colourless	—	—	—
Hf	—	—	colourless	—	—
Ta	—	—	—	colourless	—
W	—	—	—	green	yellow
Re	—	red	—	—	—
Os	brown	green	red brown	—	—
Ir	—	yellow	brown	—	—
Pt	green	green-black	red, yellow	—	—

❍ They form many covalent compounds, e.g., the carbonyls of iron and nickel, the chlorides of titanium, and the oxyacids of chromium, molybdenum and tungsten.

❍ They form coordination compounds with ammonia, e.g., the ammines of cobalt and nickel.

❍ They mostly form borides, carbides, nitrides, and hydrides, which have mostly metallic character.

❍ They have the lowest solubility in mercury.

The transition metals can be divided into three groups:

• *Vertical transition metals*. These are the vertical groups scandium to manganese. They show similarity in the vertical direction, e.g., Zr-Hf, Nb-Ta, and Mo-W. The group Sc, Y, La, and Ac form colorless compounds and have the same valency (+3).

• *Horizontal transition metal*. This is the group iron, cobalt, and nickel. They show similarity in the horizontal direction.

- All three metals are ferromagnetic.

- Their carbides have intermediate properties between the metal-like character of the transition metals and the ionic character of the typical metals. Thus they have metallic luster and electrically conductive, but they are attacked by water and dilute acids.

- They form di- and trivalent compounds.

- They form carbonyls with CO.

- All three metals have nearly the same melting point (about 1500°C).

- All three metals occur in nature together in the native state in the minerals awariait, Fe(Ni,Co)₃, and josephinite, Fe(Ni,Co)₂.

• *Horizontal-vertical transition metals*. This is the platinum metals group where the similarity between the six metals is in the horizontal and vertical direction.

- They resist corrosion.

- They occur together in nature in the native state.

Inner transition metals

These metals have the same number of electrons in the two outermost shells but a progressively greater number of electrons in the next inner shell. They form two groups:

The lanthanides These are the metals between lanthanum and hafnium, namely cerium to lutenium (Figure 4). Although they have two electrons in the outermost shell, and one would expect that they would form divalent compounds, yet their most common valency state is three. This is one of the exceptions in the Periodic Table.

• Beside showing multiple valency they also form colored ions in solution (Table 4).

Figure 4. The actual position of lanthanides in the Periodic Table

Table 4. Colour of inner transition metal ions in solution

	M^{2+}	M^{3+}	M^{4+}	MO$_2$$^{2+}$
Ce	—	colourless	orange red	—
Pr	—	yellow green	—	—
Nd	—	red violet	—	—
Sm	red brown	pale yellow	—	—
Eu	—	pale pink	—	—
Gd	—	colourless	—	—
Lu	—	colourless	—	—
Yb	green	colourless	—	—
Tm	—	pale green	—	—
Er	—	rose	—	—
Ho	—	brownish yellow	—	—
Dy	—	pale yellow green	—	—
Tb	—	pale pink	—	—
Th	—	—	colourless	—
U	—	—	green	yellow
Pu	—	green	pink	—

• Being less reactive than the typical metals, they are so similar in chemical properties that their separation is usually done by making use of differences in physical properties.

• They form ionic carbides that decompose with water liberating hydrogen. However, these carbides have some metal like character, e.g., they have metallic luster and electrical conductivity.

• As in typical and transition metals, the atomic radius in the lanthanides gradually decreases from lanthanum to lutetium with the result that although the atomic radius of lanthanum is larger than that of yttrium, which is above it in the Table, the atomic radius of lutetium is smaller that of yttrium, i.e., La, Y, Lu. This is known as the "lanthanide contraction" and is responsible for the fact that the atomic radii of the metals lanthanum to mercury are nearly identical to those above them in the Table (Figure 5).

The actinides

These are the metals following actinium, namely thorium to lawrencium. Of this only thorium, uranium, and plutonium are of practical importance. In this group the 6d and 5f energy levels of electrons may be too close to each other which results

in cases where f-levels may be occupied in one atom but not in another. Uranium has multiple valency (+ 3, +4, +5, and +6) and form colored compounds; plutonium exists in +3 and +4 oxidation states and also forms colored compounds (Table 4).
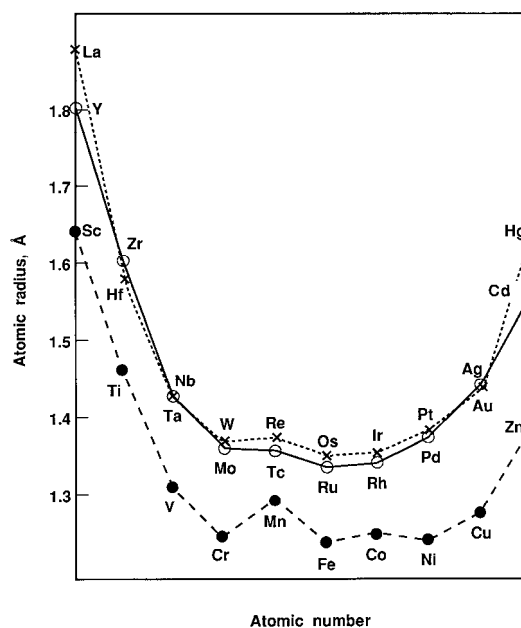

Figure 5. Lanthanide contraction. The lanthanides (metals between La and Hf) are not included in this chart.

• The actinides differ from the lanthanides by the fact that they can be readily separated one from the other by differences in the chemical properties while this is not the case with the lanthanides.

• They are similar to the lanthanides in forming ionic carbides with some metal-like behavior that decompose with water yielding hydrogen.

• While plutonium shows similarity to samarium, thorium and uranium differ much more than do cerium and neodymium. While thorium is like cerium in the tetravalent state, uranium is most stable in the hexavalent state. Thus they are, in this respect, more like transition metals than lanthanides. Plutonium is most stable in the tetravalent state, but also occurs in the +3 and +6 valent states.

• Americium and curium do show similarity and difficulty of separation comparable to the lanthanides.

DISCUSSION

Since its inception in 1869 by Mendeleev, the Periodic Table has undergone numerous changes (Table 5) and a large number of forms have been proposed.

IUPAC's Periodic Table

In 1985 the *International Union of Pure and Applied Chemistry* (IUPAC) recommended that the groups in the Periodic Table should be numbered from 1 to 18, i.e., the alkali metals are Group 1 and the inert gases are Group 18.[1,2] This numbering was a compromise between the North

American and the European Periodic Tables (Figure 6). But this raised a hot debate among chemists that was published in *Chemical & Engineering News* in a series of letters to the editor.[3-5] Almost all these letters opposed the new numbering system.

Figure 6. The Periodic Table according to IUPAC in an attempt to resolve the difference between European and North American nomenclature regarding the sub-groups

It is believed that this conflict may be resolved if chemists and physicists abandon the old idea of numbering the groups. Instead, it would be more reasonable to give names to each group of the elements that reflect their electronic structure, the nature of their bonding, and their properties (both physical and chemical). These names should be easier for students to remember and give them a deeper understanding of the Periodic Table. The present classification in ten groups (Figure 7) should be helpful in this respect. In this classification aluminum is moved to a position immediately next to magnesium so that the alkali metals, the alkaline earth metals, and aluminum form a group of typical metals. The other groups are: the less typical metals, the vertical transition metals, the horizontal transition metals, the vertical-horizontal transition metals, the inner transition metals (the lanthanides and the actinides), the metalloids, the monatomic nonmetals, and the covalent bond nonmetals.

Figure 7. A proposed Periodic Table without group numbers

An advantage of this classification would be putting each member of a group in its logical position. For example:

□ The group starting with boron and ending with thallium (Group 13 of the IUPAC notation) is in fact composed of three different groups: boron is a metalloid, aluminum is a typical metal, gallium, indium, and thallium are less typical metals.

□ The group starting with carbon and ending with lead (Group 14 of the IUPAC notation) is again composed of three different groups: Carbon is a nonmetal; silicon and germanium are metalloids while tin and lead are less typical metals.

There is a little advantage in keeping these two groups as Groups 13 and 14 (or III A and IVA) - - they have little in common. There is a great disparity in the melting points of the members of both groups. Similarly, the nitrogen and oxygen groups are a mixture of nonmetals and metalloids; the differences are more than the similarities. It would be advantageous to make this distinction. It would also be advantageous to identify the iron, cobalt, and nickel as a group, and the platinum metals as another group, instead of putting them in three vertical groups 8, 9 and 10.

The position of aluminum

Moving aluminum further away from gallium with which it occurs in bauxite may raise objection. However, it should be recalled that there are marked differences between both metals:

• While aluminum oxidizes so rapidly that it soon forms a non-porous protective layer, gallium does not.

• Gallium can be electrodeposited from aqueous solution, while aluminun cannot.

• $Al(OH)_3$ does not dissolve in ammonium hydroxide solution, but $Ga(OH)_3$, does dissolve.

• Gallium is precipitated from aqueous solution by H_2S as a sulfide; aluminum does not.

• Aluminum forms carbides, gallium does not.

• Aluminum carbide, Al_4C_3 is similar to the carbides of the first three groups, being ionic colorless compound containing the C_2^{2-} anion that decomposes in water. However, it liberates methane instead of acetylene like the other members of the group:

$$Al_4C_3 + 12\ H_2O \rightarrow 4\ Al(OH)_3 + 3\ CH_4$$
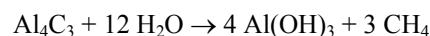
• Gallium forms a gaseous hybride, Ga_2H_6, while aluminum forms a white solid polymer hydride, $(AlH_3)_x$

• Historically, aluminum oxide was considered an earth like the rare earths and its fits with the scandium group.

• Mendeleev successfully predicted the properties of scandium before it was discovered by linking it with aluminum.

• The chemistry of scandium is very similar to that of aluminum and the ions Al^{3+}, Sc^{3+}, Y^{3+}, La^{3+}, and Ac^{3+} form a series similar to Mg^{2+}, Ca^{2+}, Sr^{2-}, Ba^{2+} and Ra^{2+}.

• Gallium is a typical dispersed element whose relative abundance in the Earth's crust is 1.5×10^{-3} %, aluminum is the third most abundant element with a relative abundance of 8.13 % (after oxygen and silicon).

Another objection, which may arise from this transfer, is the dissimilarity of the electron orbital structure of aluminum as compared to Sc, Y and La: aluminum has two s and one p electrons, while the others have two s and one d electrons. This objection can be answered in the following. The classification of the elements in the Periodic Table according to the population of electrons in the subshells, i.e., as s-, p-, d, and f-block elements does not indicate or explain many facts such as:

• The boron group elements are in the p-block but show different chemical and physical properties, e.g., boron is a metalloid while the other elements are metals. Further, the structure of boron hydroxide (boric acid) is fundamentally different from aluminum hydroxide. In the former no oxygen atoms are shared between the $M(OH)_n$ coordination groups in contrast to the latter.

• Boron group elements have three electrons in their outer shell: 2s and 1p. However, all three electrons are lost in one step except thallium and to a minor extent gallium. On the other hand the scandium group elements have also three electrons in their outer shell: 2s and 1 d, and all three are lost in one step. Hence the distinction in electron orbital is not a critical criterion for classification of the elements, and it is the total number of electrons that should be taken into consideration.

• The copper and zinc groups of elements are in the d-block which is used to be known as transition metals but differ from the other members of the same block in that the atomic radius increases with atomic number whereas in the other members it is the opposite. As a result they have different chemical properties and should not be included in the transition metals group.

• There are many irregularities in the electron orbitals in the subshells, which arises from quantum mechanical considerations. For example:

❍ Chromium and manganese, and molybdenum and technetium have the same number of d-electrons and different numbers of s-electrons instead of the reverse.

❍ Europium and gadolinium have similar f- and different d-electrons instead of the reverse.

This renders the strict adherence to the s-p-d, and f-classification pointless, and it should be better to consider the total number of electrons in a shell.

It should also be noted that this classification was introduced by physicists who are not necessarily interested in chemical properties.

CONCLUSIONS

Chemists should abandon numbering the groups in the Periodic Table, and to give the following descriptive names instead:

• Monatomic nonmetals

• Covalent nonmetals

• Metalloids

• Typical metals

• Less typical metals

• Transition metals with vertical similarity

• Transition metals with horizontal similarity (iron, cobalt, nickel)

• Transition metals with vertical and horizontal similarity (platinum group metals)

• Inner transition metals:

☐ The lanthanides

☐ The actinides

An advantage of this classification would be putting each member of a group in its logical position.

REFERENCES

[1]Anonymous, *Chem. Eng. News*, **1985**, February 4, pp. 26-27

[2]Rawls, R. L., *Chem. Eng. News*, **1986**, January 27, pp. 22-24

[3]Letters to the Editor, *Chem. & Eng. News* **1985**: February 25 pp. 4-5, March 11 pp. 4-5, March 18 p. 2, April 8 p. 5, April 22 p. 87, May 6 pp. 5 and 46, May 13 pp. 2 and 36, June 10 p. 4, August 5, pp. 4 and 47, August 12 pp. 2-3, August 19 p. 3

[4]Letters to the Editor, *Chem. Eng. News* **1986** January 27 p. 22, March 3 pp 3 and 46, March 17 p. 3, April 14 pp. 3 and 67, April 28 pp. 2 and 90, May 19 p. 2, June 23 p. 4, June 30 pp. 2 and 47, September 1 pp. 2-3, November 10 pp. 2 and 39

[5]Letters to the Editor, *Chem. Eng. News* **1987**, January 12 pp 3, 24, and 46, February 2 p. 3, April 6 p. 41

[6]Habashi, F., *Educ. Chem., (Bombay)*, **1994**, *11(2)*, 18–24

[7]Habashi, F., *Found. Chem.*, **2010**, *12(1)*, 31–39.

"METALLIC" BORON NITRIDE

R. Becker,[a] L. Chkhartishvili,[b,c]* R. Avci,[d] I. Murusidze,[e] O. Tsagareishvili[c] and N. Maisuradze[b]

Boron nitride shell structures of chemical composition BN_x with boron excess ($x << 1$) contaminated with carbon are synthesized in the process of melting of a boron-rich material in a boron nitride crucible with the nitrogen source in the form of high-purity pressed boron nitride rods, which held up the crucible. The obtained material is found to be conductive despite the fact that all the boron nitrides of stoichiometric chemical composition BN are insulators. "Metallic" boron nitride is modelled as a mixture of structural modifications of semiconducting boron and boron carbide heavily doped with nitrogen. First principle calculations performed within the quasi-classical approximation prove that nitrogen impurities, accommodated in large crystallographic voids characteristic of all-boron and boron-rich crystalline lattices, create donor electron-states inside the conduction band and then lead to the local "metallization" of chemical bonds in these initially covalently bonded structures.

* Corresponding Author
    E-Mail: chkharti2003@yahoo.com
[a] Boron Cluster Metamaterials, Cluster Sciences Research Institute, 39 Topsfield Rd., Ipswich, MA 01938, USA, ionsourcerer@mac.com, rbecker@clustersciences.com
[b] Department of Engineering Physics, Georgian Technical University, 77 M. Kostava Ave., Tbilisi 0175, Georgia, chkharti2003@yahoo.com, nmaisuradze@gtu.ge
[c] Laboratory for Boron & Powdered Composite Materials, F. Tavadze Institute of Metallurgy & Materials Science, 15 A. Kazbegi Ave., Tbilisi 0160, Georgia, chkharti2003@yahoo.com, t_otari@hotmail.com
[d] Department of Physics, Montana State University, Bozeman, MT 59717, USA, avci@physics.montana.edu
[e] Institute of Applied Physics, Ilia State University, 3/5 K. Cholokashvili Ave., Tbilisi 0162, Georgia, miv@iliauni.edu.ge

Introduction

Boron nitrides with the chemical formula BN, i.e. stoichiometric ratio of B : N = 1 : 1, can exist in various forms: diatomic molecule, plane fragments of a hexagonal sheet, nanotubes, fullerenes, hexagonal (h-BN), rhombohedral (r-BN), cubic (c-BN) and wurtzite-like (w-BN) crystals. It is well proved both experimentally and theoretically that all of them possess wide band or HOMO – LUMO gaps. Their chemical-bonding and electronic properties are well-studied. In particular, we have theoretically studied electronic structure of the BN diatomic molecule,[1] BN infinite hexagonal sheet,[2] and h-BN,[3] c-BN[4] and w-BN crystals[5] applying a quasi-classical-type method of calculation.

Boron nitride of composition BN is a chemical analogue of carbon. They are similar to each other and share similar structures of various dimensionality: hexagonal sheets and layered crystals, nanotubes and fullerenes, zinc blende and wutzite-like crystals. However, unlike carbon which can be metallic, BN is an insulator irrespective of its structure and dimensionality. Namely, 3D boron nitrides are known as wide band gap insulators what limits their application in electronics.

However, if some process (e.g. doping) could induce metallicity in these structures, then 3D BN would turn into a novel material with a potential for applications in electronics beyond conventional ceramics.

The possibilities of the intrinsic metallicity of BN were discussed in a few papers.

The high pressure room temperature phase transition in BN from the diamond-like insulating structure into the white-tin-like metallic structure was calculated for the first time in reference.[6] As for the recent calculations, it should be mentioned the density-functional-theory (DFT) study,[7] which has predicted that c-BN (111) nanofilms are metallic and turn into semiconductors once their thickness is too small. Note that such exceptional metallic behavior is not truly intrinsic, but due to a combined effect of thickness-dependent inbuilt electric polarization and labile near-gap states unique to polar nanofilms. On the basis of theoretical calculations, it has been proposed a dynamically stable tetragonal phase of BN which is metallic.[8] The analysis of its band structure, density of states, and electron localization function confirms the origin of the metallic behaviour to be due to the delocalized B $2p$ electrons.

By the DFT a series of 1D NFE (nearly-free-electron) bands of BN nanotubes with on-axis spatial distributions was also found.[9] These nanotubular states originate from the screening responsible for the image potential of the parent 2D BN sheets. When the nanotube radius exceeds the radial extent of NFE states, their energies converge to those of image potential states. The comparative DFT analysis in generalized-gradient-approximation (GGA) performed on electronic properties of BN single-walled zigzag nanotubes, as well as their BP and BAs analogues confirms[10] that, all these BN nanotubes are semiconducting in nature, whereas BP and BAs nanotubes are metallic up to some diameter. A superconductivity state was predicted[11] by Green's function approach in a zigzag BN nanotube within the extended attractive Hubbard model.

However, in most cases the metallicity of boron nitrides with the stoichiometric ratios of $B : N \approx 1 : 1$ must be related to point, dot-like or linear structural defects.

The DFT employing the local-spin-density-approximation (LSDA) was used[12] to show that increasing of the B-content relative to the N-content in BN nanoribbons, which are insulators, can significantly reduce the band gap making them semiconducting. In particular, armchair ribbons having excess of B-atoms were predicted to have a more stable triplet structure with a higher density-of-states (DOS) at the top of the valence band near the Fermi level. The influence of vacancies and substitutional defects on the electronic properties of h-BN in 2D molecular model was studied[13] using DFT at the level of local-density-approximation (LDA) and found that these point defects reduce the HOMO – LUMO energy gap.

Triangle-shaped nanohole, nanodot, and lattice antidot structures in h-BN monolayer sheets characterized with DFT calculations utilizing the LSDA[14] have revealed that N-terminated nanodots and antidots show half-metallicity. In spite of significant lattice contraction due to the presence of multiple holes, antidot superlattices were predicted to be stable, also exhibiting enhanced half-metallicity.

The synthesis of highly porous BN nanospheres with a rough surface consisting of open nanocones and corrugated ribbons has been described.[15] They exhibited surprisingly stable field emission properties at low turn-on voltages. These electron emission properties must be attributed to the presence of finite BN ribbons with zigzag edges which behave like metals as confirmed by first-principles calculations. They indicated that the work function associated to zigzag BN ribbons is lower when compared with BN-bulk material. Authors claimed that it was for the first time the possibility of finding a sort of metallic BN was reported. The theoretical evidence based on total-energy first-principles calculations of the existence of states and extended along the edges of bare zigzag BN-nanoribbons has been presented as well.[16] In particular, it was shown that there was a rich spectrum of electronic behaviors which could be controlled by applying an external electric field in order to obtain metallic ↔ semiconducting ↔ half-metallic transitions. The electronic structure calculations for the zigzag-edged BN nanoribbons by using DFT showed[17] that the ground states of the ribbons with an N-edge are half-metallic. According to the first-principles spin-polarized calculations,[18] the BN nanoribbons with topological line defects exhibit diverse electronic properties, including half-metallicity and half-semimetallicity, depending on the type of edge and line defect. Furthermore, an applied tensile strain can tune the half-semimetal gap. The comprehensive study[19] of the effects of line defects on electronic properties of monolayer BN sheets, nanoribbons, and single-walled nanotubes using first-principles calculations and Born–Oppenheimer quantum molecular dynamic (MD) simulation shows that although line defects divide the BN sheet (or nanotube) into domains they can lead to edges that significantly reduce the band gap. In particular, the line-defect-embedded zigzag BN nanoribbons with only N-terminated edges are predicted to be metallic at the ground state. The BN stereo-nanoribbons constructed by three BN ribbon wings connected via the junctions were investigated using first-principles calculations.[20] It was found that for the zigzag edges, the tri-wing BN nanoribbons can be metals or

narrow-band gap semiconductors depending on the bonding characteristics; the sp^3-bonding junctions even induce the metallic behaviors. However, it was also demonstrated,[21] using a combination of transmission-electron-microscopy (TEM) data and DFT calculations, that covalent interlayer bonds can be formed spontaneously at the edges of a h-BN bilayer resulting in subångström distortions of the atomic structure of the edge, and reconstruction of this closed edge can help the material to recover its bulk-like insulating behavior and thus disprove the predicted metallic character of open edges.

The metallicity of boron nitrides with the stoichiometric ratio of $B : N \approx 1 : 1$ also can be related to the impurities.

The first-principles investigation[22] of the electronic properties of BN nanoribbons having edges passivated by H-atoms showed that band gap for nanoribbons with armchair-shaped edges exhibited oscillations as their width increases. For the wider ribbons it converges to the constant value of 0.02 eV, while for nanoribbons with zigzag edges the band gap monotonically decreased and converged to the gap of 0.70 eV. Both these values are significantly smaller than the bulk gap due to the presence of the edge-states. Calculations of the electronic structure of H-terminated zigzag B-edged BN nanoribbons by using DFT even showed that their ground states are half-metallic. The intriguing electronic properties of fully and partially hydrogenated BN nanoribbons were investigated by means of first-principles computations.[23] Irrespective of ribbon width, fully hydrogenated zigzag BN nanoribbons were found to be metallic. The partially hydrogenated zigzag BN nanoribbons exhibit a semiconductor → half-metal → metal transition that occurs when the hydrogenated part is dominant. According to the electronic characteristics of fully hydrogenated BN layer and zigzag-edged BN nanoribbons investigated by using DFT, the zigzag-edged BN nanoribbon (prominently fabricated in experiments) possesses half-metallicity with full hydrogenation and this property can be tuned by applying a transverse electric bias.[24] Few-layer rippled h-BN membranes also exhibit[25] distinct and pronounced changes in their electronic properties after the atomic H-plasma treatment: the band gap reduced, which is a signature of transition from the insulating to the semiconducting regime.

By the DFT-based quantum mechanical description of the electronic properties of armchair BN nanoribbons edge-terminated with hydroxyl OH-groups or O-atoms, a reduction of band gap was observed.[26] On the other hand, standard spin-polarized DFT calculations[27,28] showed that unlike the semiconducting H-terminated zigzag BN nanoribbons, the O-terminated ones have two energetically degenerate ground states on the B-edge, both of which are metallic, and all the S-terminated zigzag BN nanoribbons also are metallic. The first-principles calculations[29] have revealed that an oxidized hexagonal monolayer of BN supported by a Cu substrate exhibits metallic properties when O adatom vertically bonds with the B atom. This is mainly due to the hybridization of the p orbital of the BN layer and O adatom around the Fermi level. Charge transfer from the Cu substrate to the O atom stabilizes the formation of the vertical O – B bond. Injecting negative charges could trigger the migration of the O adatom from the B – N bond to B atom for supported monolayer, which will lead to a metallic transition in the oxidized nanosheet.

DFT was utilized[30] to study the electronic properties BN sheets, taking into account the presence of defects. The structure considered consisted of a central hexagon surrounded by 3 alternating pentagons and 3 heptagons. To explore the effects of doping, B and N atoms were replaced with C atoms. When a B atom was replaced with a C atom, the new structure was a semimetal. Replacing two B atoms with two C atoms also yielded a semimetal. When three B or N atoms of the central hexagon were replaced with three C atoms, the new structure exhibited transition to a conductor, which however remained a semiconductor. Results of the study[31] on the effects of C-impurity doping on the DOS of the h-BN sheet within the random tight-binding model and Green's function technique also show that doping by C reduces the band gap of the BN system and, in high concentration of C-atoms, the DOS of BN plane becomes similar to that of graphene sheet, resulting in semimetallic behavior. Using DFT, as well as the Green's function quasi-particle approach, it was studied[32] the electronic structure of h-BN sheets doped with carbon and given the qualitatively correct picture of the substitutional impurity states in the gap.

The electronic structures and transport properties of fluorinated zigzag-edged BN nanoribbons were investigated by applying Green's function and DFT.[33] Results showed that the transition between half-metal and semiconductor can be realized by fluorination at different sites or by the change of the fluorination level. A comprehensive study[34] on the semi-fluorinated BN bilayers was presented using DFT calculations. Due to the combined effect of intrinsic intralayer strain and interlayer charge transfer, the ferromagnetic coupling is favored, which has to exhibit half-metallic behavior for BN bilayers. However, the h-BN nanosheets actually doped with F-atoms[35] via a facile chemical solution method with fluoboric acid, demonstrated a typical semiconductor characteristic.

By an investigation[36] of the electronic structure of alkali-doped BN nanotubes using DFT calculations, it was found that the NFE state couples with the alkali atom states, giving rise to metallic states near the Fermi level. Not only the s- but the d-orbital states substantially take part in the hybridization, and the resulting metallic states preserve the free-electron-like energy dispersion. The nodeless wave function at the Fermi level, together with the lowered work function, constitutes the major feature of the alkali-doped BN nanotubes. The electronic and structural properties of nanotubes composed of an iron oxide FeO monolayer and BN nanotubes were investigated[37] by means of a GGA implementation of DFT. Depending on the diameter of the tube, they can be semiconductors, half-metals or half-semimetals that can become half-metals if charged with either electrons or holes.

And finally, the metallicity of boron nitrides with the stoichiometric ratio of $B : N \approx 1 : 1$ can be related to the phase-inclusions of carbon.

According to the first-principles total-energy electronic-structure calculations performed within the LSDA[38] for hexagonally bonded honeycomb ribbons consisting of B, N, and C atoms, there are metallic BNC ribbons with different zigzag edges, C and BN or NB. The first-principles study[39] also suggested that hybrid C/BN nanoribbons with dihydrogenated edges can possess half-metallicity with a certain range of widths for the graphene and BN sections.

The hybrid C/BN nanoribbons can undergo the semiconductor-to-half-metal-to-metal transitions as the width of both graphene and BN nanoribbons increases. In particular, the dihydrogenation of the B-edge can induce localized edge states around the Fermi level, and the interaction among them can lead to the semiconductor-to-half-metal-to-metal transitions. The transport properties of hybrid nanoribbons formed by partially substituting zigzag BN (or graphene) nanoribbons into zigzag graphene (or BN) nanoribbons have been investigated using the first-principles nonequilibrium Green's function method.[40] The electrical transport was found to be highly improved with the transmission conductance around the Fermi level. The enhancement in these hybrid systems was attributed to the coupling effect between B (or N) atoms and C atoms at the interfaces, which introduces a pair of bonding and antibonding bands around the Fermi level. Based on a first-principle calculations it was also reported[41] the size limitation of half-metallic properties in hybrid zigzag BCN nanoribbons. Electronic properties of all hybrid systems are mainly determined by the C- rather than BN-segments. Transitions between semiconductor, half-metal and metal can be realized as the width of the carbon segment increases. Such atomic layers containing hybridized domains of graphene and h-BN, i.e. h-BNC, constitute a different type of disordered 2D electronic system. Magneto-electric transport measurements performed at low temperature in vapor phase synthesized h-BNC layers showed[42] a clear and anomalous transition from an insulating to a metallic behavior upon cooling. This transition can be modulated by electron- and hole-doping and by the application of an external magnetic field. These results supported by first principles calculations suggest that this transition in h-BNC is the result of the coexistence between percolation through metallic graphene networks and hopping conduction between edge states on randomly distributed insulating h-BN domains. Novel electronic properties of various-sized graphene nanoflakes embedded in a BN layer were also studied in ref.[43] In addition, it was found[44] that depending on the sizes of the h-BN triangular clusters embedded in graphene supercells and the separation region between them, the spin polarization can be induced through charge-doping. The half-metallicity is observed for certain charged states, which are otherwise metallic. In these half-metallic states, the spin density is concentrated near the edges of the clusters, in analogy to the more common predictions for h-BN/graphene intercalated nanoribbons. The first principles results of ref.[45] indicated that the heterostructures formed after C-fullerene coalescence in BN-nanotubes are metallic due to a core of corrugated C-nanotube, which provides an electron transport channel.

From the above short review one can conclude that there are a number of proposed models of metallic conductivity in boron nitrides with simple atomic structures and chemical formula BN, which are related to structural defects, impurities or phase-inclusions. However, these models fail to explain metallicity in boron-rich boron nitrides with complex clustered structures which are formed at very high temperatures.

In this work, we have obtained boron nitride of composition BN_x with boron excess, i.e. $x \ll 1$, which is conductive dispite the fact that all the boron nitrides of common stoichiometric composition BN are insulators. "Metallic" boron nitride is modeled as a mixture of different

structural modifications of semiconducting boron and boron carbide, i.e., a structure constructed from icosahedral and maybe small amount of some quasi-planar boron clusters, heavily doped with nitrogen. The calculations performed within the quasi-classical approximation have proved that nitrogen impurities accommodated in large crystallographic voids characteristic for all-boron and boron-rich lattices create electron donor states inside the conduction band and then lead to the local "metallization" of bonding.

Materials and Methods

In our experiments, high-purity pressed BN rods support the pyrolytic BN crucibles filled with powdered mixture of a metal oxide and boron (Figure 1). The crystalline boron used was of 99.999 % purity with trace contaminants being limited to water vapor and atmospheric gas adsorptions. The molten material was in full contact with the crucible for several hours during each synthesis run and even a day after the power was shut off, the crucible was still too hot. The mass of resulting polycrystalline boride was always certainly smaller than that of powder in the initial room-temperature crucible and fell out merely by inverting the crucible.

Figure 1. Crucible and its support before the melting runs.

Figure 2 shows the deposits which formed during several melting runs. There we are able to identify the badly eroded rods holding up the crucible, which however was attacked in much lesser extent. It must be due to the different degrees of structural imperfections in BN materials used in rods and crucible (like the graphite: high-purity pressed graphite easily reacts, but pyrolytic graphite does not): the crucibles material has a tiling structure which gives almost nothing for B to bind to.

It is obvious that in the presence of the B-vapor overflowing the pyrolytic BN crucible during the vacuum reduction of the charge material at temperature > 2050 °C, the highest-purity pressed BN rods (used to suspend the pyrolytic BN crucible in the optimum thermal position in the carbon-vacuum-furnace) is aggressively attacked by B-vapor from the reduction process.
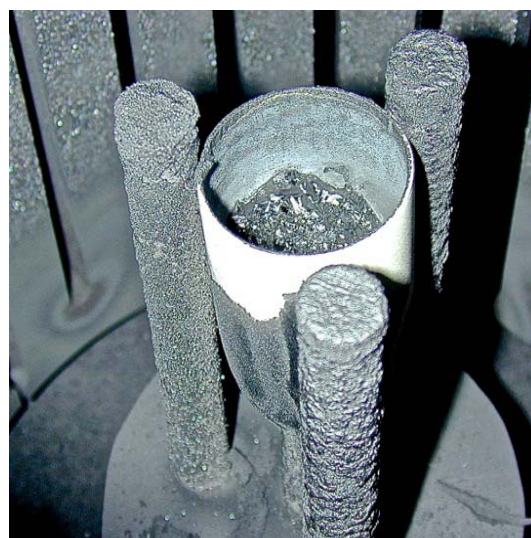

Figure 2. Deposits formed on rods and crucible during several melting runs.

As for the oxygen, it would have partially sublimated from the metal oxide at much lower temperatures and been pumped away by a turbo-molecular pump directly attached to the vacuum chamber (pumping efficiency was optimized at $\sim 10^{-6}$ Torr). However, rest of oxygen can evaporate, bonded with boron clusters and, therefore, their deposit should be contaminated with some oxygen as well. In a different case, when the crucible was machined from the same high-purity pressed BN as the rods, it was attacked by the molten boride too aggressively. Thus, pyrolytic BN was the material that more effectively resisted the thermo-chemical attack at such elevated temperatures.

After many subsequent melting runs, rods and crucible were covered with a paper-thin silicon-colored deposit (Figure 3).

Figure 3. Rods and crucible entirely covered with silicon-colored deposit.

The support rods can be used for melting runs until they are so reduced in diameter that they are no longer reliable: when erosion of rods is very intensive they are not able to support the crucible (Figure 4).

Figure 4. When erosion of rods is very intensive, they are unable to support the crucible.

We think that the irregular shells formed around the rods are some sort of BN_x, $x < 1$, compound. The reason for this conclusion is that the inside diameter of the shells is consistently similar to the original diameter of the pressed BN rods, while the diameter of the remainder of the rods diminished with each run – even though the shell fully enclosed the rods as they are progressively attacked. It would therefore appear to be the case that the thin BN_x shells grew thicker on the inner dimension layer by layer. Once the BN_x structure is established with the original BN rod surface reacting with excess B-vapor the structure is replicated on the inner surface as the BN_x shell gathers the dissociated nitrogen.

The specimens parted out from the obtained material were shiny on the outer surface, but matte black on the inner surface. It is perhaps because once the shell has sealed itself neither any gas can escape nor can be contaminated by residual gasses in the chamber.

There are several experimental conditions which should be properly analyzed to clarify the mechanism of formation the material.

Every metal atom stays tightly covalently bound to at least one B atom at all times because the relationship between the boron atomic percentage and phase transition temperature. The most perfect boride polycrystalline sample grown in our experiments is shown in Figure 5a. But, as the boron atomic percentage reaches the critical range, the solid gets dramatically smaller (and almost amorphous) structure and the evaporation rate is so high that there is very little material left in the crucible compared to the normal synthesis runs. So, we can conclude that boride within the crucible preferentially donates the boron (not metal) component to the vapor. The ion spectra also did not show any clear metal peak or any obvious metal/boron

compounds (see below on our earlier mass spectrometric study of clusters produced by laser vaporization from boride target rod).

(a)

(b)

Figure 5. Most perfect polycrystalline sample grown (a) after and (b) before being removed from the crucible.

Note the white line at top edge of the crucible (Figure 5b) revealing perfectly unreacted clean surface of the BN crucible where full contact of molten material during phase change was constant. Highly reflective smooth band above the crystal would have been deposit of pure boron vapor. Irregular crystalline band at top of crucible is similar to material growing on BN support rods and other external surfaces – therefore probably indicates turbulence of overflowing B-vapor – ambient-N interface zone. The "cap" disk at top of a rod is identical to the samples tested (see below).

The pyrolytic BN, instead of graphite, crucible process was developed to reduce the carbon contamination problem. In our extreme experimental conditions – temperature > 2050 °C and pressure ~ 10^{-6} Torr – if there was any carbon present in crucible it would have reacted with the traces of oxygen and been pumped away in gaseous state as CO or CO_2. Nevertheless, the presence of carbon in product is logical since the vacuum furnace was constructed using ultra-purified graphite resistance-heating elements, and to get the crucible content to the melting point of ~ 2000 °C and over, the heating elements must have had surface temperature closer to the ~ 3000 °C – it was certainly white hot – what means intensive sublimation of carbon. There is also the fact that we had melted many times and obviously that the surface of the graphite heating-elements had reacted with considerable quantities of the generated boron vapor and the inner surface was covered with tiny hemispherical glassy irregularities – "beads" – which must have been some

sort of B/C compound and/or boron heavily doped with carbon. Such isolation should weaken this source of carbon contamination. On the other hand, there would be carbon in some form within the closed confines of the graphite fiber walls of the furnace insulation.

The reflectivity would indicate the reasonably planar polycrystalline morphology at the outer surface. This silicon-colored surface of the shell could only continue to accumulate boron due to the overflow of the B-fluid from the top of the crucible. So, it is probable that the outer surface mainly consists of condensed boron clusters. Figure 6 shows the typical microstructure of such surfaces.
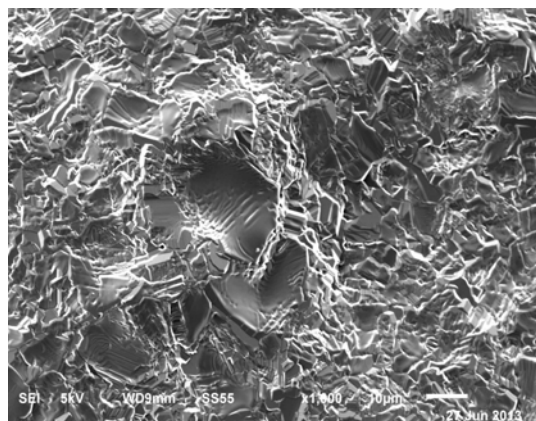
Figure 6. Outer surface microstructure of a shell.

As for the inner surface, it would have grown inwards, i.e. towards the BN rod, which would be dissociating in essentially pure nitrogen and boron vapor with almost no gaseous convection effects from the chamber. However, because the rods would have some percentage of carbon contamination, and perhaps traces of oxygen and other residual gasses trapped in the pressing process, chemical composition of the product also would be more complex than simply BN_x. The source of the nitrogen is without question its reduction or "gettering" from the pressed BN rods and not from the pyrolytic BN crucible because at base pressure of $\sim 10^{-6}$ Torr in the chamber any external source of nitrogen would be in the ppm range and therefore not a contributing factor. The microstructure of an inner surface is shown in Figure 7. In the most part, material is built up from loosely fused droplets (Figure 8). But, there are also presented threads (Figure 9) and flakes (Figure 10).
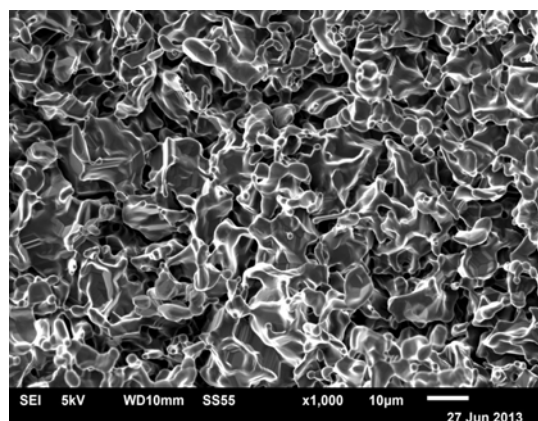

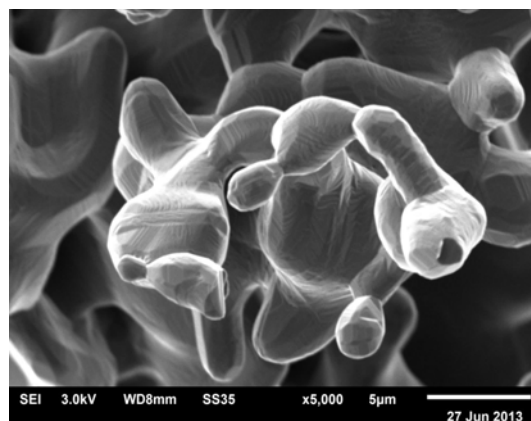**Figure 7.** Inner surface microstructure of a shell.

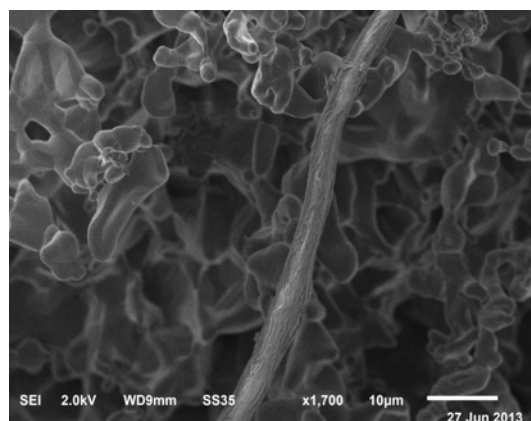**Figure 8.** Microstructure built up from loosely fused droplets.

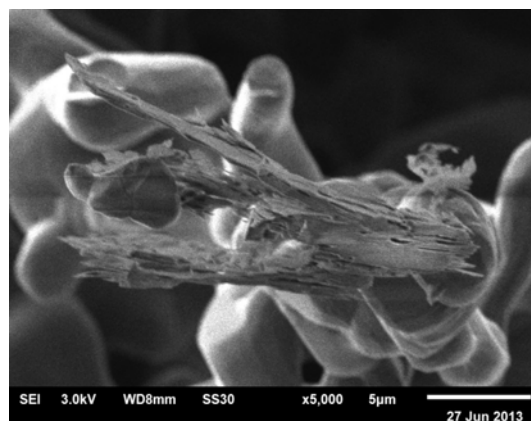**Figure 9.** Thread presented in microstructure.

**Figure 10.** Flakes presented in microstructure.

Note that material with almost of similar structure can be observed in other process, when gaseous nitrogen is used, instead of argon, e.g., during an implanter run. Namely, such deposit was obtained on the front surface of the ion source arc chamber with the boride target-crystal at the opposite end from the filament. The nitrogen reactively sputtered the surface of this crystal and formed a very dense and extremely hard black deposit on the molybdenum sidewall. Typically it result was a mixture of various nano-allotropes.

One more alternative nitrogen source was related to the pressed BN dielectrics used instead of conical insulators behind the boride target designed for the filament and normally made from corundum.
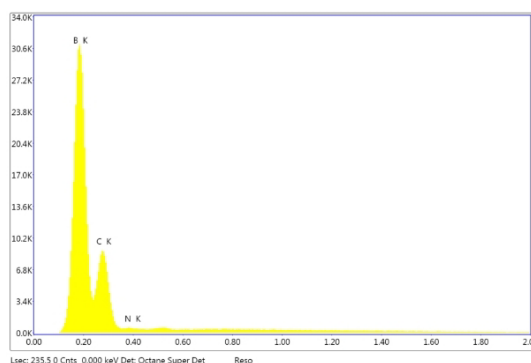
Chemical composition was analyzed for several different segments of shiny and dark surfaces. Examples of corresponding curves are presented in Figures 11 and 12. Figure 13 corresponds to the special case of fragments with flake-like structure.
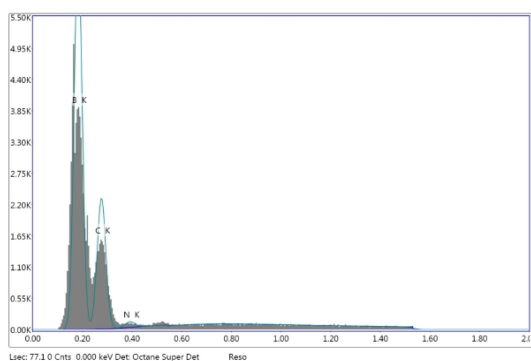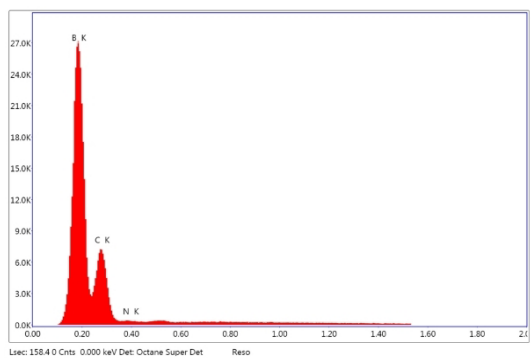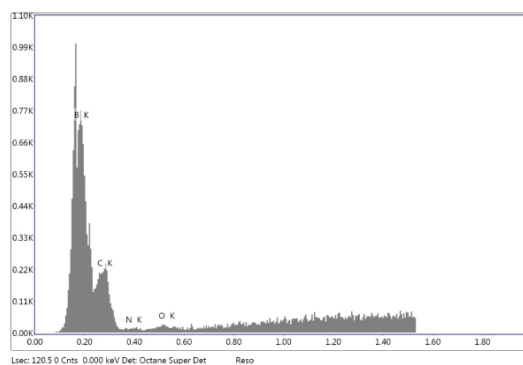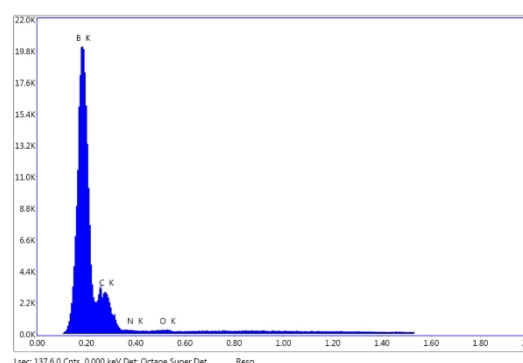

Figure 11. Chemical composition of a fragment of outer shell-surface: (a) unallocated, (b) B*K* / C*K* and (c) sum spectra.

Numerical results of such analysis are presented in Table 1. It shows that on outer surface elements are distributed almost homogeneously. There are presented mainly B and C. Concentration of N is relatively low. O and other trace elements are not detectable. As for the inner surface, it reveals essentially inhomogeneous distribution of chemical elements. Concentrations of B and C remain high, but at the same time concentration of N also reaches the significantly high level.
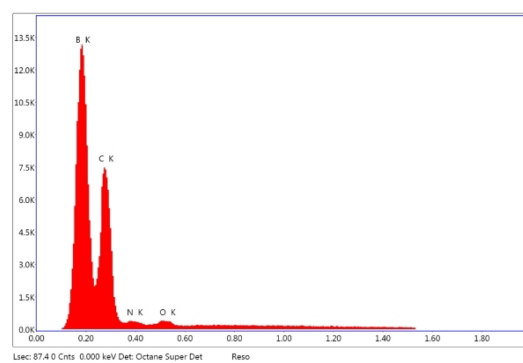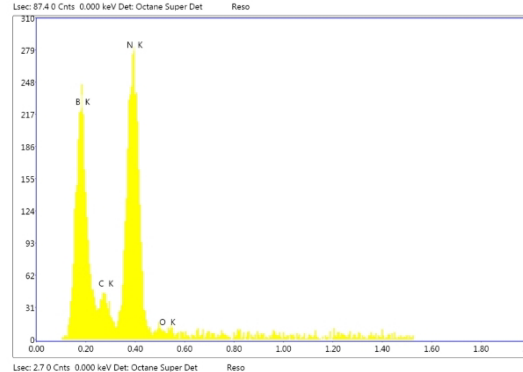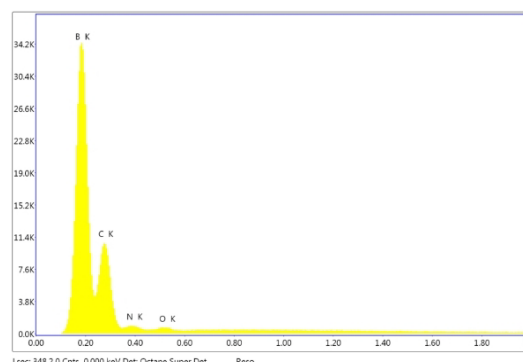

Figure 12. Chemical composition of a fragment of inner shell-surface: (a) unallocated, (b, c) B*K* / C*K*, (d) N*K* /B*K* / C*K*, and (e) sum spectra.

Now O is a detectable element. It should be emphasized that highest concentration of N is characteristic for flake-like microstructures: B 55.31, N 40.21 and C 4.48 atom %, respectively.
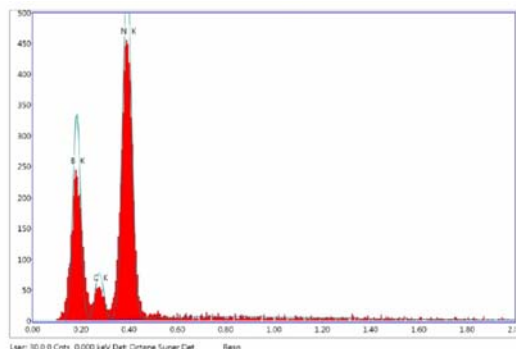

Figure 13. Chemical composition of flakes on inner shell-surface.

Because samples are thin polycrystalline structures, which are the most fragile material, it was extremely difficult to make rigorous electrical contact without turning them to dust. The probes used in electrical measurements were the brass spring-loaded hook-clips. However, even their pressure, necessary to get a reading, frequently destroyed such samples. It is a reason why we were only able to get momentary readings. Measured resistance R is in the range of $\sim 10^6\ \Omega$. Taking $R \sim 10^6\ \Omega$ and crude estimates for the geometry of experiment – distance between probes $l \sim 1$ cm, their diameter $d \sim 10^{-1}$ cm, and sample thickness $w \sim 10^{-2}$ cm, we can recalculate samples resistivity: $\rho = Rdw/l \sim 10^3\ \Omega$ cm, which is significantly lower if compared with the room temperature intrinsic resistivity of insulating boron nitrides, e.g. h-BN: $\sim 10^{13}\ \Omega$ cm, or even semiconducting boron modifications, e.g. ground-state β-rhombohedral modification $B_{\sim 105}$ (β-B): $\sim 10^7\ \Omega$ cm. Thus, obtained shells certainly are better conductive – "metallic" if compared with boron and boron nitride with chemical formula BN.

Table 1. Chemical composition of obtained shells in atom %.

Surface elements	Outer	Inner
B	85.66 – 88.57	55.31 – 91.00
N	00.34 – 00.67	00.01 – 40.21
C	11.09 – 13.57	04.48 – 18.15
O and other traces	00.00 – 00.00	00.00 – 00.77

One more argument of the "metallicity" is circuit shortening effect caused by shell fragments when they are placed on an insulating surface: after application of the wall voltage between pair of distant points on a shell fragment surface, the material is instantly vaporized with a blinding flash of light. This test was repeated many times on the two opposing surfaces and it was noted that when the electrodes touched the shiny side it was harder to initiate an arc and the arcs were not as intense as they were on the black side which was extremely sensitive, and vaporized more completely with a brighter flash. So, one can feel confident in saying that there is a clear difference in the electrical conductivity of the two surfaces: the black surface is definitely more conductive.

On the Positions of Nitrogen

We can state that, the synthesized shells mainly are consisted of boron.

As for the concentration of carbon, it is too high but less than the level of ~ 20 atom % characteristic of boron carbides with approximate chemical formula B_4C. Unit cell of a boron carbide $B_{12+x}C_{3-x}$, $0.1 < x < 1.7$, is similar to that of α-rhombohedral boron B_{12} (α-B), unless it contains additional $C-B-C$, $C-B-B$ or $B-B-B$ atomic chains along the largest diagonal of the elemental rhombohedron. Consequently, material has to contain fine crystals of α-B and maybe boron carbides of different chemical compositions (about properties of crystalline boron and its implications on boron carbides see reference[46]).

Apparently, the fine crystals of β-B have to be present as well. They can contain carbon not only segregated at grain boundaries, but also dissolved in lattice up to a few atom %. However, we do not expect interstitial doping of β-B with C as accommodation of carbon atoms inside the large crystallographic voids characteristic of β-B lattice is virtually impossible because carbon atoms easily substitute boron atom in too many regular sites leading to the contraction of interatomic chemical bonds.

And finally, as the material is synthesized at very high temperature the inclusions of amorphous phase of boron (a-B) are excluded. Material can contain only small regions of randomized structure in the form of an association of both icosahedral and (quasi)planar boron clusters enriched with carbon.

Thus, the synthesized shells can be imagined as a boron-based fine-structured multiphase system including α-B, β-B and traces of a-B doped with C, as well as boron carbides of different compositions. But, all these bulk phases are semiconducting. "Metallicity" of their mixture must be attributed to the presence of nitrogen with overly high concentrations. Consequently, we need to systemize here the data available on B/N systems for construction of the structural model describing position of N dopant atoms in the obtained material, which can be named as "boron-rich boron nitride."

B/N stoichiometries with B in excess

There are number of evidences that boron nitride molecules and clusters, fullerenes and nanotubes, as well as solid structures prefer the stoichiometries with boron in excess.

Optimum geometries and vibration spectra for different states of B_2N molecule were obtained by the Hartree–Fock (HF) method.[47] From a statistical thermodynamic analysis, B_2N is found to be extraordinarily stable up to very high temperatures, whereas nitrogen-rich species BN_2 dissociates spontaneously to $B + N_2$ at all temperatures. The BNB radical was generated[48] by the laser vaporization of solid BN and isolated noble gas matrices at helium temperatures. This radical also was indicated as an extraordinary stable linear species with the symmetric ground state, according to the calculation at the configuration-interaction (CI) level of the theory. The equilibriums involving the B_2N molecule has

been studied using the high-temperature Knudsen cell mass spectrometry.[49] The Green's function-based approach was employed[50] for direct and accurate calculations of the low-lying ionization potentials and electron affinities of the highly correlated close- and open-shell molecule B_2N and molecular ion B_2N^-.

The discovery of pristine boron clusters B_n, $n = 2 – 52$, formed by the laser-ablation of h-BN has been reported.[51] As for the mixed clusters of B and N, B_nN_m, an empirical interatomic potential can be introduced,[52] which is parameterized by means of the LDA results and allows a reliable description of their structures and energies. Such clusters were actually produced[53] by sputtering BN with Cs or Rb. The atom ordering in assumed linear species were deduced from measurements of the mass distribution of both the positive and negative products from the fragmentation of the anionic clusters in a gas target. The existence of several anions with B in excess including B_2N, B_3N, B_4N, and B_3N_2 were demonstrated. These clusters are believed to play an important role as precursors in the formation of boron nitride thin films, nanoparticles, nanotubes, and nanomesh. Gas-phase electronic spectra of some linear and cyclic B_nN_m radicals were measured in a supersonic molecular beam in the visible spectral region.[54] A novel set of stable graphite-like structures of B_nN_m ($n + m \leq 54$, $n = m$ or $n = m + 1$) clusters have been obtained theoretically.[55]

An efficient method was proposed[56] for the enumeration of substitution isomers for boron nitride polyhedral molecules with face spirals. It was applied to the fullerene-24 cage and the truncated octahedron for enumerating the related $B_{24-m}N_m$ isomers with boron in excess i.e. $m \leq 12$. The species which contain no $B – B$ or $N – N$ bonds are expected to possess a stability that could be compared to carbon fullerenes. The first-principles calculations were applied[57] to study the structure of several stoichiometric and non-stoichiometric boron nitride fullerenes of sizes ranging from 28 to 128 atoms and the relative stability of these fullerenes in both B- and N-rich environments were addressed. For the size larger than that of $B_{16}N_{16}$, the stoichiometric structures are found to be the most stable under B-rich conditions.

Tips of the boron nitride nanotubes synthesized[58] by arc discharge had a "triangular flag" like morphology. This morphology suggests the presence of energetically unfavorable odd-membered atomic rings in addition to favorable even-membered rings. Odd-numbered rings introduce unfavorable $B – B$ or $N – N$ bonds. However, in this case one cannot distinguish between the two ways placing the lines of unfavorable $B – B$ or $N – N$ bonds without energy consideration of diverse topology of these boron nitride hetero-networks. A single B-adatom adsorption on the external surface of zigzag BN nanotubes (as well as hexagonal BN sheets) was studied[59] by using the first principle spin-polarized DFT calculations.

The stoichiometric ratio B : N > 1 characteristic for some c-BN crystals was found to be associated with the presence of a free or bonded (in the forms of B_4C, B_2O_3 and B_xO) B-impurities. It explains why c-BN crystals with lower B-content grow only in special conditions.[60]

The behavior of boron with different degrees of purity, fineness, and crystal structure perfection during nitriding at high temperatures was studied[61] by electron microscopy, XRD (X-ray-diffraction), and chemical analysis. It was found that after high-temperature nitriding an almost 100 % yield of material of BN-stoichiometric composition was too difficult to achieve.

Investigations of structure and phase transformations of fine-grained h-BN powders induced by heating to concentrated light beam of different energies in nitrogen flow in optical furnace have been carried.[62] The surface observation of molding powders demonstrated formation of boron nitride of various structures depending on the beam energy as the high-density radiation energy resulted in the boiling process on the surface of an h-BN sample. Thermolysis of h-BN with impurities of B_2O_3 and foaming during boiling cause the formation of a dark porous melted drop in the center of the crater containing amorphous phase of boron, h-BN, B_2O_3 and B_2O. Coarse particles of whiskers obtained on a quartz substrate should be single-crystals of BN with orthorhombic lattice. Later, the light-induced heating in an optical furnace of fine grained h-BN powders was used to produce[63] the nanostructures of BN in a flow of dried and purified nitrogen. The structure and phase composition studies showed that the sublimated material settles on a substrate in the form of an amorphous phase, h-BN, boron-rich tetragonal $B_{51.2}N$ and $B_{25}N$ phases and also as pure boron. Studies of new BN nanomaterials obtained[64] by the concentrated light radiation heating in a high power optical furnace in a flow of commercially available nitrogen demonstrated that the use of pure boron powder as initial material also leads to the precipitation of amorphous structures in the form of equiaxed nanoparticles and films with short needle-like nanostructures on the surface. A process, which takes place during heating in the focal zone of the high power optical furnace in a steady flow of nitrogen, was specially investigated.[65] It was shown that the transformation of BN nanotubes initiates formation of whiskers (threads) around the crater and the drops on the surface of the sample. The drops and whiskers at the beginning and the end of their length have high content of B. It was demonstrated that the powder material deposited on the surface, which is removed from the crater, also have an increased B-content and consists of thread-like structures – nanotubes and whiskers (threads), equiaxed nanosized crystallites, crystals of h-BN and tetragonal phases $B_{51}N_2$ and $B_{25}N$, and amorphous boron nitride as well. For this material it was identified band gaps 3.5, 3.8 and 4.8 eV, which correspond to the phases of tetragonal $B_{51}N_2$ and $B_{25}N$, and h-BN, respectively.

Boron nitride has been prepared by nitriding pure B deposited on carbon substrates by chemical-vapor-deposition (CVD).[66] Thermodynamic analysis shows that the complete conversion of B to BN occurs only when N_2 is in excess. The detailed reaction ways between B and N can be drawn as follows: N atoms first attack B crystal, and then are combined with B into amorphous BN, and ultimately amorphous BN is transformed into orderly ranged BN above 1200 °C.

A systematic study on the effect of B-addition on structure and mechanical properties of $Al – Cr – N$ films grown by cathodic arc evaporation, involving X-ray photoelectron spectroscopy (XPS) indicated the formation of a nanocomposite structure consisting of a crystalline face-centered cubic $Al – Cr – (B) – N$ solid solution and an

amorphous phase a-BN$_x$, $x < 1$.[67] The formation of a BN$_x$ phase is likely, although this phase, due to its often amorphous character, is not visible in the XRD pattern. It was evident from the spectra that the increasing B content is associated with an increase of the intensity and fraction of the B − N peak. This can be interpreted by an increasing fraction of a-BN$_x$ phase with increasing B content.

Crystalline boron nitrides with B in excess

At very high temperatures, B/N system forms mixtures of phases of boron and boron nitrides with boron in excess.

For this system, the existence of boron subnitride B$_6$N with α-B-like structure was for the first time suggested as early as in 1976,[68] by an examination of the direct solid – diatomic gas reaction between boron and nitrogen in the elevated temperature range from 1480 up to 1820 K. The reaction mechanism is most likely topochemical, i.e., with rate limited by the process occurring at the interface between the reaction product and the solid reactant, yielding BN with amorphous boron, probably of an α-B-like structure, as the starting material, while a two-step reaction series occurs with an homogenous reaction to form B$_6$O followed by a topochemical reaction to yield BN when β-B is the starting material. Later, a number of boron subnitrides of different stoichiometries, e.g., B$_4$N, have been reported; however, neither their structure nor thermodynamic stability has been established.

Rhombohedral boron subnitride B$_{13}$N$_2$ was synthesized[69] by crystallization from the B/BN melt at 5 GPa. It represents a structural type produced by the distorted B$_{12}$ icosahedra linked together by N − B − N chains and inter-icosahedral B − B bonds. According to the Raman data, the subnitride belongs to a group of boron-rich compounds with structures related to α-B. The composition B$_{13}$N$_2$ is less stable than boron nitride phases of composition BN. The details of chemical interaction and phase transformations in the B/BN system were studied[70] *in situ* by XRD with synchrotron radiation at high temperatures and high pressures using multi-anvil press. The heating above 2380 K is accompanied by the disappearance of the β-B lines due to the boron melting. The quenching of the samples having the B$_6$N and B$_5$N compositions from 2400 to 2600 K leads to the formation of the well-crystallized rhombohedral boron subnitride phase with structure related to α-B and of general stoichiometry B$_{12+x}$N$_{2+y}$. XRD patterns of the well-powdered quenched samples shows the lines corresponding to a B$_6$O-like lattice. The lattice parameters of this boron nitride are intermediate between those of boron suboxide B$_6$O and boron carbide B$_{13}$C$_2$. The B$_{12+x}$N$_{2+y}$ phase features distorted B$_{12}$ icosahedra linked by N − B − N atomic chains, giving rise to a 3D framework. The similarity is greatest to B$_{4+z}$C$_{1−z}$, which has the same unit cell, space group, and atom sites as the subnitride. The site occupancies of the atoms of each crystallographic type are close to unit, so the synthesized phase has the B$_{13}$N$_2$ stoichiometry. The variation of lattice parameters of the as-synthesized B$_{12+x}$N$_{2+y}$ subnitride in all experiments was too small, which allows one to conclude that the resulting phase B$_{13}$N$_2$ is an individual subnitride and not a solid solution (in contrast to boron carbide analog). Over the whole $p − T$-range under study, B$_{13}$N$_2$ crystallizes in mixture with β-B, a phase similar to boron-rich tetragonal subnitride B$_{50}$N$_2$ (a phase with structure of hypothetical first

tetragonal boron I-B) and h-BN. The amount of the B$_{13}$N$_2$ phase in relation to B$_{50}$N$_2$-like phase increases with a higher BN content in the starting mixture; however, synthesis of single-phase B$_{13}$N$_2$ seems to be impossible because its formation at ~5 GPa occurs according to the liquid + h-BN ↔ B$_{13}$N$_2$ peritectic reaction. Results of an *in situ* study[71] of chemical interaction and phase relations in the B/BN system at pressure of ~ 5 GPa and temperatures up to 2800 K point to the contact interaction that gives rise to a metastable liquid in the system according to the B + h-BN ↔ liquid eutectic reaction, whose temperature is 2120 K. On subsequent heating to 2200 – 2250 K, the lines of B$_{13}$N$_2$ boron subnitride appear in the XRD patterns. It is the only thermodynamically stable boron subnitride, which melts incongruently at 2600 K and forms eutectic equilibrium with B at 2300 K and 4 atom % N.

These results on high-pressure synthesis of novel boron-rich solids, including boron-rich B/N phases, were summarized in a review.[72] The phase equilibria studies in the B/BN system by both *in situ* experiments and thermodynamic calculations have revealed the existence of at least three different boron subnitrides.

First, the high pressure synthesis of the so-called B$_6$N, the thermodynamically stable boron subnitride, was reported. However, its structure is unsolved. According to the simulations, it cannot belong to the α-B$_{12}$ family. Second boron subnitride, having the diffraction pattern similar to that of B$_{50}$N$_2$, seems to be a B$_{50}$N$_{2−x}$B$_x$ solid solution, so-called I-tetragonal boron, boron-rich quasi-periodic structure stabilized by nitrogen contamination, since its formation is observed only in the presence of BN, while the lattice parameters correspond to those expected for B$_{50}$N$_2$. The formation of third subnitride was observed which has a well-pronounced α-B$_{12}$-like powder XRD pattern. Its structure was resolved and represents a structural type produced by the distorted B$_{12}$ icosahedra linked by the atomic chains N − B − N. The stoichiometry of the phase is B$_{13}$N$_2$. Rhombohedral B$_{13}$N$_2$ was found to be the only thermodynamically stable boron subnitride at ~ 5 GPa. From the phase diagram of the system constructed by adjustment of the calculated equilibrium lines to the experimental data, B$_{13}$N$_2$ melts incongruently at 2600 K, according to the liquid + BN → B$_{13}$N$_2$ peritectic reaction, and forms an eutectic equilibrium with β-B$_{\sim 105}$ at 2300 K.

Joule-heating-induced failure of individual multi-walled BN nanotubes was investigated[73] in a high-resolution-transmission-electron-microscope (HRTEM) equipped with a scanning tunneling microscope unit. Direct observation of the failure process indicated that it occurred via thermal decomposition of tubular layers from inside-out of a tube leaving amorphous ball-like boron-based nanoparticles behind.

Local geometries in boron nitrides with B in excess

From the above discussion, one can conclude that all the boron nitride phases with B in excess, including the material obtained in the present work, can be imagined as mixtures of various boron modifications heavily doped with N. Since boron icosahedron B$_{12}$ is known to be the main structural motif of these crystals, the feasible local geometries of environments of N atoms in boron-rich B/N systems can be

constructed on the basis of crystal structure data on B_{12}-icosahedral networks examined, for example, by Higashi and Ishii.[74]

In the α-B crystal, B_{12} icosahedra are placed at each corner of the rhombohedral unit cell. Linkages between the icosahedra are affected along the 5-fold axis in the direction of the main crystallographic axes. There appear three icosahedral networks, each with translational periodicity along the [111]-axis. They are all crystallographically equivalent, extending parallel to the (111)-plane. The linkages between B_{12} icosahedra within each network are by a 3-centered bond. On the other hand, linkages between icosahedral networks are made by 2-centered bond along the 5-fold axes of icosahedra in the direction of the main crystallographic axes. In the structure of $B_{12}N_2$ (B_6N), which is of α-B structure-type, two nitrogen atoms are located on the [111]-axis in such a way that each of them is located at the center of a triangle formed with three icosahedra B_{12} (see Figures 14 and 15). Owing to the incorporation of N atoms, the rhombohedral unit cell volume is increased slightly with a variation of the rhombohedral angle. The recent data on lattice parameters of some B_6N-related structures were presented by Albert and Hillebrecht.[75]
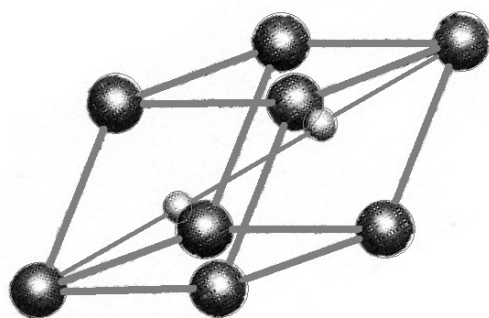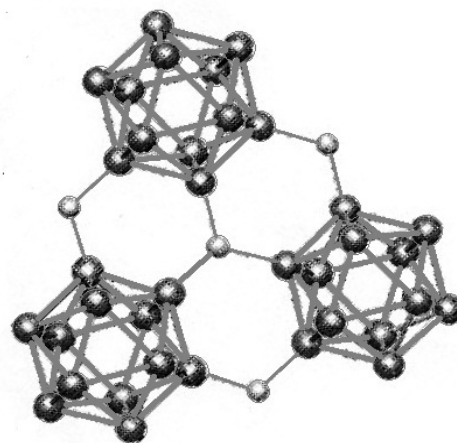

Figure 15. B_{12}-icosahedral network in the structure of B_6N as seen along the [111]-axis. The smaller circles stand for the N atoms.

Figure 14. Structure of B_6N (α-B structure-type). Each circle at the lattice point stands for the B_{12} icosahedron and smaller ones on the [111]-axis are N atoms.

Figure 16 shows the crystal structure of α-tetragonal boron. There are four icosahedra B_{12} per unit cell. In ideal structure, they coordinate tetrahedrally about an isolated B atom. But, it was reported that the accurate chemical composition of this crystal phase can be $B_{50}N_2$, and in real crystals the isolated B atoms should be replaced with N atoms. The icosahedral networks in $B_{50}N_2$ are, however, exactly the same as those in α-tetragonal boron.

Nitrogen in boron crystals

An overview of the studies in doping of β-B, including doping with N, has been given by us.[76] Main conclusions are as following. Nitrogen not only forms compound with boron, but also can be accommodated in large crystallographic voids of the β-B lattice.

Like other light elements, N is hardly removable from β-B.[77] According the microanalysis,[78] distribution of N impurity atoms in β-B is inhomogeneous.
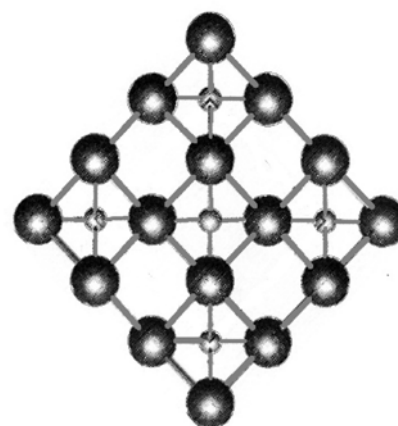

Figure 16. Structure of α-tetragonal boron as seen along the *c*-axis. The larger cycles stands for the B_{12} icosahedra and the smaller ones for the isolated N atoms. Each of the isolated N atoms is tetrahedrally coordinated with four icosahedra B_{12}.

Melting of boron in crucibles lined with boron nitride leads to the contamination of product with nitrogen: formation of a huge number of centers of crystallization and, consequently, crystallites.[79] Especially fragile samples of β-B are obtained during melting in nitrogen-containing atmosphere. In case of melting directly in BN crucibles, such crystallites form a crust around a coarse-crystalline core.[80] The β-B samples obtained by zone-melting of the pressed powders, in which H_3BO_3 served for binder material, contained gaseous impurities such as H, N and O.[81,82] Thermal-kinetic analysis exhibits a basic trend: decreasing in N content leads to the increasing in O and H contents. It weakens twinning and increase micro-strength and deformation energy. In β-B crystals doped by diffusion of N in the melt, the concentration of unpaired spins increases.[83,84] Corresponding electron-spin-resonance (ESR) line disappears only after a high-temperature annealing. Thermal treatment of β-B samples in nitrogen atmosphere can decrease their conductivity by ~ 200 %.[85]

A low-energy-electron-diffraction (LEED) pattern, which is characteristic of the (111)-surface of β-B, was obtained[86] after heating at a temperature higher than 1400 °C. As indicated by Auger spectroscopy, this treatment is sufficient to eliminate O and C, the main impurities present on the initial surface. However, a certain amount of N remains on the surface. On heating up to 1200 °C, the LEED pattern showed a completely disordered surface structure. In order to obtain a clean surface, the material was subjected to heat treatment at > 1300 °C and the vacuum attained in the apparatus was better than ~ 10^{-9} Torr. These conditions are necessary for recrystallization (α ↔ β transition) of boron.

As shown by Auger spectrometry, O was below the sensitivity limits, but small amounts of C and N were presented. No peaks of other elements were found. The amount of C seems too low to affect the surface structure. As for the N, it can be removed only by ion bombardment with Ar ions, but N reappears after the high-temperature heating necessary in order to reobtain a regular surface structure. This indicated that N is segregated near the surface and it is not ruled out if N diffuses from the bulk. The minimum ratio between N and B Auger peaks was about 1 : 50. The surface covered by this contamination should be of the order of one-tenth of a monolayer what can affect the surface structure of the β-B.

In the work[87] curried out to study the interaction of fine grained boron powders with gaseous environment and develop a technique for removal of gases from powders, we determined the content of N_2 from the analysis by the reduction melting method. In powders with average particles sizes of 1.90, 0.46 and 0.25 μm, there were determined 0.9, 0.5 and 2.1 wt. % N_2, respectively.

Studying[88] the ion implantation in boron leads to the undisputable result that in the absence of a significant concentration (a few tenths atom %) of N no amorphization takes place in β-B implanted with N-ions. This result can be understood taking into account following two factors: (i) about ⅓ of the valence electrons in boron icosahedron are directed towards external bonds and their number and directions can be easily changed in order to adopt it to surroundings, giving rise only distortions from the regular configuration, and greater stability and versatility to the icosahedron; (ii) the β-B lattice affords eighteen vacant voids per hexagonal unit cell and can accommodate impurity concentrations of the stopping range of the order of $3 \cdot 10^{21}$ cm^{-3}. As for the boron nitrides of composition BN, whose structure is not built of icosahedra, they are known to be damaged very easily by irradiation even at very low doses.

Structural model of nitrogen-doped boron

Structural patterns of boron nitrides with excess of boron allow the constructing of the structural model for nitrogen impurity centers in boron matrix.

Previously, we reported[89] a mass spectrometric study of boron cluster anions B_n^-, $n = 7 - 55$, containing multiple B_{12}-icosahedra, which were produced by laser vaporization both from pure boron (i.e. homogeneous) and boride (i.e. heterogeneous) target rods. While at lower masses these spectra were similar, at higher masses the boride spectrum

exhibited a completely different pattern: in addition to the local maximum at B_{13}^-, characteristic of the pure boron spectrum as well, a repeating intensity pattern having local maxima at $(B_{13}^-)(B_{12})_2$ and $(B_{13}^-)(B_{12})_3$ as well as $(B_{13}^-)(B_{13})$ were observed. These observations can be attributed to the structural differences between the two target materials. The appearance of B_{12} units in the boride mass spectrum is presumably due to the ablation of relatively labile B_{12} cages from the structure. The fusion of two B_{12} units, followed by their asymmetric dissociation upon electron attachment into $B_{13}^- + B_{11}$ or $B_{11}^- + B_{13}$ explains why both clusters B_{13}^- and B_{11}^- display higher intensities than their immediate neighbors in both the pure boron and the boride mass spectra. As for the relative prominence of B_{13}^--based species over B_{11}^--based ones in the mass spectra, it may be due to B_{13} having a higher electron affinity than B_{11} and also stability of B_{13}^- with regard to electron loss. Further, we had demonstrated[90] that created boron clusters can be self-assembled into nanostructures.

Taking into account high content of carbon, we cannot rule out that in addition to carbon-doped boron allotropes the synthesized material contains some amounts of boron carbide phases with crystalline lattices similar to that of α-B, which are semiconducting like this and all the rest crystalline modifications of boron.

From these studies and the above described results available in literature on B/N stoichiometries, crystalline boron nitrides, and local geometries in boron nitrides with B excess as well as on the behavior of nitrogen in boron crystals, we can figure out structure of possible atomic environments of N impurity atoms in synthesized material.

In crystallites of $B_{12}N_2$, nitrogen atoms are surrounded by 3 boron atoms, which are symmetrically placed in the same plane, i.e. like the intralayer coordination in h-BN. We can, therefore, approximate corresponding B – N chemical bonds length by that of h-BN: 1.45 Å. Not truly identical, but similar local environment would be realized in crystallites of $B_{12}N_2$, α-B doped with N (i.e. with no more than one N atom in the unit cell), and boron carbides doped with N (i.e. with one or two B or C atoms in the unit cell substituted with N atoms).

In crystallites of $B_{50}N_2$, nitrogen atoms are tetrahedrally surrounded by 4 boron atoms, i.e. like the coordination in c-BN. For this reason, we can approximate corresponding B – N bonds length by that of c-BN: 1.57 Å.

And finally, in crystallites of β-B, impurity atoms of nitrogen can be accommodated in crystallographic voids of types A(1), A(2), A(3), D and E with 12, 12, 12, 14 and 15 neighboring boron atoms and B – N bonds average length of 2.17, 2.10, 2.15, 2.36 and 2.38 Å, respectively. In crystallites of I-B, the situation must be almost similar, unless part of N atoms is substituted by other impurities, which possibly also stabilize the structure.

As for the flakes found in our material, their layered structure and chemical composition with highest nitrogen and relatively low carbon contents and small excess of boron point to the local formations of h-BN doped with carbon (i.e. h-BNC) together with small amount of boron-rich phases doped with nitrogen.

Theorizing

Finding out the electron energy levels of dopant nitrogen accommodated in various boron-rich lattices requires development of a special model of impurity centers. The situation when the nitrogen atom is introduced among boron atoms, already tightly bonded together, essentially differs from that when a tightly bonded with neighbors constituent boron atom is substituted. Therefore, standard models for impurity centers cannot be used for our purposes. The appropriate model was proposed and successfully applied for β-B doped with metals by us earlier.[91] Taking into account that such an impurity atom only slightly affect the crystalline structure, within the first approximation the donor energy level of the impurity atom can be found from the outer valence shell ionization potential of the same chemical element in isolated state shifting the corresponding electron energy level in the internal crystalline field. This chemical shift can be found assuming that changes in the electric field within an impurity atom are determined mainly by the boron atoms directly surrounding it. Within the proposed model, the depth of the donor level E_D formed by the nitrogen impurity atom embedded in a certain boron-rich crystallite is determined from the relation

$$E_D = (E_{IP} + E'_{IP}) - (E_{WF} - E_G) \qquad (1)$$

where E_{IP} is the known ionization potential of N atom in the isolated state, $E_{IP} = 14.53$ eV, and E'_{IP} is its shift in the crystalline field, while E_{WF} and E_G are the electron work function and the band gap of the semiconductor. In case of β-B, $E_{WF} = 6.13$ eV and $E_G = 1.56$ eV. This value for work function is chosen by us on the basis of analysis of the existing experimental data. As for α-B and I-B, there are no data available for their work function. That is why in all the cases below we use the difference $E_{WF} - E_G = 6.13$ eV − 1.57 eV = 4.56 eV assuming that it is almost the same for all crystalline modifications of boron.

Thus, to find the location of nitrogen donor levels on the energy axis it is necessary to calculate only one quantity, E'_{IP}. It is possible to estimate its value as a quantum-mechanical mean of the electron potential energy in the crystalline field. In the initial quasi-classical approximation we obtain:

$$E'_{IP} = -\frac{3 N E_{IP}}{4\pi(4n_{IP}^2 - l_{IP}(l_{IP}+1))}\sqrt{\frac{2E_{IP}}{n_{IP}^2 - l_{IP}(l_{IP}+1)}}\sum_{i=1}^{i=q}\varphi_i V_i(r'_{IP}, r''_{IP}, d) \qquad (2)$$

Here N is the coordination number − number of boron atoms surrounding the impurity nitrogen atom, and d is the B − N bonds average length; function $V_i(r'_{IP}, r''_{IP}, d)$ denotes the volume of the intersection of i th layer of the boron atom with the layer of the nitrogen atom limited by the classical turning points radii r'_{IP} and r''_{IP} of the outer valence shell electron:

$$r'_{IP} = \frac{n_{IP} - \sqrt{n_{IP}^2 - l_{IP}(l_{IP}+1)}}{\sqrt{2E_{IP}}} \qquad (3)$$

$$r''_{IP} = \frac{n_{IP} + \sqrt{n_{IP}^2 - l_{IP}(l_{IP}+1)}}{\sqrt{2E_{IP}}} \qquad (4)$$

where n_{IP} and l_{IP} represent, respectively, the principal and orbital quantum numbers of the outer valence shell electron in the impurity atom. For nitrogen $n_{IP} = 2$ and $l_{IP} = 1$.

The function $V_i(r'_{IP}, r''_{IP}, d)$ is calculated as a linear combination of intersection volumes of 4 pairs of spheres:

$$V_i(r'_{IP}, r''_{IP}, d) = \\ V(r_i, r''_{IP}, d) + V(r_{i-1}, r'_{IP}, d) - V(r_i, r'_{IP}, d) - V(r_{i-1}, r''_{IP}, d) \qquad (5)$$

Here the coefficient φ_i is the volume-average of the electric field potential in the i th radial layer of boron atom, q is the number of layers of the quasi-classical averaging. The parameters r_i and r_{i-1} are the external and internal radii of the i th layer of boron atom, respectively (assuming $r_0 \equiv 0$). For B atom the parameter $q = 5$. As for the r_i and φ_i, they are given in Table 2. Their numerical values have been calculated and tabulated in ref.[92] The function $V(r_1, r_2, d_{12})$ has a geometric meaning as the volume of an intersection of two spheres with radii r_1 and r_2 whose centers are at the distance d_{12} from each other. It is an algebraic piecewise continuous function. Explicit form of $V(r_1, r_2, d_{12})$ has been described.[93]

Table 2. Quasi-classical parameters of potential distribution in B atom.

i	r_i, a.u.	φ_i, a.u.
1	2.758476 E−2	+ 2.105468 E+2
2	5.098016 E−1	− 8.882329 E+0
3	7.441219 E−1	− 3.652920 E+0
4	4.021346 E+0	− 2.060720 E−1
5	4.337060 E+0	− 6.135348 E−4

Table 3. Parameters of N donor centers in boron crystals.

Structure	Site	N	d, Å	E_D, eV
α-B		3	1.45	− 5.2
	A(1)	12	2.17	−12.3
	A(2)	12	2.10	−14.0
β-B	A(3)	12	2.15	−12.8
	D	14	2.36	−11.1
	E	15	2.38	−12.1
I-B		4	1.57	− 8.7

The calculated electron energy levels together with parameters of corresponding impurity centers are summarized in Table 3. Thus, all the $E_D < 0$, i.e. N-related donor levels are placed immediately inside the conduction band or even above the vacuum level. In this context it should be noted that the calculated negative energy levels of

course are definitely virtual and they never can be occupied. These dopant atoms supply electrons at first to low-lying electron traps located within the band gap and then to delocalized electron states at the bottom of the conduction band, i.e., they cause metallization of the material when introduced at sufficiently high concentrations.

Main result of the present calculations is that the N atoms in BN_x act as electron-donors. The same can be argued from the following qualitative consideration. Boron is known to be one of the most electronegative elements, but it is less electronegative than nitrogen. For this reason, in common boron nitrides with chemical formula BN, the electron density is shifted from B atoms towards N atoms. However, in boron nitrides with excess of boron, BN_x, $x \ll 1$, boron atoms enable to form icosahedra and other multi-atomic clusters, significantly enhancing in this way the electronegativity of the boron component. Thus, the electron density can be shifted from N atoms towards B clusters.

Presence of traces of boron nanophases in the material obtained cannot be rules out. The nanophases are expected to be metallic.[94] Recently, it has been proposed[95] that the so-called borophene, the structure built up from planar hexagonal B_{36} clusters, must be fully metallic. However, it seems too doubtful that amount of nanoboron-component is enough to form a continuous conductive matrix. Thus, the metallization related to doping phases of semiconducting boron, and maybe boron carbide inclusions, with nitrogen seems to be prevailing.

Conclusion

In summary, the "metallic" conductivity in boron nitride with boron in excess can be explained in a way similar to that of boron doped with metals. It means that such a material can be modeled as a mix of boron phases heavily doped with nitrogen impurity.

In this regard, it is appropriate to discuss the phenomena of metallic conductivity and superconductivity in boron crystals.

A long-standing issue, why β-B, with odd number of electrons in the regular unit cell, which, as the band calculations predict, was to be metallic, is in fact semiconducting, has been solved.[96] The problem was related to the breaking of stoichiometry in this crystal: the presence of unfilled bands requires reconstruction of chemical bands.

As for α-B, using an expansion of plane waves, the first principles calculations of the energy bands of B_{12} were performed[97] which found a gap of width 1.427 eV, i.e. α-B must be a semiconductor.

A unified picture for B-based icosahedral cluster solids has been proposed.[98] The common features are: (i) they are expected to have complicated structures such as giant unit cell crystals or quasi-crystals because of inconsistency between the icosahedral symmetry and the space periodicity, (ii) they can have both metallic and covalent bonds, because B is located at the boundary of covalent/metallic bonding in the Periodic Table, (iii) their Fermi level can be located in the deep pseudo-gap or at the high DOS position because of

high symmetry of the icosahedron. The metallic–covalent bonding conversion in boron can occur at sites other than the center of the icosahedron. In particular, when a vanadium V atom is doped in the certain-type crystallographic void of β-B, the bonding nature is converted from the covalent one to the more metallic one. A characteristic phenomenon in the V-doped β-B is the change of electrical conductivity from that of semiconducting hopping-type into metallic one by doping with only ~ 1 atom % V.[99] This unique conversion of electrical conductivity seems to be due to the local metallic–covalent bonding conversion. A high concentration of lithium Li (up to the composition $LiB_{5.8}$, i.e. 18 Li atoms per cell) was doped into β-B.[100] In Li- or Mg-doped β-B, electron doping was compensated by removing of interstitial B atoms and by generating of vacancies.

Theoretical exploration of a group of B_{12}-based materials, A_xB_{12}, with A = Li and Ca, and $x = 1 - 4$, was done[101] by performing LDA calculations of the electronic structure, including DOS, using the first principles pseudopotentials. Li-doped materials mostly demonstrate to be sufficiently stable, whereas it is shown that all calcium-doped materials are unstable, including Li_2CaB_{12}. These calculations showed essentially metallic behavior of stable and metastable Li_xB_{12}. Favorable superconducting properties were predicted for Li_3B_{12}, in the context of the sufficiently high DOS at the Fermi energy and obtained bulk modulus that is indicative of strong electron–phonon coupling.

An alternative route to achieve the superconducting state in boron-rich solids has been proposed, the hole-doping of B_{12} icosahedra.[102] For this purpose a prototype metallic phase of $B_{13}C_2$ was considered. It was shown that in this compound the boron icosahedral units are mainly responsible for large phonon frequencies and moderate electron–phonon coupling. It was suggested that relatively high critical temperature could be a general feature of hole-doped boron icosahedral solids.

Thus, boron, heavily doped with metal impurities, exhibits metallic conductivity and even superconductivity.

As for the boron "doped" with nitrogen, i.e., boron nitride with boron in excess, there is only single indirect experimental evidence of its "metallicity" mentioned above. It was predicted that superhard rhombohedral subnitride $B_{13}N_2$ might exhibit metallic conductivity. Unfortunately, the $B_{13}N_2$ crystallization by peritectic reaction in the studied $p - T$ range did not allow the study of such properties. Taking into account (i) metallic behavior and even superconductivity observed in boron-rich solids at high pressure and (ii) the results on high-pressure synthesis of novel boron-rich solids, including boron-rich B/N phases, reviewed above, one may expect that these high pressure phases can have exceptional electronic and phonon transport properties.

The theoretical results obtained in the present work for N-doping of boron quantitatively support already suggested qualitative mechanism of modification of the electronic properties of boron by doping. Initially electrons from donor impurities fill the empty intrinsic acceptor levels. It leads to an increase in the concentration of hole-hopping centers and, consequently, p-type hopping conductivity also increases. However, after about a half of these centers have been filled,

a decrease in the concentration of localized holes prevails and the hopping conductivity begins to decrease as well. At higher dopant concentrations, when all of acceptor centers of intrinsic origin are occupied by electrons, the inversion of type of conduction takes place, and the n-type conductivity starts to increase. Finally, the doping of boron with donor atoms at sufficiently high concentrations yields the metallization of the material – a semiconductor-to-semimetal transition.

Acknowledgements

References

[1] Chkhartishvili, L., Lezhava, D., Tsagareishvili, O., Gulua, D., *Proc. Police Acad. Georg.*, **1999**, *1*, 295-300.

[2] Chkhartishvili, L. S., *Phys. Solid State*, **2004**, *46*, 2126-2133.

[3] Chkhartishvili, L., Lezhava, D., Tsagareishvili, O., *J. Solid State Chem.*, **2000**, *154*, 148-152.

[4] Chkhartishvili, L., *J. Solid State Chem.*, **2004**, *177*, 395-399.

[5] Chkhartishvili, L., *Mater. Sci. Ind. J.*, **2006**, *2*, 18-23.

[6] Al'tshuler, A. M., Vekilov, Y. K., Umarov, G. R., *High Temp. High Press.*, **1976**, *8*, 635-662.

[7] Zhang, Zh., Guo, W., *Nano Lett.*, **2012**, *12*, 3650-3655.

[8] Zhang, Sh., Wang, Q., Kawazoe, Y., Jena, P., *J. Am. Chem. Soc.*, **2013**, *135*, 18216-18221.

[9] Hu, Sh., Zhao, J., Jin, Y., Yang, J., Petek, H., Hou, J. G., *Nano Lett.*, **2010**, *10*, 4830-4838.

[10] Srivastava, A., Sharma, M., Tyagi, N., Kothari, S. L., *J. Comput. Theo. Nanosci.*, **2012**, *9*, 1693-1699.

[11] Mousavi, H., J. Supercond. *Novel Magn.*, **2013**, *26*, 2905-2909.

[12] Owens, F. J., *Mol. Phys.*, **2011**, *109*, 1527-1531.

[13] Anota, E. Ch., Escobedo–Morales, A., Villanueva, M. S., Vázquez–Cuchillo, O., Rosas, E. R., *J. Mol. Modeling*, **2013**, *19*, 839-846.

[14] Du, A., Chen, Y., Zhu, Zh., Amal, R., Lu, G. Q. (M.), Smith, S. C., *J. Am. Chem. Soc.*, **2009**, *131*, 17354-17359.

[15] Terrones, M., Charlier, J.-C., Gloter, A., Cruz–Silva, E., Terrés, E., Li, Y. B., Vinu, A., Zanolli, Z., Dominguez, J. M., Terrones, H., Bando, Y., Golberg, D., *Nano Lett.*, **2008**, *8*, 1026-1032.

[16] Barone, V., Peralta, J. E., *Nano Lett.*, **2008**, *8*, 2210-2214.

[17] Lai, L., Lu, J., Wang, L., Luo, G., Zhou, J., Qin, R., Gao, Zh., Mei, W. N., *J. Phys. Chem. C*, **2009**, *113*, 2273-2276.

[18] Tang, P., Zou, X., Wang, S., Wu, J., Liu, H., Duan, W., *RSC Adv.*, **2012**, *2*, 6192-6199.

[19] Li, X., Wu, X., Zeng, X. Ch., Yang, J., *ACS Nano*, **2012**, *6*, 4104-4112.

[20] Wang, Y., Ding, Y., Ni, J., *J. Phys. Chem. C*, **2012**, *116*, 5995-6003.

[21] Alem, N., Ramasse, Q. M., Seabourne, C. R., Yazyev, O. V., Erickson, K., Sarahan, M. C., Kisielowski, C., Scott, A. J., Louie, S. G., Zettl, A., *Phys. Rev. Lett.*, **2012**, *109*, 126102 (1-5).

[22] Park, Ch.-H., Louie, S. G., *Nano Lett.*, **2008**, *8*, 2200-2203.

[23] Chen, W., Li, Y., Yu, G., Li, Ch.-Zh., Zhang, Sh. B., Zhou, Zh., Chen, Zh., *J. Am. Chem. Soc.*, **2010**, *132*, 1699-1705.

[24] Samarakoon, D. K., Wang, X.-Q., Appl. *Phys. Lett.*, **2012**, *100*, 103107 (1-4).

[25] Zhang, H. X., Feng, P. X., *ACS Appl. Mater. Interfaces*, **2012**, *4*, 30-33.

[26] Lopez–Bezanilla, A., Huang, J., Terrones, H., Sumpter, B. G., *J. Phys. Chem. C*, **2012**, *116*, 15675-15681.

[27] Lopez–Bezanilla, A., Huang, J., Terrones, H., Sumpter, B. G., *Nano Lett.*, **2011**, *11*, 3267-3273.

[28] Lopez–Bezanilla, A., Huang, J., Terrones, H., Sumpter, B. G., *Nano Lett.*, **2012**, *12*, 3879-3879.

[29] Guo, Y., Guo, W., *Nanoscale*, **2014**, *6*, 3731-3736.

[30] Anota, E. C., Gutiérrez, R. E. R., Morales, A. E., Cocoletzi, G. H., *J. Mol. Modeling*, **2012**, *18*, 2175-2184.

[31] Mousavi, H., Moradian, R., *Solid State Commun.*, **2013**, *153*, 17-22.

[32] Berseneva, N., Gulans, A., Krasheninnikov, A. V., Nieminen, R. M., *Phys. Rev. B*, **2013**, *87*, 035404 (1-9).

[33] Zeng, J, Chen, K.-Q., Sun, C. Q., *Phys. Chem. Chem. Phys.*, **2012**, *14*, 8032-8037.

[34] Wang, Y., Ding, Y., *J. Phys. Chem. C*, **2013**, *117*, 3114-3121.

[35] Xue, Y., Liu, Q., He, G., Xu, K., Jiang, L., Hu, X., Hu, J., *Nanoscale Res. Lett.*, **2013**, *8*, 49-55.

[36] Yan, B., Park, Ch., Ihm, J., Zhou, G., Duan, W., Park, N., *J. Am. Chem. Soc.*, **2008**, *130*, 17012-17015.

[37] Batista, R. J. C., de Oliveira, A. B., Pereira, N. R., Paolini, R. S., Manhabosco, T. M., *J. Phys. Cond. Matter*, **2012**, *24*, 165501 (1-10).

[38] Nakamura, J., Nitta, T., Natori, A., *Phys. Rev. B*, **2005**, 72 205429 (1-5).

[39] Liu, Y., Wu, X., Zhao, Y., Zeng, X. Ch., Yang, J., *J. Phys. Chem. C*, **2011**, *115*, 9442-9450.

[40] Yu, Zh., Hu, M. L., Zhang, C. X., He, C. Y., Sun, L. Z., Zhong, J., *J. Phys. Chem. C*, **2011**, *115*, 10836-10841.

[41] Xiao, H. P., He, Ch., Zhang, Ch., Sun, L. Z., Peng, X., Zhang, K., Zhong, *J., Physica B*, **2012**, *407*, 4770-4472.

[42] Song, L., Balicas, L., Mowbray, D. J., Capaz, R. B., Storr, K., Ci, L., Jariwala, D., Kurth, S., Louie, S. G., Rubio, A., Ajayan, P. M., *Phys. Rev. B*, **2012**, *86*, 075429 (1-12).

[43] Zhou, Y., Wang, Zh., Yang, P., Gao, F., *J. Phys. Chem. C*, **2012**, *116*, 7581-7586.

[44] Menezes, M. G., Capaz, R. B., *Phys. Rev. B*, **2012**, *86*, 195413 (1-9).

[45] Li, X., Yang, W., Liu, B., *Nano Lett.*, **2007**, *7*, 3709-3715.

[46] Wang, L., Mo, Y., Rulis, P., Ching, W. Y., *RSC Adv.*, **2013**, *3*, 25374-25387.

[47] Martin, J. M. L., François, J. P., Gijbels, R., *Chem. Phys.*, **1989**, *90*, 6469-6485.

[48] Knight Jr., L. B., Hill, D. W., Kirk, T. J., Arrington, C. A., *J. Phys. Chem.*, **1992**, *96*, 555-561.

[49] Meloni, G., Baba, M. S., Gingerich, K. A., *J. Chem. Phys.*, **2000**, *113*, 8995-8999.

[50] Mahalakshmi, S., Yeager, D.L., *Mol. Phys.*, **2003**, *101*, 165-174.

[51] la Placa, S. J., Roland, P. A., Wynne, J. J., *Chem. Phys. Lett.*, **1992**, *190*, 163-168.

[52] Albe, K., Möller, W., Heinig, K.-H., *Radiat. Eff. Def. Solids*, **1997**, *141*, 85-97.

[53] Vandenbosch, R., *Phys. Rev. A*, **2003**, *67*, 52709 (1-5).

[54] Ding, H., Morse, M. D., Mailer, J. P., *Mol. Phys.,* **2007**, *105*, 1251-1261.

[55] Feng, Y., Fang, F., *Asian J. Chem.,* **2012**, *24*, 4012-414.

[56] Shao, Y., Jiang, Y., *J. Phys. Chem.,* **1996**, *100*, 1554-1558.

[57] Alexandre, S. S., Chacham, H., Nunes, R. W., *Phys. Rev. B,* **2001**, *63*, 045402 (1-5).

[58] Saito, Y., Maida, M., *J. Phys. Chem. A,* **1999**, *103*, 1291-1293.

[59] Li, L. L., Yang, S. Q., Yang, X. J., Xu, X. W., Tang, C. C., J. *Mol. Str.,* **2012**, *1020*, 183-187.

[60] Shulzhenko, A. A., Sokolov, A. N., *High Press. Res.,* **2000**, *18*, 345-351.

[61] Lyashenko, V. I., Ostrovskaya, N. F., Zelyavskii, V. B., Kurdyumov, A. V., Bartnitskaya, T. S., *Powd. Metall. Met. Ceram.,* **2003**, *42*, 189-194.

[62] Sartinska, L.L., Frolov, A. A., Koval', A. Yu., Danilenko, N. A., Timofeeva, I. I., Rud', B. M., *Mater. Chem. Phys.,* **2008**, *109*, 20-25.

[63] Sartinska, L.L., *Acta Mater.,* **2011**, *59*, 4395-4403.

[64] Sartinska, L. L., Voynich, E. V., Bloschanevich, O. M., Frolov, G. O., Koval', O. Yu., Danilenko, M. I., in *Proc. 7th Int. Conf. MEE,* IPMS, Kiev, **2012**, 129-129.

[65] Sartinska, L. L., Frolov, A. A., Andreeva, A. F., Voynich, Y. V., Kasumov, A. M., Frolov, G. A., Tinkov, V. A., Stonis, V. V., *Nano Studies,* **2012**, *5*, 89-102.

[66] Ye, F., Zhang, L., Liu, Y., Li, S., Su, M., Yin, X., Cheng, L., Prog. *Nat. Sci. Mater. Int.,* **2012**, *5*, 433-439.

[67] Tritremmel, C., Daniel, R., Lechthaler, M., Rudigier, H., Polcik, P., Mitterer, C., *Surf. Coat. Technol.,* **2012**, *213*, 1-7.

[68] Condon, J. B., Holcombe, C. E., Johnson, D. H., Steckel, L. M., *Inorg. Chem.,* **1976**, *15*, 2173-2179.

[69] Solozhenko, V. L., Kurakevych, O. O., *J. Phys. Conf. Ser.,* **2008**, *121*, 062001 (1-7).

[70] Solozhenko, V. L, Kurakevych, O. O., *J. Solid State Chem.,* **2009**, *182*, 1359-1364.

[71] Solozhenko, V. L., Kurakevych, O. O., Turkevich, V. Z., Turkevich, D. V., *J. Phys. Chem. B,* **2010**, *114*, 5819-5822.

[72] Kurakevych, O. O, Solozhenko, V. L., *High Press. Res.,* **2011**, *31*, 48-52.

[73] Xu, Zh., Golberg, D., Bando, Y., *Nano Lett.,* **2009**, *9*, 2251-2254.

[74] Higashi, I., Ishii, T., *Forma,* **2001**, *16*, 187-207.

[75] Albert, B., Hillebrecht, H., *Angew. Chem. Int. Ed.,* **2009**, *48*, 8640-8668.

[76] Gabunia, D. L., Tsagareishvili, O. A., Chkhartishvili, L. S., Tavadze, G. F., in *Proc. 8th Int. Cong. ETHTMA,* NSC KhPTI – PPC Contrast, Kharkiv, **2007**, 211-272.

[77] Tsagareishvili, G. V., *Jpn. J. Appl. Phys. Ser.,* **1994**, *10*, 21-24.

[78] Prudenziati, M., in *Boron and Refractory Borides*, Springer-Verlag, Berlin, **1977**, 241-261.

[79] Niemyski, T., Pracka, I., Szczerbiński, R., Frukacz, Z., in *Boron: Preparation, Properties, and Applications*, Plenum Press, New York, **1965**, 35-43.

[80] Starks, B. J., Medcalf, W. E., in *Boron: Synthesis, Structure, and Properties*, Plenum Press, New York, **1960**, 59-69.

[81] Tsagareishvili, G. V., Oganezov, K. A., Bairamashvili, I. A., Khvedelidze, A. G., Mazmishvili, G. A., Chepelev, V. V., Tabutsidze, M. L., *J. Less-Comm. Met.,* **1979**, *67*, 419-424.

[82] Tavadze, F. N., Lominadze, J. N., Khvedelidze, A. G., Tsagareishvili, G. V., Shorshorov, M. Kh., Bulichev, S. I., *J. Less-Comm. Met.,* **1981**, *82*, 95-99.

[83] Appenheimer, S., Niemyski, T., Jabłoński, R., *Electron Technol.,* **1970**, *3*, 29-33.

[84] Gaulé, G. K., Breslin, J. T., Pastore, J. R., Shutteleworth, R. A., in *Boron: Synthesis, Structure, and Properties,* Plenum Press, New York, **1960**, 159-174.

[85] Babaev, R.M., Iglitsyn, M. I., Kiskachi, Yu. A., Tilhonov, V. N., *Dev. Control Syst.,* **1969**, *8*, 49-49.

[86] Rovida, G., Maglietta, M., *J. Appl. Phys.,* **1973**, *44*, 3801-3082.

[87] Tsagareishvili, G. V., Bairamashvili, I. A., Oganezov, K. A., Tabutsadze, M. I., Tsagareishvili, O. A., J. *Less-Comm. Met.,* **1981**, *82*, 131-135.

[88] Schmirgeld, L., Zuppiroli, L., Brunel, M., Delafon, J., Templier, C., *AIP Conf. Proc.,* **1991**, *231*, 630-638.

[89] Xu, S.-J., Nilles, J. M., Radisic, D., Zheng, W.-J., Stokes, S., Bowen, K. H., Becker, R. C., Boustani, I., *Chem. Phys. Lett.,* **2003**, *379*, 282-286.

[90] Boustani, I, Becker, R., in *Proc. 9th Ann. Nanotechnol. Conf. & Trade Show*, NSTI, Boston, **2006**, MO 60.802.

[91] Chkhartishvili, L., Murusidze, I., Darchiashvili, M., Tsagareishvili, O., Gabunia, D., *Solid State Sci.,* **2012**, *14*, 1673-1682.

[92] Chkhartishvili, L., Berberashvili, T., *J. Electro Magn. Anal. Appl.,* **2010**, *2*, 205-243.

[93] Chkhartishvili, L. S., *Math. Notes,* **2001**, *69*, 421-428.

[94] Chkhartishvili, L., in *Boron: Compounds, Production and Application*, Nova Sci. Publ. Inc., New York, **2011**, 221-294.

[95] Piazza, Z. A., Hu, H.-Sh., Li, W.-L., Zhao, Y.-F., Li, J., Wang, L.-Sh., *Nat. Commun.,* **2014**, *5*, 3113 (1-15).

[96] Shirai, K., Uemura, N., *Solid State Sci.,* **2012**, *14*, 1609-1616.

[97] Lee, S., Bylander, D. M., Kleinman, L., *Phys. Rev. B,* **1990**, *42*, 1316-1320.

[98] Kimura, K., Hyodo, H., Takagiwa, Y., Kirihara, K., Soga, K., Kato, K., Takata, M., in *Abs. 17th Int. Symp. Boron, Borides & Rel. Mater.*, ITU, Istanbul, **2011**, 102-102.

[99] Soga, K., Hyodo, H., Iseki, H., Kimura, K., in *Abs. 17th Int. Symp. Boron, Borides & Rel. Mater.,* ITU, Istanbul, **2011**, 68-68.

[100] Hyodo, H., Nazu, A., Soga, K., Kimura, K., *Solid State Sci.,* **2012**, *14*, 1578-1583.

[101] Gunji, Sh., Kamimura, H., *Phys. Rev. B,* **1996**, *54*, 13665-13673.

[102] Calandra, M., Vast, N., Mauri, F., *Phys. Rev. B,* **2004**, *69*, 224505 (1-5).

VAPOR–SOLID GROWTH OF InP AND Ga$_2$O$_3$ BASED COMPOSITE NANOWIRES

D. Jishiashvili[a]*, Z. Shiolashvili[a], N. Makhatadze[a], A. Jishiashvili[a], V. Gobronidze[a] and D. Sukhanov[a]

InP/Ga$_2$O$_3$ core-shell nanowires were grown on Si substrate at 400 ºC in the hydrazine (N$_2$H$_4$) vapor diluted with 3 mol. % H$_2$O. The crystalline InP and solid Ga served as source materials for the growth of nanowires. According to TEM and EDX data the nanowires consisted of InP core with wurtzite-type structure and an amorphous Ga$_2$O$_3$ shell. The minimum diameter of NWs was 14 nm, while the maximum lengths reached several micrometers. The twinned planes appeared in WZ InP core at increased nanowire diameters. Based on the obtained results and possible chemical reactions, the following mechanism was proposed for the growth of core-shell nanowires: pyrolytic decomposition of hydrazine caused the appearance of intermediate NH$_2$, NH and H species in the vapor. At elevated temperatures the crystalline InP source was also dissociated to In and phosphorus precursors. At source temperatures close to 600 ºC, due to the interaction of In and Ga sources with water molecules and hydrazine decomposition products the volatile Ga$_2$O and In$_2$O were formed. These molecules reached the Si substrate which was heated to 400 ºC. The final chemical reaction involved Ga$_2$O$_3$, In$_2$O$_3$ and phosphorus precursors. As a result of a spontaneous reaction the Ga$_2$O$_3$ and InP phases were produced and segregated. The InP crystallized as a core while Ga$_2$O$_3$ created the amorphous shell, because the growth temperature was insufficient for its crystallization.

* Corresponding Author
  E-Mail: d_jishiashvili@gtu.ge
[a] V. Chavcanidze Institute of Cybernetics, Georgian Technical University, 0186, Euli Str. 5, Tbilisi, Georgia

Introduction

The core-shell nanostructures are considered as the promising building blocks for the future advanced nanodevices.[1-3] The unique properties of core-shell nanostructures arise not only from quantum confinement and surface dominated features, but also due to the processes that take place in the shell material and core–shell interface. The band gap of core semiconductor and its emission profile can be preciously tuned by selecting the proper composition and thickness of a shell material, without altering the size of core nanoparticle.[4-7] The latest demonstration of the use of biofunctionalized InP/ZnS core-shell nanocrystals raised interest in the development of future nanoprobes for biomedical applications, that may replace the highly toxic cadmium-based nanostructure with less toxic InP based biomarkers.[5,8,9]

Together with zero dimensional (0D) core-shell nanocrystals the 1D core-shell nanostructures (nanowires, nanotubes, nanorods, nanobelts etc.) also attracted a great interest and show promise for different applications. Ultrasensitive toxic-gas sensors were fabricated recently using various core–shell nanowires (NWs).[10-13] This type of 1D nanostructures were also successfully used for light emitting diodes,[14-16] for the fabrication of solid quantum bits[17] and nanowire lasers,[18] for the effective solar energy conversion,[19] etc.

1D nanostructures with InP cores are considered as promising materials not only due to the unique electronic and optical properties of indium phosphide, but also for their potential wide range of applications in different fields beginning from telecommunications and ending with biological imaging. Indium phosphide offers a "green" alternative to the traditional cadmium-based biomarkers, but suffers from extreme susceptibility to oxidation. Coating InP cores with more stable shell materials significantly improves the resistance to oxidation and photostability [5, 20], thus increasing the interest of scientists in the development of new InP based core-shell nanostructures.

The purpose of this work was to develop the one-step process for the growth of InP based core–shell nanowires.

Experimental

The nanowires were grown in the tubular vertical quartz reactor which was first evacuated and then filled with hydrazine (N$_2$H$_4$) vapor to its saturated pressure of ~ 10 Torr. The piece of a flat crystalline InP covered with coarsely ground metallic Ga served as a source for producing volatile species. The source was placed at the bottom of the reactor and annealed in the presence of hydrazine vapor which was containing 3 mol. % water molecules. The weight ratio of InP and Ga was 2.5 at a total mass of 0.50 – 0.55 g. In the presence of hydrazine decomposition products the volatile compounds were formed at the surfaces of Ga and InP sources, which after sublimation caused the growth of ID nanomaterials on the Si substrate placed at 2 cm above the source.

The Si substrate temperature (growth temperature) was in the range of 400 – 430 °C, which corresponded to the source temperature of 600 – 635 °C. The nanowire growth time of was 45 – 60 min. The details of the growth technology are presented elsewhere.[21]

The morphology and structure of NWs were studied using FEI Quanta FEG 600 scanning electron microscope (SEM). Transmission electron microscopy (TEM) images were recorded on a Philips CM12 operated at 100 keV with a W cathode and a FEI Tecnai F30 (FEG) equipped with an energy dispersive X-ray (EDX) and a high-angle annular dark-field (HAADF) detector The Gibbs free energies for the chemical reactions were evaluated using the computer software HSC Chemistry–6 and chemical database stored in this program.

Results and discussion

The whole growth process was based on the transportation of constituent atoms from the source material (solid InP and Ga) located in the hot zone of the reactor (T_{max} = 635 °C) to the Si substrate placed at 2 cm distance just above the source (cold zone, T_{max} = 430 °C). The vertical quartz reactor operated at a static pressure (10 Torr) of N_2H_4 + 3 mol. % H_2O vapor and was isolated from the vacuum system during the growth of nanowires. In the absence of carrier gases only vaporized and volatile molecules could reach the substrate surface. The convectional flow, which appeared due to the temperature difference between source and substrate also promoted the transportation of volatile species.

The pyrolytic decomposition of hydrazine in the presence of 3 mol. % H_2O leads to a variety of highly reactive fragments. The detailed study of ammonia and hydrazine decomposition at elevated temperatures was presented in Ref.[22,23] Decomposition of hydrazine can usually be performed by two methods: catalytic decomposition (for example on semiconductor or metal source surfaces, or heated quartz reactor walls) and thermal decomposition.[24,25] Following active intermediate species were formed during the decomposition: NH_2, NH, N, H, until the final stable products (N_2, H_2) were produced. Besides, the dissociative adsorption of hydrazine may take place with the formation of two NH_2 radical species on the source surface. The strong nitriding ability and activity of hydrazine decomposition products was confirmed in our previous experiments on the growth of single crystalline Ge_3N_4 1D nanowires at 500 °C using volatile GeO molecules as germanium precursors.[26] In this growth process the temperature was by 350 °C lower in comparison with the synthesis of Ge_3N_4 nanowires using the same GeO source molecules and ammonia vapor.[27,28] We assume, that such a dramatic reduction of nitriding temperature in hydrazine vapor can be explained only by the high concentration of active NH_2 and/or NH species, together with possible presence of atomic nitrogen. It should be noted that the single crystalline, pure germanium nitride NWs and micrometer sized crystalline blocks were obtained in hydrazine vapor in spite of the presence of oxidizing water molecules in it (3 mol. % H_2O).[26] Besides, the chain like pure germanium nanostructures were formed on the substrate and no traces of GeO or GeO_2 were found in the condensed material.[21] This proves a high reducing ability of
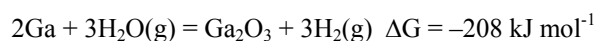
hydrazine vapor. On the nanoscale range the high activity of hydrazine was confirmed in numerous works on the reduction of graphene layer at room temperature from its oxide using hydrazine (see for example Ref.[29]).

The thermal decomposition of InP source in the reactor served for producing gaseous phosphorus ambient and In precursors. As it was found in Ref.[30,31] in the presence of hydrogen the InP dissociation temperature can be significantly decreased. For example, the energy of activation of dissociation reaction
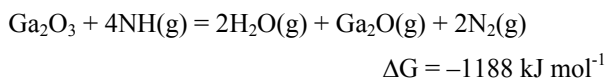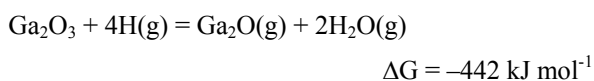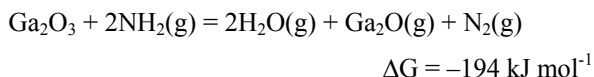
$$InP_{(solid)} = In_{(solid)} + ½P_{2(gas)}$$
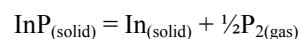
is reduced from 154.5 kJ mol⁻¹ down to 38.9 kJ mol⁻¹, and InP dissociates at 297 °C in the presence of atomic hydrogen with the concentration of 10^{15} cm⁻³. The total amount of N_2H_4 molecules is $4.8 \cdot 10^{17}$ cm⁻³ in our reactor with the volume of 1.5 L at 10 Torr. This amount of hydrazine is sufficient to produce molecular or atomic hydrogen with concentration that will be close to concentrations described in Ref.[30,31] Accordingly, the decrease of InP dissociation temperature in our experiments has a sound physical bases and seems quite realistic. Besides, as it was found in Ref.,[30,31] the phosphine (PH_3) appeared in the gaseous phase together with P_4, and the pressure of diphosphorus (P_2) increased up to 10^{-5} Torr. As a result of dissociation the In islands with diameters of several micrometers appeared at the surface of InP source. These In droplets together with metallic Ga, which was placed on the InP surface, served in our experiment as sources for the growth of NWs.

The transportation of Ga and In to the Si substrate surface needs the formation of volatile molecules. As it will be shown later, both elements were found in NWs grown on Si substrate located at 2 cm above the sources. The possible chemical reactions that lead to the formation of volatile suboxides will be suggested below to explain how these elements reached the Si substrate. The only volatile species that could perform this task are Ga and In suboxides (Ga_2O and In_2O). The water molecules diluted in hydrazine and some residual oxygen in the reactor are considered to be the only sources for producing oxides. Analyzing the Gibbs free energy of formation it was concluded that the first step in the formation of suboxides was the oxidation of metals to Ga_2O_3 and In_2O_3, with their subsequent reduction to suboxides using the hydrazine decomposition products (NH_2, NH, H). All these reactions have negative Gibbs free energy. The examples of chemical reactions are presented for the Ga source, but the similar tendency was observed also for the interaction of In source with the same reagents. The equations below have the tentative nature as they were calculated for 600 °C and atmospheric pressure while the initial pressure in our experiments was 10 Torr. 600 °C was selected as the reaction temperature because it corresponded to the temperature of our source. The first step is the oxidation of In and Ga:

$$2Ga + 3H_2O(g) = Ga_2O_3 + 3H_2(g) \quad \Delta G = -208 \text{ kJ mol}^{-1}$$

$$2Ga + 1.5O_2(g) = Ga_2O_3 \quad \Delta G = -807 \text{ kJ mol}^{-1}$$

Next step is the formation of volatile suboxides:

$$Ga_2O_3 + 2NH_2(g) = 2H_2O(g) + Ga_2O(g) + N_2(g)$$

$$\Delta G = -194 \text{ kJ mol}^{-1}$$

$$Ga_2O_3 + 4H(g) = Ga_2O(g) + 2H_2O(g)$$

$$\Delta G = -442 \text{ kJ mol}^{-1}$$

$$Ga_2O_3 + 4NH(g) = 2H_2O(g) + Ga_2O(g) + 2N_2(g)$$

$$\Delta G = -1188 \text{ kJ mol}^{-1}$$

The sign of ΔG determines only whether or not a chemical reaction will occur. The negative signs of ΔG in the equations listed above indicate that these reactions may take place spontaneously. However, the real amount of synthesized material depends on the reaction kinetics, i.e. on the rates of chemical processes. As a result of these reactions the volatile Ga$_2$O and In$_2$O molecules were produced. They reached the Si substrate heated up to 400 ºC and formed nanowires after reacting with ambient gases (P$_2$, P$_4$, PH$_3$, H$_2$O and O$_2$).
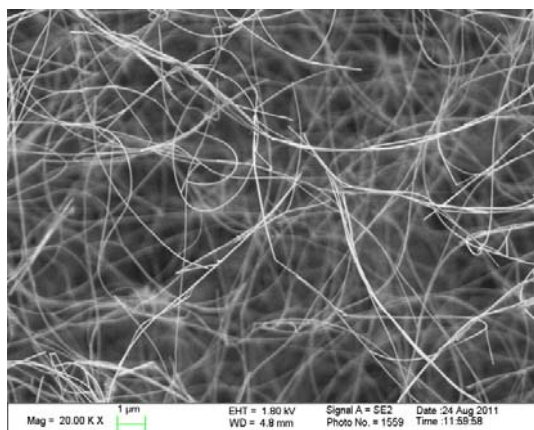
Figure 1. SEM image of nanowires grown on the Si substrate.
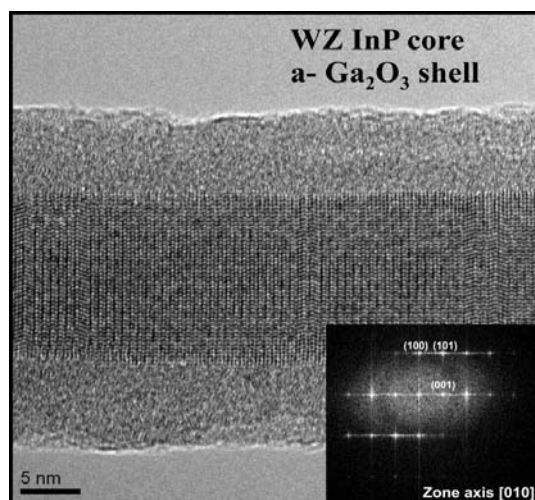
Figure 2. High resolution TEM image of InP/Ga$_2$O$_3$ nanowire with the average diameter of 28 nm (core – 14.9 nm). The Fast Fourier Transform (inset) confirms the WZ-type structure of the core.

Figure 1 presents SEM image of nanowires grown on the Si substrate. Some of them are quite long reaching tens of micrometers. The detailed structure of nanowires was studied using TEM and the results are presented in Figure 2 and Figure 3. As can be seen, the nanowires consist of crystalline core and the amorphous shell. The analysis of shell composition will be considered later. It should be noted that all nanowires presented on the surface of Si substrate have the heterogeneous core–shell structure and no nanowire were found with a homogeneous composition. Besides, no catalyst tips were observed, indicating that the growth proceeded through the vapor–solid mechanism with crystalline InP as a nucleation site.
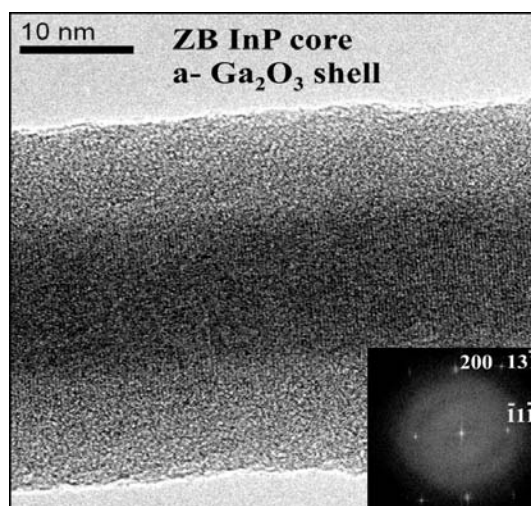
Figure 3. TEM image of ZB InP/amorphous Ga$_2$O$_3$ shell nanowire with the average diameter of 37.3 nm (core – 15.7 nm). Inset shows the ZB structure of nanowire that grows along [111] direction.

Analyzing the TEM results it was established that most nanowires have the cores of crystalline InP with wurtzite (WZ) structure. This is indicated in the Fast Fourier Transform in the inset of Figure 2, which shows a clear wurtzite pattern. In contrast to bulk non-nitride III–V materials which are usually zincblende (ZB) type, NWs predominantly crystallize as wurtzite type phases. Several different theoretical explanations for this behavior have been proposed. Recent calculations suggest that the WZ phase is energetically favorable for small NW radii.[32] Small radius results in a larger relative contribution of the nanowire sidewall surfaces to the total free energy. The surface dangling bonds at the nanowire lateral facets also have a significant influence on the formation of WZ structure. In Ref.[33] it was shown that the formation of wurtzite phase leads to an approximate 25 % reduction in the sidewall surface energy, and hence is thermodynamically favorable. A few core/shell nanowires were found, which preserved the ZB structure in spite of their small diameters (Figure 3). The reason for this phenomenon is not yet explained.

As it was mentioned earlier the WZ structured InP has significantly lower dangling bonds at the side walls as compared with ZB InP. This would cause the formation of less strained transition layer between WZ InP and the amorphous, unordered gallium oxide, because a low density of interface bonds will not alter significantly the side wall alignment.

Analyzing the side walls of InP in Figure 2 and Figure 3 one can detect the sharp interface between WZ InP and amorphous Ga$_2$O$_3$ in contrast to the rough and blurred ZB InP/Ga$_2$O$_3$ interface with possibly higher stresses.

Twin planes are the dominating stacking foults for III–V nanowires, which preferentially grow in the [111]B direction. Randomly positioned twin planes form naturally as a consequence of the relatively low twin-plane energy (about 10 mJ m^{-2} for InP).[34] This energy barrier is easily overcome at the typical growth temperatures and relatively high superstsuration used in general. For nanowires larger than ~ 40 nm in diameter, the twinning between wurtzite and zinc-blende phases becomes quite frequent.[35] The same was observed in our nanowires. TEM images reflected the gradual increase of twin density for NWs with larger diameters, as it is demonstrated in Figure 4. The high density of rotational twins is clearly seen in TEM image of NW with the diameter of 74 nm (Figure 4). It is interesting to note that some rare twins can be clearly detected also in the high resolution TEM image in Figure 2.
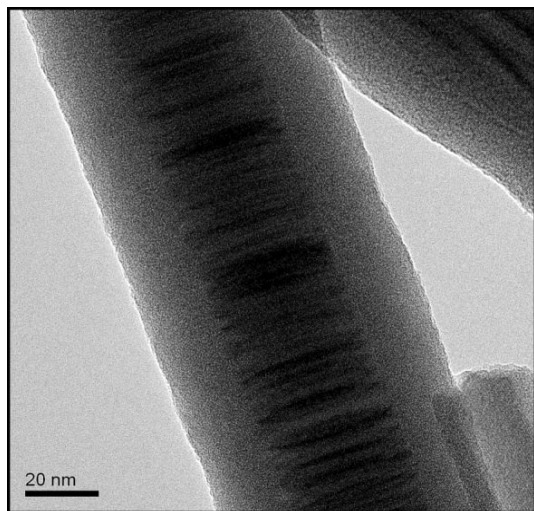
Figure 4. TEM image of InP/Ga$_2$O$_3$ core–shell nanowire with rotational twins. The diameter of nanowire was 74 nm.
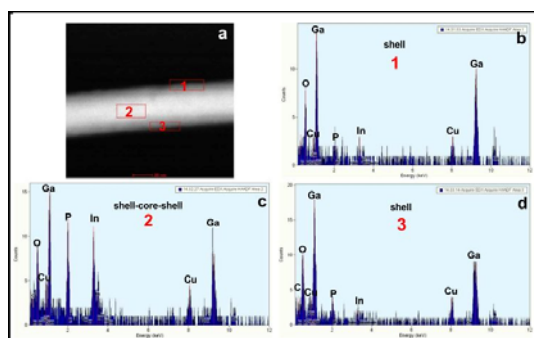
Figure 5. HAADF STEM image of the nanowire (a) and EDX spectra of rectangular regions marked in (a) (b – d).
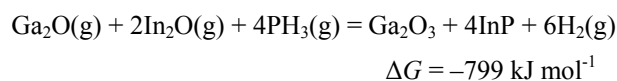
The composition of a shell was studied by the EDX method. Figure 5 shows the HAADF STEM image of NW and three EDX spectra. Two of them were obtained from the rectangular shell regions marked by 1 and 3 (Figure 5b and 5d). Figure 5c reflects the composition of two shells and a core, because the focused excitation electron beam was

transmitting the NW, initiating the simultaneous emission of X-rays from core and two shells located above and behind the core. As can be seen, In an P peaks increase in the core, while shells contain mainly Ga and oxygen. Comparison of these results with EDX spectrum of pure Ga$_2$O$_3$ powder confirmed that the shell material can be attributed to the gallium(III) oxide. The peak of Cu in the spectra comes from the copper TEM grid.

When considering the possible mechanisms of the core-shell nanowire formation it should be emphasized that the gallium oxide shell has an amorphous structure, as it was produced at 400 ºC. This temperature is insufficient for the crystallization because, to our knowledge, 610 ºC is the minimum temperature for the growth of crystalline Ga$_2$O$_3$ (β modification) using Ga$_2$O precursors.[36] According to TEM images in Figures 2 – 4, the thickness of Ga$_2$O$_3$ shell is quite uniform along the nanowire length and it depends on the nanowire core diameter. It increases with the increase of a core diameter, indicating that the core and shell were produced simultaneously, through the unified chemical reaction.

From the other hand, if we assume that Ga$_2$O$_3$ was formed separately, then it would appear on the substrate in the form of the deposited amorphous layer, because the formation of amorphous nanowires in the absence of templates (tubular pores or template nanowires) is impossible. According to the assumption made above, the Ga$_2$O$_3$ shell was deposited on the side walls of InP nanowire core during the whole growth time. This would lead to the formation of tapered core–shell NWs. However the tapering was not observed in SEM and TEM images of grown nanowires, confirming that the assumption concerning the separate deposition of Ga$_2$O$_3$ shell was wrong and the shells were formed simultaneously with InP through the spontaneous chemical reaction.

The spontaneous growth is a process driven by the reduction of Gibbs free energy realized by chemical reaction or phase transformation.[37] Taking into account the existing precursors the possible chemical reactions that may lead to the spontaneous formation of InP-Ga$_2$O$_3$ core-shell nanowires were analyzed. We suggest following reactions for the formation of core–shell NWs at $T = 400$ ºC:

$$Ga_2O(g) + 2In_2O(g) + 4PH_3(g) = Ga_2O_3 + 4InP + 6H_2(g)$$

$$\Delta G = -799 \text{ kJ mol}^{-1}$$

$$Ga_2O(g) + 2In_2O(g) + 2P_2(g) = Ga_2O_3 + 4InP$$

$$\Delta G = -798 \text{ kJ mol}^{-1}$$

$$Ga_2O(g) + 2In_2O(g) + P_4(g) = Ga_2O_3 + 4InP$$

$$\Delta G = -672 \text{ kJ mol}^{-1}$$
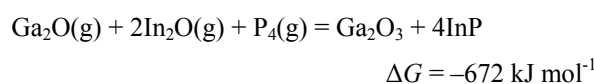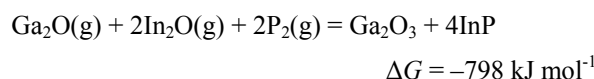
These reactions have sufficiently high negative values of Gibbs free energy to form the core-shell nanowires with the composition that were observed in our experiments. It should be emphasized once again that these reactions have the tentative nature because the standard state thermodynamic data were used for their calculation. However, we consider that these equations can truly convey the main tendencies of NW formation observed in this work.

Taking into account that the whole Si substrate was covered with a thick "mat" of nanowires, like those depicted in Figure 1, it can be concluded that considered chemical equations have significant reaction rates.

Conclusions

The core-shell nanowires were grown on Si substrate at 400 ºC in the hydrazine vapor diluted with 3 mol. % H_2O. The crystalline InP and solid Ga served as source materials for the growth of nanowires. According to TEM and EDX data the nanowires consisted of wurtzite InP core with an amorphous Ga_2O_3 shell. The twinned planes appeared in WZ InP core at increased nanowire diameters. Based on the obtained results and possible chemical reactions, the following mechanism was proposed for the growth of core-shell nanowires: pyrolytic decomposition of hydrazine caused the appearance of active intermediate NH_2, NH and H species in the vapor. At elevated temperatures the crystalline InP source was also dissociated to In and phosphorus precursors. At source temperatures close to 600 ºC, due to the interaction of In and Ga sources with water molecules and hydrazine decomposition products the volatile Ga_2O and In_2O were formed. These molecules reached the Si substrate which was heated to 400 ºC. The final chemical reaction involved Ga_2O_3, In_2O_3 and phosphorus precursors. As a result of a spontaneous reaction the Ga_2O_3 and InP phases were produced and segregated. The InP crystallized as a core while Ga_2O_3 created the amorphous shell, because the growth temperature was insufficient for its crystallization.

Acknowledgments

References

[1] Qi, W., Luo, L., Qian, H.-Sh., Ouyang, G., Nanda, K. K., Obare, Sh. O., (Eds.). *Core–Shell Nanostructures: Modeling, Fabrication, Properties, and Applications. J. Nanomater.*, **2012** – Special Issue.

[2] Reiss, P., Protiere, M., Li, L., *Small*, **2009**, *5*, 154.

[3] Choi. H.-J., In: *Nano Science and Technology* (Ed. G.-C. Yi), *Berlin – Heidelberg: Springer–Verlag,* **2012**.

[4] Lei, D., Shen, Y. T., Feng, Y., Feng. W., *Sci. China: Technol. Sci.*, **2012**, *55*, 903.

[5] Kim, S., Shim, W., Seo, H., Bae, J. H., Sung. J., Choi, S. H., Moon, W. K., Lee, G., Lee, B., Kim, S.-W., *Chem. Commun.*, **2009**, *10,* 1267.

[6] Lu, M.-Y., Zhou, X., Chiu, C.-Y., Crawford, S., Gradečak, S., *ACS Appl. Mater. Interfaces*, **2014**, *6*, 882.

[7] Marcu, A., Enculescu, I., Vizireanu, S., Birjega, R., Porosnicu, C., *Dig. J. Nanomater. Biost.*, **2013**, *8,* 597.

[8] Dennis, A. M., Piryatinski, A., Mangum, B. D., Park, Y.-Sh., Htoon, H., Hollingsworth, J. A., *243rd American Chemical Society National Meeting &Exposition. Chemistry of Life. Section: Basic Research in Colloids, Surfactants and Nanomaterials.* **2012**, San Diego, Pub. # 97.

[9] Mushonga, P., Onani, M. O., M. Madiehe, A., Meyer. M., *J. Nanomater.,* **2012,** *2012,* 11 pp.

[10] Li, X., Li, X., Chen, N., Li, X., Zhang, J., Yu, J., Wang, J., Tang, Zh., *J. Nanomater.,* **2014,** *2014,* 7 pp.

[11] Le, D. T. T., Trung, D. D., Chinh, N. D., Binh, B. T. T., Hong, H. S., Duy, N. V., Hoa, N. D., Hieu, N. V., *Curr. Appl. Phys.,* **2013,** *13,* 1637.

[12] Jang, Y.-G., Kim, W.-S., Kim, D.-H., Hong, S.-H., *J. Mater. Res.,* **2011**, *26*, 2322.

[13] Chen, C., Lin, Sh.-Sh., Lin, T.-J., Hsu, Ch.-L., Hsueh, T. J., Shieh, T.-Y., *Sensors*, **2010**, *10,* 3057.

[14] Park, S., Jun, J., Kim, H. W., Lee, C., *J. Korean Phys. Soc.*, **2009,** *55,* 1591.

[15] Zhong, M. Y. Li, Tokizono, T., Zheng, M., Yamada, I., Delaunay, J.-J., *J. Nanopart. Res.*, **2012,** *14,* 10 pp.

[16] Hayden, O., Greytak, A. B., Bell, D. C., *Adv. Mater.* **2005,** *17*, 701.

[17] Hu, Y., Kuemmeth, F., Lieber, Ch. M., Marcus. Ch. M., *Nat. Nanotechnol.*, **2012,** *7,* 47.

[18] Choi, H.-J., Johnston, J.C., He, R., Lee, S. K., Kim, F., Pauzauskie, P., Goldberger, J., Saykally, R. J., Yang, P. *J. Phys. Chem. B,* **2003,** *107,* 8721.

[19] Hochbaum, A. I. , Yang. P., *Chem. Rev.*, **2010**, 110, 527.

[20] Hollingsworth, J. A., Werner, J. H., Htoon, H., Piryatinski, A., Schaller, R., Ghosh, Y., Dennis, A. M., Keller, A. M., Mangum, B., Hannah, D. C., In: *Proc. Int. Conf. "Lasers and Electro-Optics (CLEO)".* **2013,** San Jose.

[21] Jishiashvili, D., Chkhartishvili, L., Kiria, L., Shiolashvili, Z., Makhatadze, N., Jishiashvili, A., Gobronidze, V., *Nano Studies*, **2013,** *7,* 27.

[22] Dirtu, D., Odochian, L., Pui, A., Humelnicu, I., *Cent. Eur. J. Chem.*, **2006**, *4,* 666.

[23] Pakdehi, Sh. G., Salimi, M., Rasoolzadeh, M., *Res. Appl. Mech. Eng.,* **2014,** *3,* 21.

[24] Konnov, A. A., Ruyck, J. D., *Combust. flame,* **2001**, *124,* 106.

[25] Zheng, M., Cheng, R., Chen, X., Li, N., Li, L., Wang, X., Zhang, T. *Int. J. Hydrogen Energy,* **2005**, *30,* 1081.

[26] Jishiashvili, D., Kiria, L., Shiolashvili, Z., Makhatadze, N., Miminoshvili, E., Jishiashvili, A. *J. Nanosci.,* **2013,** *2013,* 10 pp.

[27] Xie, T., Jiang, Z., Wu, G., Fang, X., Li, G., Zhang, L., *J. Cryst. Growth,* **2005**, *283,* 286.

[28] Gao, Y. H., Bando, Y., Sato, T., *Appl. Phys. Lett.,* **2001**, *79,* 4565.

[29] Vallés, C., Núñez, J. D., Benito, A. M., Maser, W. K., *Carbon*, **2012,** *50*, 835.

[30] Gorbenko, V. I., Gorban, A. N., *Radiophysics (in Russian).* **2012,** *1,* 7.

[31] Gorbenko, V. I., Shvets, J. A., Gorban. A. N., In: *III–Nitride Based Semiconductor Electronics and Optical Devices and Thirty-Fourth State-of-the-Art Program on Compound Semiconductors (SOTAPOCS XXXIV).* In: *Proc. Int. Symp. 2001 – Technol. & Eng.* **2001**, Electrochem. Soc., 218.

[32] Akiyama, T., Nakamura, K., Ito, T., *Phys. Rev. B.*, **2006**, *73,* 235308, 6 pp.

[33] Dubrovskii, V. G., Sibirev, N. V., *Phys. Rev. B.,* **2008**, *77,* 035414, 8 pp.

[34]Li, J., Wang, D., la Pierre, R. R., *Advances in III–V Semiconductor Nanowires and Nanodevices. Bentham Sci. Publ.* **2011.**

[35]Moewe, M. J., Thesis (Elect. Eng. & Comp. Sci.). **2009,** Univ. CA Berkeley.

[36]Han, N., Wang, F., Yang, Z., Yip, S. P., Dong, G., Lin, H., Fang, M., Hung, T. F., Ho, J. C., *Nanoscale Res. Lett.,* **2014,** *9,* 6.

[37]Cao, G., Limmer. S. J., *Oxide Nanowires and Nanorods.* In: *Encyclopedia of Nanoscience and Nanotechnology, Am. Sci. Publ.,* **2004**

PREPARATION OF SILVER NANOPARTICLES IN SILVER NITRATE SOLUTION BY USING TANNIN

T. Pavliashvili[a], T. Kalabegishvili[b,c], M. Janjalia[b], E. Ginturi[b] and G. Tsertsvadze[d]

Presented at 3rd International Conference "Nanotechnologies", October 20 – 24, 2014, Tbilisi, Georgia (Nano – 2014)

Preparation of silver nanoparticles in silver nitrate solution using tannin as a reductant and sodium carbonate-as a solution stabilizer was performed. Spectrophotometric and electron-microscopic methods were used to investigate the process of synthesis of silver nanoparticles. The effect of microwave power on the formation of nanoparticles was analyzed.

* Corresponding Authors
  E-Mail: pavliashvilitamaz@yahoo.com;
  kalabegi@yahoo.com
[a]   Institute of Micro and Nanoelectronics, Tbilisi, Georgia
[b]   I. Javakhishvili Tbilisi State University, E. Andronikashvili Institute of Physics
[c]   Ilia State University, Institute of Applied Physics, Tbilisi, Georgia
[d]   Georgian Technical University, Republic Center for Structure Researches (RCSR), Tbilisi, Georgia

Introduction

Silver nanoparticles possess unique physical, chemical and bactericidal properties, which determine their widespread use in electronic, optical and sensor devices, in medicine, etc. Among chemical methods of preparation of silver nanoparticles, the most generally employed is the method of formation of silver nanoparticles in water solution by using various reductants and stabilizers.[1,2] Toxic substances such as sodium borhydride and hydrazine are often used as reductants. Hence, it is topical to develop the technology of preparation of silver nanoparticles by using nontoxic agents (reductants and solution stabilizers). The use of the exposure to high-energy physical fields, such as the microwave electromagnetic one, in combination with chemical methods is quite efficient. As is well known, the elevation of temperature is one of widespread methods for acceleration of chemical reactions. When a solution is heated up by traditional methods, heat transfer occurs gradually via heat conduction, convection or radiation mechanism, which is always associated with emergence of a temperature gradient. In case of the exposure to microwave radiation, the whole body of the solution is heated up immediately.[3,4]

Experimentals

We used tannin as a reductant and sodium carbonate, being the source of carbonate ions, as a stabilizer. Distilled water was user for dilution. The solution was prepared at room temperature. The solutions of tannin and sodium carbonate (10^{-5} M) were added to silver nitrate solutions of

$5 \cdot 10^{-4}$ and $5 \cdot 10^{-3}$ M under continuous stirring. The pH value of the prepared solutions was equal to 5.77. The silver nitrate solution was placed in microwave oven Saturn equipped with a rotating table. The microwave power was 600 W and the exposure duration was 4 min.

The optical absorption spectra of the prepared solution were measured with an UV-vis spectrometer Sintra 10e. The spectra were detected at room temperature.

Electron microscope Jem100–SX was used for the electron-microscopic investigation.

Results and Discussion

The silver nanoparticles prepared in silver nitrate solutions using tannin as reducing agent and sodium carbonate as source of carbonate ion as stabilizer were performed at at pH=5.77. The exposure for microwave irradiation was 4 min. The UV-Vis spectra of the reaction mixtures formed with or without microwave irradiation contain well-defined plasmon bands with a peak at 420 nm, which is characteristic of silver nanoparticles (Figures 1 and 2).
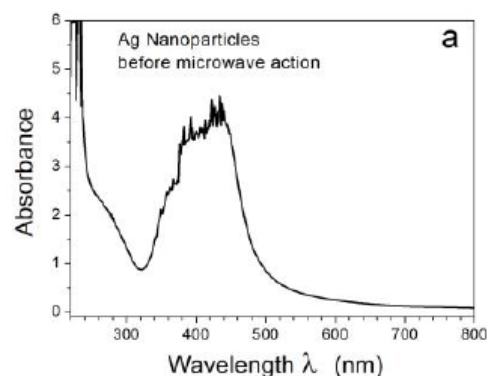

Figure 1. Absorption spectra of silver nanoparticles in silver nitrate solution $5 \cdot 10^{-3}$ M
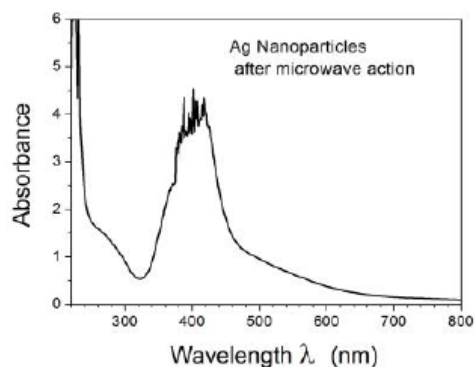
Figure 2. Absorption spectra of silver nanoparticles in silver nitrate solution (10^{-3} M) after the exposure to the microwave field.

The obtained nanoparticles proved to be crystalline (Fig. 3). The size distribution of nanoparticles before microwave action is shown in Figure 4. As it can be seen from the microphotographs, the solutions of nanoparticles generally contained spheroids 15 – 20 nm in size. A small amount of larger nanoparticles 30 – 40 nm in size was also observed.
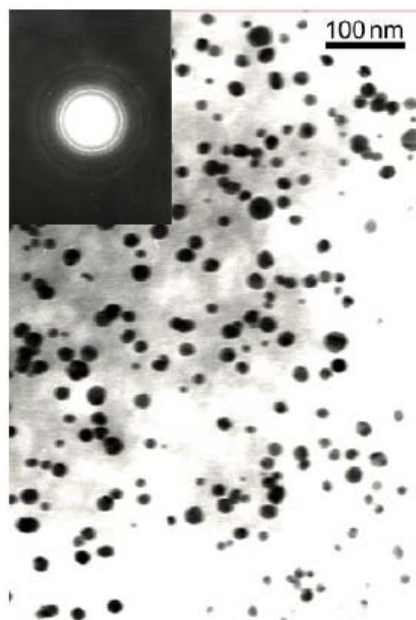

Figure 3. Electron-microscopic microphotograph of silver nanoparticles before the exposure to the microwave field.
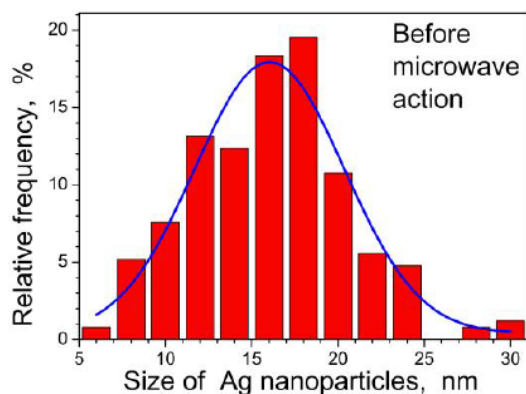
Figure 4. Size distribution of silver nanoparticles before the exposure to the microwave field.
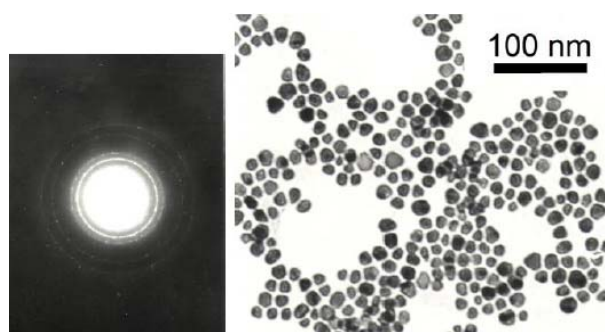
Figure 5. Electron-microscopic microphotograph of silver nanoparticles after the exposure to the microwave field.

The Electron-microscopic investigation performed after the exposure of the samples to the microwave field showed that there had taken place changes in the shape and size of the nanoparticles (Figure 5). The size of nanoparticles reduced and made up 10–15nm. To analyze the size distribution of nanoparticles, we constructed relevant histograms. IT is seen that, after the exposure to the microwave field, the nanoparticles were distributed within a much narrower size range than before it (Figure 6).
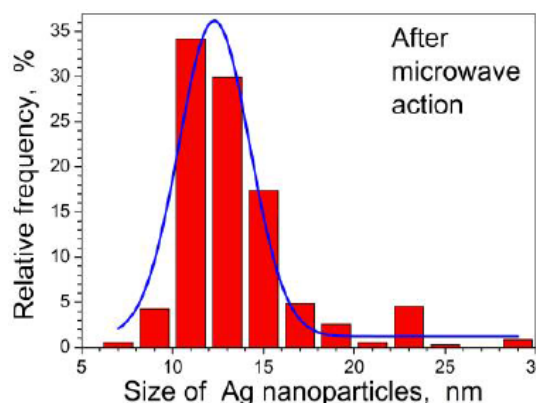

Figure 6. Size distribution of silver nanoparticles after the exposure to the microwave field.

The experiments showed that sodium carbonate possessed good stabilizing properties. The prepared solution of silver nitrate containing silver nanoparticles retained its properties during a month, and there was no aggregation.

Conclusions

Using tannin as a reductant and sodium carbonate as a solution stabilizer proved to be a promising method for the preparation of silver nanoparticles. The experiments showed that sodium carbonate possessed good stabilizing properties, and the prepared silver nanoparticle containing silver nitrate solution retained its properties during a month, and there was no aggregation. The method we propose is realized without using highly toxic substances, does not require expensive reagents.

References

[1]Krizova, H., Wiener. J., Synthesis of silver nanoparticles using condensed and hydrolysable tannins. In: *Proc. 5th Int. Conf. EU.* **2013**, Brno, 600-604.

[2]Kruglyakov, Yu. A.m Kudrinskij, A. A., Olenin, A. Yu.m Lisichkin, G. V., *Chem. – Uspekhi*, **2008**, *77*, 242-250.

[3]Berdonosov, C. C., Berdonosova, D. G., Znamenskaya, I. V., Chem. Technol., **2008**, *3*, 2-8.

[4]Pavliashvili, T., Kalabegishvili, T., Ginturi, E., Lomidze, L., Tsertsvadze, G., Abramishvili, G., *Nano studies*, **2012**, *6*, 101-104.

A NEW METHOD FOR THE SYNTHESIS OF NANOPARTICLES FOR BIOMEDICAL APPLICATIONS

Sh. Kekutia[a]*, L. Saneblidze[a], V. Mikelashvili[a], J. Markhulia[a], R. Tatarashvili[a], D. Daraselia[b] and D. Japaridze[b]

New chemical synthesis methods for producing nano-sized iron oxides particles and producing biocompatible polymer coated nanoparticles in the solution has been investigated. A new particle processing device for making high performance nanomaterials as well as their applications in medicine has been developed by applying electrohydraulic technique for nanohomoganization. Biomedical application requires the biocompatible super paramagnetic iron oxide nanoparticles (SPIONs), which are stable and well dispersed in water at physiological pH or in physiological salinity. In order to obtain biocompatible SPIONs, particles of 10-15 nm size have been synthesized and these SPIONs have been coated with ascorbic acid. Vibrating Sample Magnetometer studies (VSM) were carried out to study the effect of phase transformations on the magnetic properties of the nanoparticles. The samples were analyzed by VSM at room temperatures to find the saturation magnetization. The ascorbic acid coated iron oxide nanoparticles were found to be well dispersed in water as they have a hydrophilic outer surface containing hydroxyl and amine groups. This hydrophilic outer surface is likely to enhance their bioactivity. Therefore they may become a very good drug carrier for biomedical applications.

* Corresponding Authors
    E-Mail: kekuka@yahoo.com, vmikelashvili@gmail.com
[a]   V. Chavchanidze Institute of Cybernetics of the Georgian Technical University, Sandro Euli Str. 5, Tbilisi 0186, Georgia
[b]   I. Javakhishvili Tbilisi State University, Department of Physics, I.Chavchavadze Ave. 3, 0179 Tbilisi, Georgia

Introduction

Magnetic nanofluids or nanoferrofluids refer to the stable colloidal suspensions of magnetic nanoparticles (MNPs) in a carrier liquid. Usually, the MNPs have core-shell structures in which the cores are made of magnetic crystallites and the shells are made of organic or inorganic substances. For most nanoferrofluids, the size of magnetic cores is in the range of several nanometers to tens of nanometers, containing only a simple magnetic domain. Owing to their extremely small size, the MNPs exhibit super paramagnetic behavior. This means that the MNPs are magnetically responsive but remain nonmagnetic in absence of the magnetic field. The colloidal MNPs can be readily dispersed in a liquid to form a nanoferrofluid.

MNPs are used in important biological applications, including magnetic bioseparation, detection of biological entities (cell, protein, nucleic acids, enzyme, bacteria, virus, etc.), clinic diagnosis and therapy (such as magnetic resonance image), magnetic fluid hyperthermia (MFH), targeted drug delivery and biological labels. In general, it is crucial to choose the materials for the construction of nanostructure materials and devises with adjustable physical and chemical properties. On this basis, iron oxide MNPs are the strong candidates for such devices, and the application of iron oxide MNPs in in vitro diagnostics has been in practice for nearly half a century.[1] In the last decade, investigations with several types of iron oxides have been carried out in the field of MNPs, among which magnetite

(Fe$_3$O$_4$) and maghemite (γ–Fe$_2$O$_3$) are the very promising reagents since their biocompatibility has already been proven.[2]

It is a technological challenge to control size, shape, stability, and dispersibility of MNPs in desired solvents. Iron oxide MNPs have a large surface-to-volume ratio and therefore possess high surface energies. Consequently, they tend to aggregate so as to minimize the surface energies. Moreover, the naked iron oxide NPs have high chemical activity, and are easily oxidized in air (especially magnetite), generally resulting in loss of magnetism and dispersibility. Therefore, providing proper surface coating and developing some effective protection strategies to stabilize iron oxide MNPs is very important and that was the aim of the present work. In general, these strategies comprise grafting of or coating the particles with organic molecules, including small organic molecules or surfactants, polymers, and biomolecules, or coating with an inorganic layer, such as silica, metal or nonmetal elementary substance, metal oxide or metal sulfide. It is worth noting that in many cases the protecting shells not only stabilize the NPs, but can also be used for further functionalization.[3]

The most conventional method for obtaining Fe$_3$O$_4$ or γ-Fe$_2$O$_3$ is by co-precipitation.[4] The size and shape of the iron oxide NPs depends on the type of salt used (such as chlorides, sulfates, nitrates, perchlorates, etc.), the ferric and ferrous ions ratio, the reaction temperature, the pH value, ionic strength of the media, and the other reaction parameters (e.g. stirring rate, rate of addition of basic solution).

But this method needs to be improved in order to cause mono dispersity, which is necessary for biomedical applications. To achieve this, we for the first time used the electrohydraulic treatment (Yutkin treatment) in a well-known scheme for the synthesis of nanoparticles in order to significantly reduce the radius scatter of particles.[5,6]

The proposed approach, as shown by preliminary studies, significantly improves the dispersion of solution. Strong oscillations associated with electrohydraulic technique, additionally produce resonant treatment of chemically synthesized particles. The process involves a series of controlled explosions produced by electro impulse discharges at the high voltage (electro sparks) in liquid. The discharges generate massive shock waves and impulses of pressure that create homogenization action on nanoparticles. As a result, radii of the particles become almost same and the particle solubility in water is increased.

Hence, in this study, we have focussed mainly on the development of various strategies for the preparation, structure determination and magnetic properties of various surface functionalized iron oxide MNPs and their applications. The properties of functionalized iron oxide nanoparticles, synthesized via chemical method and electrohydraulic technique have been compared.

We have carried out preparation of the magnetic colloid by a modified co-precipitation method along with electrohydraulic treatment, with further magnetite stabilization. The samples are analyzed by VSM at room temperature to find the saturation magnetization of ascorbic acid coated iron oxide NPs.

Experimentals

Synthesis of Magnetic Nanoparticles

We have synthesized magnetite nanoparticles by chemical precipitation of mixed iron(III) chloride hexahydrate ($FeCl_3 \cdot 6H_2O$) and iron(II) chloride tetrahydrate ($FeCl_2 \cdot 4H_2O$) or iron(II) sulfate heptahydrate ($FeSO_4 \cdot 7H_2O$) with iron ions in 2:1 molar ratio, with in NaOH or NH_4OH solution at room or relatively high temperature (80ºC) and in air or under a flow of nitrogen. Chemical co-precipitation consists of two processes, nucleation i.e. formation of centres of crystallization and subsequent growth of particles.

The co-precipitation process was carried out by Massart's procedure,[4] which involves drop wise addition of NaOH solution into the mixture of the aqueous solutions of iron salts, at either the room temperature or 80°C under continuous vigorous magnetic or mechanical stirring. The reactions can be represented as follows.

$$FeCl_2 \cdot 4H_2O + 2FeCl_3 \cdot 6H_2O + 8NaOH =$$
$$Fe_3O_4 + 8NaCl + 20H_2O \qquad (1)$$

$$FeSO_4 \cdot 7H_2O + 2FeCl_3 \cdot 6H_2O + 8NaOH =$$
$$Fe_3O_4 + Na_2SO_4 + 6NaCl + 17H_2O \qquad (2)$$
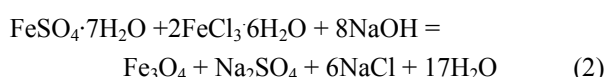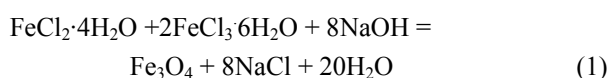
The solution turned from brown to black indicating the formation of magnetite (Fe_3O_4). The solution was subjected to magnetic stirring for 60 min to ensure nucleation and growth of magnetite particles. On the completion of the precipitation process, the separation of two phases was observed, a solid phase and a supernatant liquid. The black solid phase was magnetically decanted (while the

supernatant was carefully removed) and was repeatedly washed with deionized water in order to ensure the elimination of residual salts. The precipitate was further washed with ethanol to remove traces of water and was subsequently heated for some minutes to ensure evaporation of ethanol. The ready magnetic nanofluid was then subjected to electrohydraulic treatment for about 1 h to yield finally the highly dispersed magnetic nanofluid. After electrohydraulic treatment the black precipitates were again washed with deionized water. At last 10% of ascorbic acid from weight of nanoparticles was added into the mixture to modify the Fe_3O_4 magnetic nanoparticles and the mixture was heated to 80°C under magnetic stirring. After 1 h of modification, the resulting Fe_3O_4 magnetic nanoparticles (black precipitate) were collected from the solution by magnetic separation and washed several times with deionized water and ethanol. The pH was adjusted to 8 in order to simulate a biological environment. Two hours of sonication were required to obtain well dispersed nanoparticles. The nanoparticle solutions were then left at room temperature.

During synthesis of nanofluids, attention is required to be paid to the size of the nanoparticles. The dimensions should be homogeneous with little departure from the average size. The existing methods of synthesis do not provide an acceptable quality in this respect. To ensure high quality, we turned to the electrohydraulic technique. To achieve this, we created a device, which is presently a stationary pilot equipment. The electrohydraulic technique was used during one of the stages of synthesis of magnetic nanofluid. By using the device created by us, it is possible to homogenize a nanofluid and therefore to have highly dispersed magnetic nanofluid. The scheme of the electrohydraulic device is shown in Figure 1.
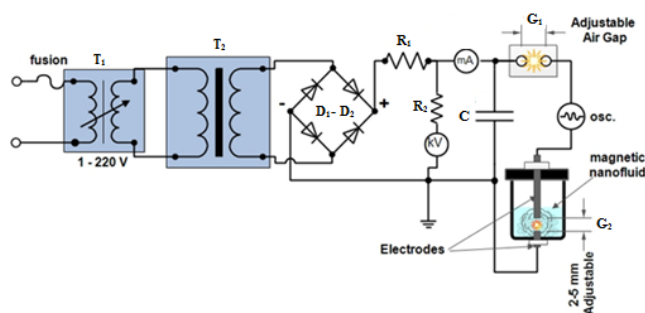

Figure1. A schematic diagram of the electrohydraulic device. The device has a power supply, transformer (T_1, T_2), charger resistance (R_1, R_2), storage capacitor (C), electrodes with adjustable air gap for creating a spark (G_1), and submerged electrodes with adjustable air gap for creating a spark (G_2).

The magnetic properties of the polymer-coated magnetite nanoparticles were measured in water solution state at room temperature using a Standard 7300 Series Lake Shore Cryotronics vibrating sample magnetometer (Criogenic Ltd, UK). The hysteresis loop of each sample was measured over a range of applied fields from −3 to +3 T with a resolution of 10^{-4} emu.

Results and Discussion

VSM was used to evaluate magnetization of the MNPs as a function of an applied external magnetic field (*H*) between –3 and 3 Tesla. Based on the obtained VSM curve at room temperature, magnetic behaviours of the MNPs can be analyzed. For example, at room temperature, the zero magnetic remanence (when H is zero), and the hysteretic loop feature indicates that the MNPs are super paramagnetic. Also, from the plateau part of the VSM curve, saturation magnetization can be determined. The dependences of magnetic momentum of MNPs on magnetic field are shown in Figures 2-5.

The Fig. 2 presents the dependence of the magnetic moments of magnetic nanofluid on the applied external magnetic field at room temperature for bare magnetic nanoparticles synthesized by chemical co-precipitation method and in Figure 3 the same dependence, only the nanoparticles were additionally treated by electrohydraulic technique.
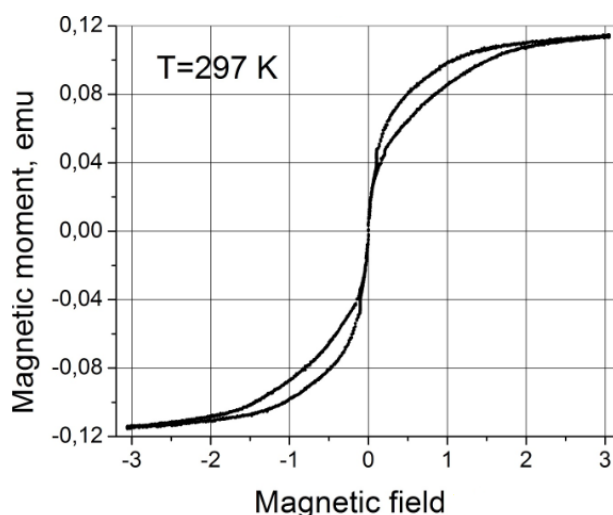
Figure 2. The dependence of magnetic moment of bare MNPs on magnetic field.
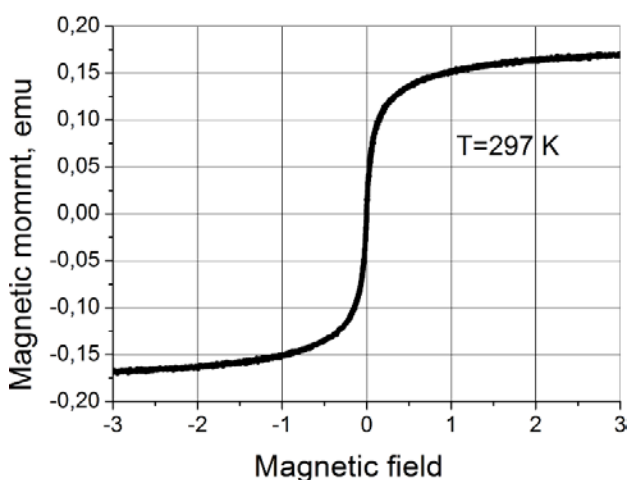
Figure 3. The dependence of magnetic moment of electrohydraulically treated bare MNPs on magnetic field

Figures clearly indicate the super paramagnetic nature of the produced nanomaterials. Also from these figures, we can conclude that the electrohydraulic treatment significantly improves the magnetic properties of nano materials and the magnetic particles are more dispersed.

Figure 4 presents the dependence of the moments of ascorbic acid-coated magnetic nanoparticles on applied external magnetic field, the same dependence is shown in Figure 5, when the magnetic nanoparticles were treated by electrohydraulic device before the coating. Ascorbic acid coated magnetic nanoparticle formulation and its therapeutic uses have recently been introduced. Hydrophilic ascorbic acid derivatives such as ascorbyl glycoside have been used not only as antioxidants, as food and pharmaceutical excipients but also as stabilizer.
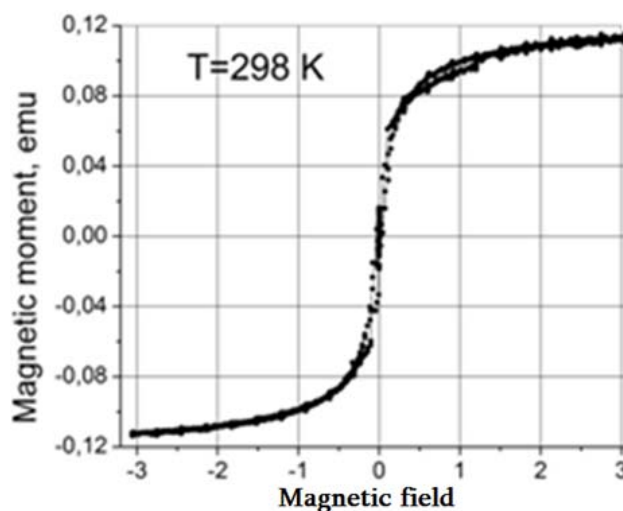

Figure 4. The dependence of the magnetic moment of ascorbic acid coated MNPs on magnetic field.
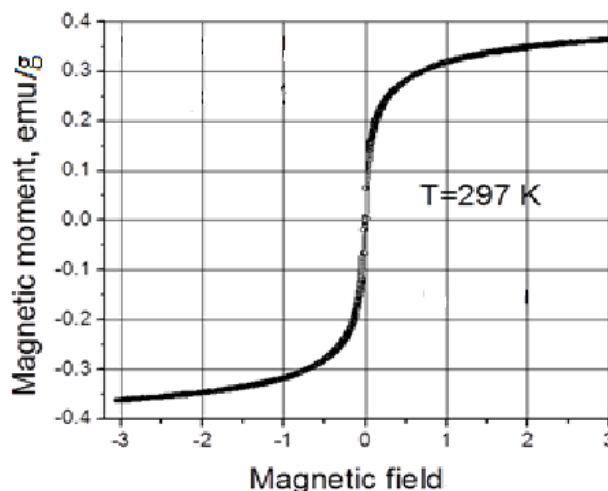

Figure 5. The dependence of the magnetic moment of ascorbic acid coated and electrohydraulic treated MNPs on magnetic field.

Nanoparticle technology is being incorporated into many areas of molecular science and biomedicine. Because nanoparticles are small enough to enter almost all areas of

the body, including the circulatory system and cells, they have been and continue to be exploited for basic biomedical research as well as clinical diagnostic and therapeutic applications. To study the coating mechanism, it is very helpful to work with particles that are uniform in size and shape.

The main advantage of the precipitation process is that a large amount of nanoparticles can be synthesized. However, the control of particle size distribution is limited, because only kinetic factors are controlling the growth of the crystal. To avoid this drawback we utilize the electrohydraulic phenomenon.

To make the best use of nanoparticles and solve the problems of their applications, the development of nanomaterial processing techniques is essential. New synthesis methods for producing nano-sized oxides particles and producing biocompatible nano-composite particles in the solution phase have been reported in this article. In addition, electrohydraulic treatment method (e.g. homogenization) is briefly discussed.

This research work aims to solve the aggregation problem, eventually leading to a cheap, effective, and safe nanoparticle-necessary for cancer treatment. Magnetite (Fe_3O_4) is also less toxic to organic systems. *The* loop shows a significant increase in magnetic moment for electrohydraulic treated nanoparticles as compared to those without this treatment. Synthesized magnetite, Fe_3O_4, is a powerful magnetic vector for penetration into the tumor. For biomedical applications such as MRI, drug-delivery and hyperthermia, the nanoparticles have to be biocompatible, have a large enough moment for targeting and display super paramagnetic behavior.

Presented figures show the magnetization curve as a function of magnetic field for the uncoated and coated nanoparticles. From the figures, no hysteresis curve was observed, which indicates the characteristic super paramagnetic behavior of the nanoparticles. The magnetic moment values of the MNPs were found between 0.120 and 0.175 emu, depending from their treatment method (with or without electrohydraulic treatment).

In addition, the magnetization decreases from the plateau value and reaches zero when the magnetic field is removed. The behavior shows that the iron oxide nanoparticles correspond to the single-crystal domain exhibiting only one orientation of the magnetic moment and are magnetite in structure.

So, it was found from VSM studies that the magnetic nanoparticles show no diamagnetic contribution and are small enough to exhibit super paramagnetic behaviour, thus, they are of particular interest for drug targeting systems, as they do not retain any magnetism after removal of a magnetic field.

Acknowledgments

References

[1]Krishanan, K. M., *IEEE Trans. Magn.,* **2010**, *46*, 2523-2558.

[2]Laurent, S., Forge, D., Port, M., Roch, A., Robic, C., vander Elst, L., Muller, R. N., *Chem. Rev.,* **2008**, *108*, 2064-2110.

[3]Veiseh, O., Gunn, J. W., Zhang, M., *Adv. Drug Delivery Rev.,* **2010**, *62*, 284-304.

[4]Massart, R., *IEEE Trans. Magn.,* **1981**, *17*, 1247-1248.

[5]Yutkin, L. A., *Electrohydraulic Effect and Its Application in Industry* (in Russian), Mashinostroenie, Leningrad, **1986**.

[6]Mikelashvili, V., Markhulia, J., Kekutia, Sh., Tatarashvili, R., *2nd Int. Conf. "Nanotechnologies" (Nano – 2012),* Tbilisi, **2012**, 30-37.

HOT EXPLOSIVE CONSOLIDATION OF NANOSTRUCTURED TUNGSTEN–SILVER PRECURSORS

A. Peikrishvili[a]*, B. Godibadze[a], E. Chagelishvili[a], M. Tsiklauri[a] and A. Dgebuadze[a]

Different precursors of refractory nanostructural tungsten-silver (W-Ag) composites were consolidated into cylindrical billets by hot explosive consolidation (HEC) method. Different types of compositions with a nanoscale W phase (100 nm) and coarse matrix phase of Ag were consolidated to near theoretical density under and above of melting point of silver (940 – 1050°C). The intensity of loading in all experiments was around 10GPa. The combination of high temperatures and two stage explosive densification processes was found to be beneficial to the consolidation of the nanostructural W based composites, resulting in high densities, good integrity, and good electronic properties. The structure and property of the samples depends on the value of consolidation temperature and dimension of consolidated particle. It was observed that for the W-Ag based composites, application of high temperature and consolidation of precursors near melting point of silver 940 °C gives samples without cracking with high value of density and uniform distribution of two phases. The features of structure/property relationship depending on phase content and consolidation conditions have been discussed.

* Corresponding Authors
     E-Mail: akaki.peikrishvili@stcu.int
[a]   G. Tsulukidze Institute of Mining, Tbilisi, 0186, Georgia

Introduction

In recent years, tungsten (W)-based heavy alloys have received increased use in both commercial and industrial spheres. Most heavy alloys consist of W particles embedded in matrix of other metals or their alloys such as iron, nickel, or copper.[1] In particular, W–silver (Ag) composites may have potential uses as heat dissipation materials in the microelectronic devices that are prone to failure at high operating temperatures,[2] as diverter plates in fusion reactors,[3] or in special industrial (e.g., aerospace) applications.

Experimental studies relating the mechanical properties of samples formed from nanocrystalline precursor powders show that these ultra-fine grained materials are fundamentally different from their normal, coarse-grained counterparts. These materials often have very unusual properties for instance, they are ultra-hard and wear-resistant, have an ideal compatibility of strength and elasticity, and are characterized by super-plasticity. When the average grain size is less than or equal to the wavelength of visible light, the material will also have unique optical, thermal, electrical and magnetic properties as well. Therefore, a decrease of the grain size and concomitant control of the defect substructure of the grains seems to be a promising way to improve properties of these materials. At present, there are various methods (e.g., cold or hot isostatic compaction in vacuum or in other media) for the manufacturing of monolithic specimens using precursor powders ranging from micro- to sub micrometer- to nanometer-sized powders (i.e., covering the visible-light spectrum from infrared to ultraviolet wavelengths).

All existing conventional technologies, alongside with imparting positive properties, introduce certain negative features. Nanometer-scale grains are very sensitive to heating, with increasing temperatures, these powders begin to grow rapidly. Typically, this grain growth is non-uniform and its overall impact causes imperfections and non-uniformity in the nanostructure and, as a result, monolithic materials formed under such conditions do not have the unique physical and mechanical properties that are otherwise would be intrinsic to nanostructural materials.

Usually, decreasing the compaction or sinter temperature during low-temperature processing does not lead to a desirable outcome. In this case, the relatively large free surface area of the powder precludes the attainment of high-density samples. Additionally, at low temperatures, the required interfacial grain-to-grain boundaries do not form and this is especially true during the compression and consolidation of refractory and ceramic powders. Thus, such samples are characterized with high level of porosity and, therefore, inadequate physical or mechanical properties.

Nevertheless, sufficient experience has been accumulated to provide solutions to some of the aforementioned problems. The idea is to apply high temperatures, up to 1200 °C, to the samples and carry out rapid consolidation at the hot, elevated temperature, conditions. Heating of the powders or alloys before loading assists in increasing the sample's plasticity. As a result, common boundaries, interfacial solid solutions, intermediate layers (in the case of joining of bulk alloys), and other beneficial features are formed. The high value of recrystalization temperature of W prevents or suppresses grain growth processes.

A further novelty of the proposed, non-conventional approach is that the consolidation of solid samples in a cylindrical geometry from sub micrometer- and nanometer-sized W-Ag blend powders is performed in two stages:

(a) First stage: preliminary explosive compression of the precursor powder blend is carried out at room temperature with a loading intensity of 5 – 10 GPa to increase the initial density and to activate the particle surfaces in the blend;

(b) Second stage: the same, already densified cylindrical sample is loaded again by a primary explosive shock wave with a loading intensity of 10GPa, but at a temperature between 20 – 1100 °C.

It is expected that the effect of the first consolidation stage is to primarily compact the precursor powder without causing a change in its microstructure. The second, hot consolidation stage is performed on the pre-compacted samples by heating in an electrical furnace. The high recrystalization temperature of W significantly decreases the probability of the thermally activated grain growth process (as it was demonstrated in the preliminary experiments), while the high intensity shock wave compression imparts fluidity to the grain surfaces thereby increasing their plasticity and, thus generate the particle-particle bonds that would otherwise not form under the quasistatic conditions.

In this study we undertook the consolidation of tungsten–(10–50) wt. % silver (W–(10–50)Ag) powder mixtures into cylindrical rods using hot explosive consolidation (HEC) processes. Two types of nanometer-scale W–Ag blend compositions with 100 nm W, and 10 & 50 % 5 µm Ag were consolidated to near theoretical density at different temperatures up to 1100 °C. The shockwave loading intensity was about 10 GPa.

The intent of the investigations were to determine if the use high temperatures and the two-stage shock wave processing resulted in acceptable homogeneity, good bonding between the metal particles and absence of voids. These micro-structural features would provide an indication of the degree of mechanical and thermal property uniformity. Of further interest was a determination of the mechanical properties (elastic modulus and internal friction losses) as a function of Ag content, processing method, and processing temperature. Lastly, the electromagnetic properties (electrical resistivity and diamagnetic susceptibility) were measured. These results are described.

Experimental

In these experiments, we have used nominally nanometer-sized W powders from US Research Nanomaterials, Inc., USA and coarse Ag powders from Inframat "Advanced Materials", Manchester, USA

The W–(10–50)%Ag precursor powder blends were prepared from commercially available elemental powders. In turn these powders were consolidated into cylindrical rods using hot explosive consolidation (HEC) methods. Three types of W–Ag were consolidated to near theoretical density. The coarse Ag powders used in experiments have dimensions around 5µm. The shock wave loading intensity was about 10GPa, The temperatures during compaction were different and maximum value was under 1100 °C.

The explosive compaction process is carried out using a cylindrical scheme of dynamic loading described earlier.[4]

Typically, the shock waves are initiated with the use of industrial explosives and their mixtures with varying amounts of ammonium nitrate.

After consolidation, the HEC samples were subjected to micro-structural characterization and micro-hardness measurements. Coefficient of Thermal Extension (CTE) was measured to determine compatibility of the W–Ag composite to other materials, such as semiconductors and ceramics that would be part of the electronic assembly in need of heat dissipation. The electro-magnetic properties (electrical resistivity and magnetic susceptibility) along with, the mechanical properties (elastic modulus and internal friction) were also measured.

Results and Discussion

Using scanning electron microscopy (SEM) it was found that while the nanometer powders did indeed contained nanometer-scale particles, they were heavily agglomerated into multi-micrometer agglomerates.

Cross-section view of the sample of W–Ag billets fabricated by two-stage HEC at 1050 °C with nanometer-sized W–10%Ag and the W–50%Ag are presented in Figure 1a and 1b respectively. A comparative examination of the samples revealed major differences in their macrostructures. Both samples contain radial cracks but sample with high content of silver (1b) contains an additional zone formed along the whole length in the central part of billet. Macrostructure (Figure 1b) of the newly-formed zone in the central part of HEC sample has definite structure that differs from another part in colour and could be result of over compression and collision of shock waves in the central part of sample. This effect is popularly known as Mach's effect.
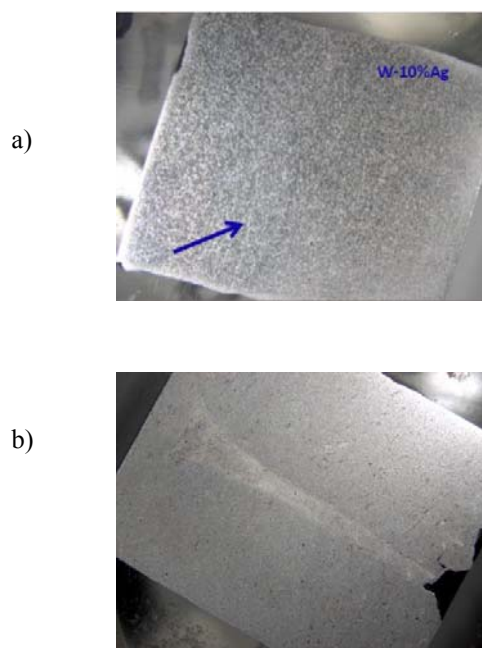

Figure 1. The Optical micrographs view of HEC W–Ag samples consolidated at 1050 °C with 10GPa. a) W–10%Ag at 6×. Radial cracking is observed b) W–50%Ag at 6×. Compositional segregation and radial cracking are observed.

Figure 2 illustrates the microstructures of different parts of the W–10%Ag composition presented in the Figure 1. Extensive radial cracking was observed in samples of the W–10%Ag composite (Figures 2a). The explosive forming of the dense W–10%Ag composite achieved good bonding between W and Ag particles. This is shown in Figures 2b, taken at 100× and 1000× correspondently. As expected, the Ag particles, initially of 8 – 10µm in size, tended to agglomerate in nodules of approximately 30µm in size in average around large areas of W in the W–10%Ag sample.

consolidated precursors in contrast to processes in solid state when consolidation mechanism works through plastic flow of particle surfaces with further formation of joint boundaries.

Undoubtedly existence of liquid bonding phase during consolidation under shock wave compression facilitates the formation of solid solutions and new chemical compounds under similar loading conditions. On the other hand, liquid phase shock wave consolidation gives opportunity to use low detonation velocity explosives with higher pulse duration and to easily fabricate high density billets. Figure 3 illustrates compositional mapping of HEC W–10%Ag sample presented on Figure 1a.
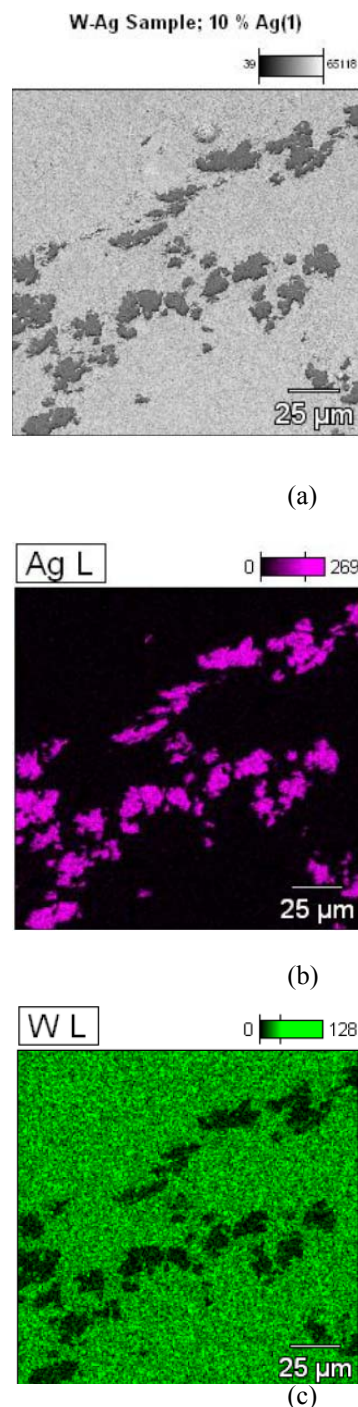
a)

b)

Figure 2. Microstructures of W–10%Ag HEC sample obtained at 1050 °C temperature with intensity of loading 10GPa. (a) Significant radial cracking is observed. (b) Distribution of Ag particles (in dark colour) – good bonding between W and Ag particles.

The formation of radial cracks in high density W–10%Ag composites after hot explosive consolidation at1050 °C, when bonding phase is in liquid state, seems to have both advantages and disadvantages. As a matter of fact liquid phase consolidation, when the bonding phase is liquid, provides extrusion of Ag phase on the shock wave front during the compression process and better densification of

(a)

(b)

(c)

Figure 3. The location and distribution Ag (lavender color) and W (green color) in the matrix (grey colour) is shown.

As mentioned above, distribution of phases of W−10%Ag showed that Ag precursor, initially of 8 – 10 μm in size, agglomerates into nodules of average size of approximately 15 to 30 μm.

The appearance of agglomerates of silver phase in some regions of HEC W−10%Ag may be explained as an influence of high temperature and low intensity of compression that may not provide good extrusion and uniform distribution matrix of silver phase in whole volume of obtained billets.

In order to evaluate influence of silver content in W−Ag phase on consolidation process, HEC method was applied under similar experimental conditions on W−50%Ag composites also. Figure 4 illustrates the microstructures of different parts of the W−50%Ag composition presented in the Figure 1b.
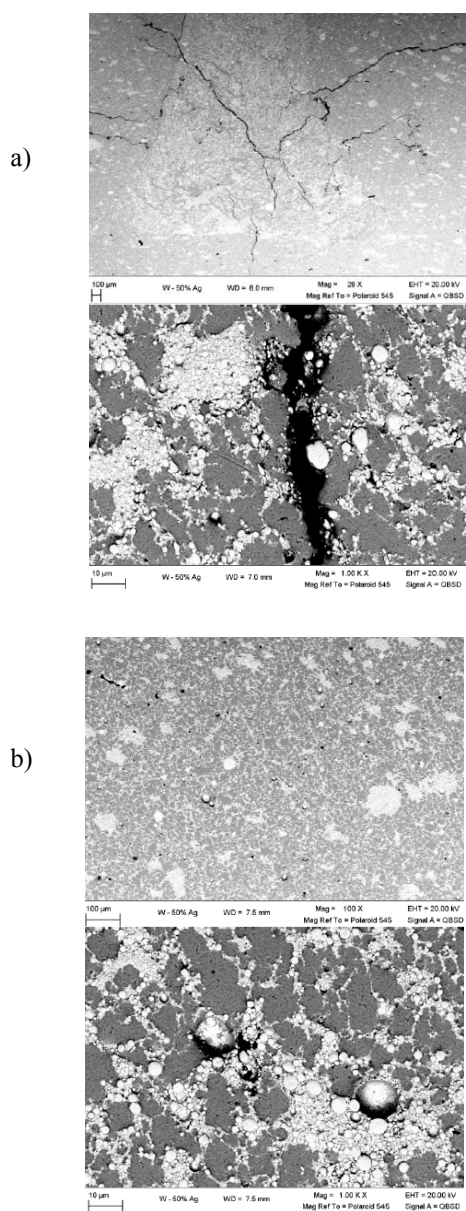
As it is seen from microstructure the increase in of silver content in W−Ag composition has substantial influence on quality of HEC samples. Under similar experimental conditions, the obtained billets are characterized with compositional segregation accompanied with intensive cracking in the central part of sample.

The formation of tungsten rich central zone that is different from other parts may be explained by assuming transportation of heavy W phase by shock wave front during of movement to central part during the explosive compression. As for the observed intensive cracking in the same central region, it must be result of "Makh's" steam effect. The intensive collision of shock waves in central part of billets causes an increase of the internal temperature and thermal stresses during the rapid cooling results in formation of intensive cracking.
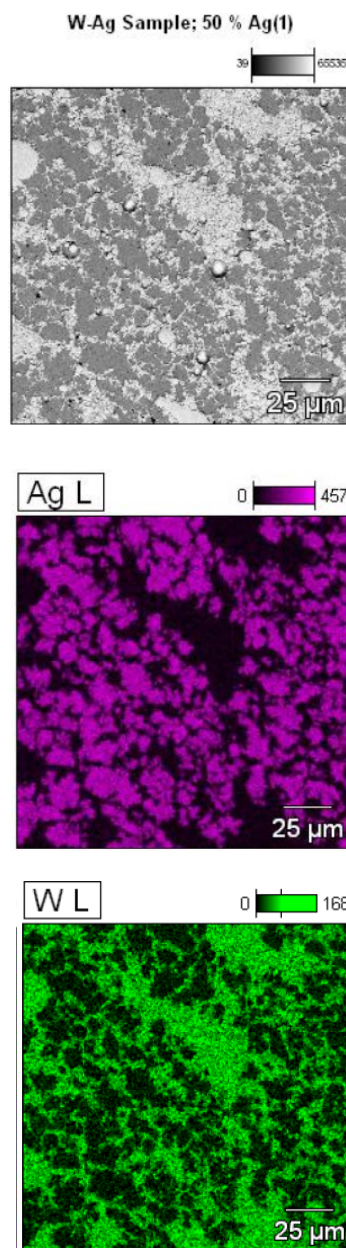

Figure 4. Microstructures of W−50%Ag HEC sample obtained at 1050 °C temperature with intensity of loading 10 GPa. (a) A large area of compositional segregation is visible at the centre of sample. This area is W rich and shows in light grey colour. Numerous cracks are also visible. (b) Distribution of Ag particles (in dark colour) –good bonding between W and Ag particles.

Figure 5. The location and distribution Ag (lavender colour) and W (green colour) in the matrix (grey colour) is shown. The Ag powder, initially of 8 – 10μm in size, agglomerates into nodules of average size of approximately15 to 30μm .

The Figure 5 illustrates compositional mapping of HEC W–50%Ag sample presented in Figure 1(a).

It is seen from the distribution of the combining phases that in the W–50%Ag also, Ag phase, initially of 8–10μm in size, agglomerates into nodules of average size of approximately 15 to 30μm. Similar observations were recorded for W–10%Ag case.

The presence of numerous cracks in the W–10%Ag samples would be detrimental to a uniform heat dissipation path. Non-uniform heat dissipation could create hot spots and potentially damage an electronic component or assembly. The presence of a W rich area at the centre of the W–50%Ag sample could also contribute to uneven heat conduction and heat dissipation from the assembly.

Therefore the fabrication of crack free W–Ag composites of near theoretical density with good bonding and uniform distribution of consisting phases is necessary for further successful application W–Ag composites in the modern microelectronics.

In order to reduce thermal stresses and cracking during the consolidation process and to evaluate the role of temperature on the consolidation process of W–Ag precursors, the HEC was performed under melting point of silver at 940 °C with loading intensity up to 10 GPa. Figure 6 illustrates the microstructures of different parts of the resulting consolidate of W–10%Ag composition.

As it's seen from microstructures the central part and whole volume of HEC sample are free from cracks and no traces of compositional segregation are observed. The agglomerated separate W particles with internal micro cracks might be observed at higher magnification that could be result of bad mixing and matching of sizes between the W and Ag phases.

The results of hardness testing of HEC W–Ag samples depending on consolidation conditions are presented in Table 1.

Table 1. The value of hardness for HEC W–Ag composites depending on consolidation temperature obtained at intensity of loading 10 GPa.

Compacted Composites	Temp. of compaction, °C	Loading, g	Microhardness HV, kg mm^{-2}
W–5%Ag	1000	50	331.5
W–10%Ag	940	50	248.5
W–10%Ag	1050	50	208.2
W–50%Ag	1050	50	47.5

As it is seen from table the content of silver phase in composition influences the value of hardness and sample with 5 % Ag content has the best value of hardness at 331 HV. The high consolidating temperature with increased Ag content in composition leads to reduced hardness value, it might be result of intensive cracking and compositional segregation. As stated above W–Ag materials could be used for heat dissipation from electronic devices that are prone to failure at high operating temperatures. Currently, materials such as copper–tungsten (Cu–W) and aluminum–silicon carbide (AlSiC) are used in industry for heat dissipation.

The above-mentioned characterizations were to determine if explosive consolidation resulted in acceptable homogeneity, good bonding between the metal particles, and absence of voids. These microstructural features provide an indication of the degree of uniformity in mechanical and thermal properties.
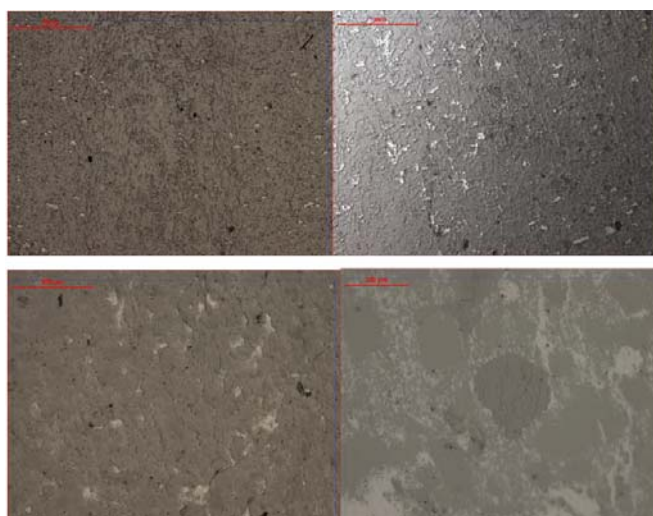

Figure 6. Microstructures of different regions of W–10%Ag HEC sample obtained at 940 °C temperature with loading intensity under 10 GPa. The sample is free from cracks in whole volume of billet and good bonding between W and Ag was observed.

CTE was measured to determine compatibility of the tungsten–silver (W–Ag) composites to other materials, such as semiconductors and ceramics that would be part of the electronic assembly in need of heat dissipation. CTE was determined by Thermal Mechanical Analysis (TMA) from –60 to 350 °C at 10 °C min^{-1} with three cycles (heat–cool–heat). Two heating cycles were used: from –60 to 20 °C and from 50 to 350 °C. The CTE from the two heating cycles is averaged from each lot of material. These values are shown in Table 2 below.

Table 2. Measurements of coefficient of thermal expansion, μm/m °C.

Composition	Coefficient of thermal expansion	
	–60 to 20 °C	50 to 350 °C
W–10%Ag	5.5	7.5
W–50%Ag	9.5	13.7

Conclusions

Cracking on both of the W–Ag samples consolidated above melting point of silver were observed. The cracking is severe and can compromise the mechanical integrity of the sample as well as the uniformity of the heat dissipation. In actual applications, this lack of mechanical integrity and non-uniformity may lead to hot spots which could damage the devices in need of heat dissipation.

The CTE of the W–Ag samples, shown in Table 2, compares well with the CTE of other materials commonly used by industry for this application, namely Cu–W and AlSiC. Reported CTE values for Cu–W are 6.5 for W–10%Cu and 8.3 for W–20%Cu. The CTE for the W–10%Ag

sample of 5.5 to 7.5 (μm m°C^{-1} or ppm K^{-1}) is within this range. CTE values for AlSiC range from 8.0 to 15 (ppm K^{-1}) depending on the composition ratios. Cu–Mo, another material used for its high thermal conductivity has a CTE of 7.2 to 11 (ppm K^{-1}) depending of the ratio of Cu to Mo. The CTE, 9.5 to 13.7 (μm m°C^{-1}), of the W–50%Ag sample measured in this investigation is within this range. The CTE of a low temperature co-fired ceramic, measured under the same conditions as the W–Ag samples was 4.4 to 6.4 (μm m°C^{-1}).

Compositional segregation was observed in the centre of the W–50%Ag sample. A large area, rich in W is visible around the longitudinal axis. This segregation raises concern about the uniformity of properties, such as thermal conductivity, of the sample.

The measurement of the thermal conductivity of the samples was not in the scope of this initial evaluation, but the presence of numerous cracks in the samples would be detrimental to a uniform heat dissipation path. Non-uniform heat dissipation could create hot spots and potentially damage an electronic component or assembly. The presence of a W rich area at the centre of the W–50%Ag sample could also contribute to uneven heat conduction and heat dissipation from the assembly.

References

[1]Bose, A., German, R. M., *Developments in the Sintering of Tungsten Heavy Alloys- Sintering Theory and Practice.* John Wiley & Sons, **1996**.

[2]German, R. M., Hens, K. F., Johnson, J. L., Bin, Y., *Proceedings of the 1993 International Conference on Powder Metallurgy and Particulate Materials,* MPIF Press, Princeton, **1993,** 189-202.

[3]Boscary, J., Suzuki, S., Nakamura, K., Suzuki, T., Akiba, M., *Proceedings of the 1997 4th International Symposiumon Fusion Nuclear Technology,* Elsevier, **1999,** 537-542.

[4]Kecskes, L., Peikrishvili, A., Godibadze, B., Chagelishvili, E., Tsiklauri, M., Hot Explosive Consolidated nanostructured Ta–Al Composites, *Proc.e 11th Int. Symp. Explosive Prod.f New Mater.s: Sci., Technol., Business, Innovations (EPNM–2012) XI EPNM*, Strasbourg, **2012**.

POSSIBILITIES OF PHYSICAL METHODS IN DEVELOPMENT OF MICROBIAL NANOTECHNOLOGY

T. L. Kalabegishvili,[a,b] I. G. Murusidze,[b] E. I. Kirkesali,[a] A. N. Rcheulishvili,[a] E. N. Ginturi,[a] E. S. Gelagutashvili,[a] N. E. Kuchava,[a] N. V. Bagdavadze,[a] M. V. Janjalia,[a] D. T. Pataraya,[c] M. A. Gurielidze,[c], M. V. Frontasyeva,[d] I. I. Zinicovscaia,[d] S. S. Pavlov,[d] G. I. Tsertsvadze[e] and V. N. Gabunia[f]

The results of applied investigations carried out by some groups of Georgian scientists in the field of nanobiotechnology using different physical and chemical methods are presented. A number of new strains of the terrestrial actinomycetes isolated from soils and rocks of Georgia as well as the blue-green alga *Spirulina platensis* were used as the templates for production the noble metal nanoparticles on examples of silver and gold. A variety of spectral and analytical methods was applied to determine optimal conditions of synthesis and characterize the synthesized nanoparticles. The features of the used research methods and some results obtained with them are detail described. The advantages of each method and their ability to characterize the process of synthesis of nanoparticles are shown.

* Corresponding Author
E-Mail: kalabegi@yahoo.com
[a] I. Javakhishvili State University, E. Andronikashvili Institute of Physics, Tbilisi, Georgia
[b] Ilia State University, Institute of Applied Physics, Tbilisi, Georgia
[c] Georgian Agrarian University, S. Durmishidze Institute of Biochemistry and Biotechnology, Tbilisi, Georgia
[d] Joint Institute for Nuclear Research, Dubna, Russia
[e] Georgian Technical University, Republic Center for Structure Researches (RCSR), Tbilisi, Georgia
[d] I. Javakhishvili State University, P. Melikishvili Institute of Physical and Organic Chemistry, Tbilisi, Georgia

Introduction

During the last years the use of physical properties and biosynthetic activities of microbial cells for the synthesis of nanosized materials has emerged as a novel biotechnological approach.[1] Numerous bacteria, fungi and yeasts have been exploited for biosynthesis of highly structured metallic nanoparticles. Microbial cells have developed specific mechanisms for surface functional groups (peptides, proteins, nucleic acids) interacting with metal ions in the aqueous solutions which result nanoparticles production.[2-4] Gold and silver nanoparticles have potential applications in electronics, information technology, catalysis, medicine, pharmacology, sensing and photonics. In medicine they have shown therapeutic potential in oncology, cardiology, immunology, neurology and endocrinology.[5-7]

Currently there is a great need to develop new alternative, easy and eco-friendly methods to search the new effective microbial strains producing gold and silver nanoparticles. The great interests present the microorganisms with potential in medical applications such as the actinomycetes as well as the blue green alga *Spirulina platensis*. The collaboration of Georgian scientists during many years carried out investigations to development of biotechnological methods using different strains of

microorganisms.[8-13] In last years the number studies of microbial synthesis of gold and silver nanoparticles was carried out.[14-18] In present paper the experience of use the different physical and chemical methods in these investigations is described and their possibilities are discussed.

Materials and methods

Materials

Georgia is a country with areas characterized by extreme microbial and plant biodiversity. The special interest present the microorganisms have great potential for biotechnology with medical applications. The study of different microorganisms characteristic for Georgia environment was performed in collaboration few groups of Georgian scientists. The distribution of different strains of terrestrial actinomycetes in various types of soils, rocks and rhizosphere of Georgia has been studied. Several groups of new microorganisms isolated in Georgia for the first times were studied as models for developing methods of nanoparticle biosynthesis. The blue-green alga *Spirulina platensis* was also used for obtaining gold and silver nanoparticles for medical and pharmaceutical application. The studied microorganisms are presented in Table 1 below.

The methods of cultivation of studied bacterial culture and production of biomass with gold and silver nanoparticles are described in detail elsewhere [14-18].

Methods

A variety of spectral and analytical methods was used to characterize the synthesized gold and silver nanoparticles.

Table 1. Studied microorganisms

Names of bacteria	Species of bacteria	Site of bacteria isolation
Arthrobacter genera	*Arthrobacter globiformis* 151B *Arthrobacter oxydans* 61B	Isolated from the Kazreti region in Georgia
Streptomyces genera	*Streptomyces glaucus* 71MD *Streptomyces sp.* 211A	Isolated from the rhizosphere of soybeans in Georgia Isolated from the Cinnamonic calcareous soil of Sagarejo region in Georgia
Extremophile bacteria	*Streptosporangium spp.* 94A	Isolated from the Black soil of Shiraki Valley in Georgia
Thermophilic actinomycetes	*Thermoactinomycete spp.* 44Th *Thermomonospora spp.* 67Th	Isolated from the red soil of Adjara Region Isolated from the cinnamonic calcareous soil of Tetritskaro region in Georgia
Blue-green alga	*Spirulina platensis*	Strain IPPAS B-256

The UV–vis (ultraviolet–visible) spectra of the samples were recorded by a spectrophotometer "Cintra 10" (GBC Scientific Equipment Pty Ltd, Australia) with a wavelength range of 190 – 1100 nm.

X-ray diffraction (XRD) measurements were made with a Dron–2.0 diffractometer. The BCV–23 X-ray tube with the Cu anode (Cu$K\alpha$: λ = 1.54178 Å) was used as a source of radiation.

Transmission Electron Microscopy (TEM) was performed using the JEOL SX–100 (Japan) equipment operating at 100 kV. The samples were prepared by placing a drop of solution with the gold or silver nanoparticles on carbon-coated TEM grids.

Scanning Electron Microscopy (SEM) was carried out using the Quanta 3D FEG, USA/ Systems for Microscopy and Analysis, (Moscow, Russia). Operational features of the microscope used in the experiment: magnification 100 – 200000 ×; voltage 1 – 30 kV. Microprobe analysis of gold and silver nanoparticles clusters was conducted with the energy-dispersive X-ray analysis spectrometer (EDAX, USA).[19]

Flame atomic absorption spectrometry (AAS) with "Analyst–800" and "Beckman–495" spectrometers was used for gold and silver determination in the experimental samples.

The gold and silver concentrations as well as the elemental content of samples were determined using neutron activation analysis (NAA) at the reactor IBR–2 of the Frank Laboratory of Neutron Physics of the Joint Institute for Nuclear Research (Dubna, Russia). The experimental equipment and irradiation conditions of samples are described elsewhere.[20] The NAA data processing and determination of element concentrations were performed using Genie 2000 software.[21]

In addition to study biosorption process on the bacterial cells during nanoparticles production the method of equilibrium dialysis with atomic-absorption analysis were used.

The method sonication of bacterial biomass by ultrasound generator (35 kHz, 10-30 min) was used for intensification of processes nanoparticles production.

Results and discussion

The process of microbial synthesis of metal nanoparticles in a solution of a metal compound can be viewed as a metal ion reduction by the biomolecules, proteins and enzymes of bacterial cells. For example, the aggregation of silver nanoparticles takes place at the reduction of silver ions from Ag (I) to Ag (0) in a reaction of silver nitrate ($AgNO_3$) water solution with bacterial suspension. Similarly, the gold nanoparticles formation takes place at Au(III) ions reduction to Au(0) in a chloroauric acid ($HAuCl_4$) aqueous solution.

The ultraviolet-visible UV-vis spectrometry was mainly used for detection nanoparticles and determination experimental conditions of the nanoparticles synthesis by the bacterial cells.

The nanoparticles exhibit localized surface plasmon resonances at visible and near-infrared frequencies leading to sharp peaks in their spectral extinction.[22] The extinction is the result of collective excitation of conducting electrons due to strong interaction between the metallic nanoparticles and the incident electromagnetic radiation.[23]

In UV-vis surface plasmon resonances absorption spectra the peaks at 530 nm for gold and 425 nm for silver were observed.

In each case for determination the optimal concentrations of aqueous solutions $AgNO_3$ and $HAuCl_4$ the dose-dependent formation of nanoparticles was carried out at concentrations 10^{-2} – 10^{-4} M. Figure 1 shows the example of results of such experiment for gold nanoparticle production (a) and absorbance maximums versus the dose of $AgNO_3$ at silver nanoparticles production (b) in biomass of *Spirulina platensis*. In all cases the optimal concentration for bacterial synthesis of nanoparticles turned out to be 10^{-3} M. It should be noted that the all spectra obtained for the gold nanoparticles are better pronounced that those for the silver nanoparticles.
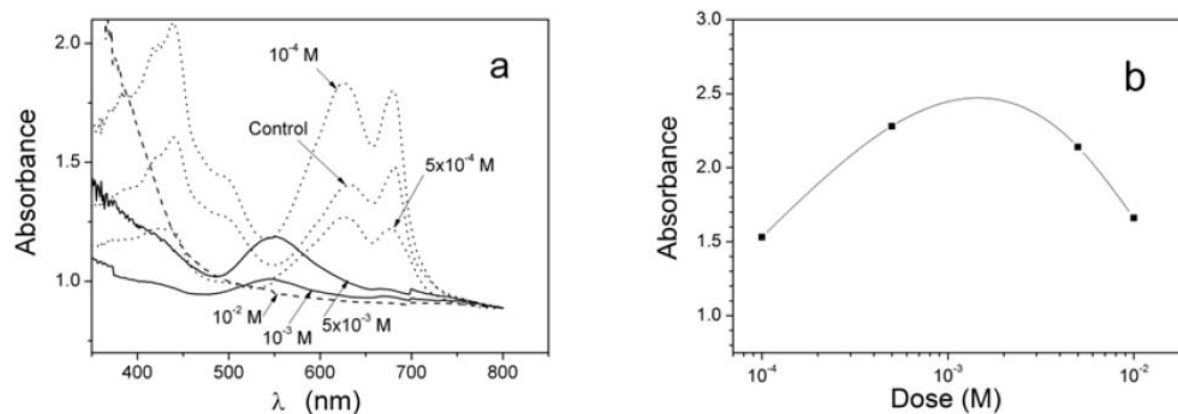
Figure 1. UV-vis spectra of gold nanoparticles in *Spirulina platensis* biomass obtained for different HAuCl₄ doses (a) and silver nanoparticles absorbance maximums versus the dose of AgNO₃ (b).
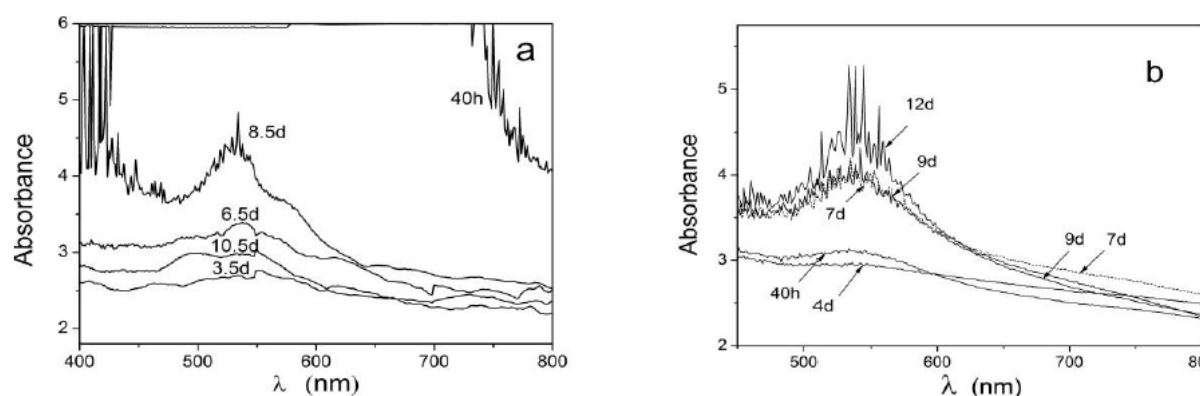

Figure 2. The absorption spectra of Au nanoparticles detected in the suspension of *Streptomyces glaucus* 71MD (a) and *Arthrobacter oxydans* 61B (b) at different time reaction with HAuCl₄ 10^{-3} M water solution.

Figure 2 shows the UV-vis spectra recorded from suspension of actinomycetes *Streptomyces glaucus* 71MD (a) and *Arthrobacter oxydans* 61B (b) for different reaction times with HAuCl₄ 10^{-3} M water solution. The presented spectra exhibit the appearance of Au absorption peak at 530 nm, which increases in intensity as a function of time of reaction. The shapes of these peaks show that gold nanoparticles have mainly the spherical shapes. The results of these experiments show that the favorable reaction time for Au nanoparticle synthesis using biomass *Streptomyces glaucus* 71MD is hours whereas in case of *Arthrobacter oxydans* 61B it is days.

The example of X-ray diffraction (XRD) spectra obtained for gold nanoparticles in biomass *Arthrobacter oxydans* 61B after reaction with 10^{-3} M HAuCl₄ (chloroauric acid) for 12 days (Figure 3a) and silver nanoparticles in biomass *Spirulina platensis* after reaction with AgNO₃ (silver nitrate) for 1 day (Figure 3b) are shown. As it is seen from Figure3 a number of Bragg's reflections corresponding to a face centered cubic (fcc) structure of gold (or silver) are seen here: four characteristic peaks (111), (200), (220) and (311). The obtained results clearly show that the gold nanoparticles formed by reduction of Au (III) and Ag (I) ions by the cells of *Arthrobacter oxydans* 61B and *Spirulina platensis* are crystalline in nature.

The Sherrer's formula[24,25] was applied for evaluating sizes of the gold nanoparticles on the basis one of the peaks in the diffractogram for different samples:

$$d = \frac{K\lambda}{\beta \cos\theta}$$

where K is the dimensionless shape factor, for cubic crystals it is $0.9 - 1$; λ is the X-ray wavelength, for Cu K_α: $\lambda = 1.54178$ Å; β is the line width at half the maximum intensity in radians, θ is the Bragg angle, and d is the size of nanoparticles in nm.

The Sherrer's formula is applicable to grains with sizes less than 100 nm. For an approximate assessment of the size of nanoparticles, the (111) interferential maximum was used. In this case $\theta = 38^{\circ}$. The calculations were carried out taking into account only instrumental broadening of β ($\approx 0.3^{\circ}$) without evaluation of the influence of crystal defects on the shape of the interferential maximum. The size of gold nanoparticles in the biomass of *Arthrobacter oxydans* 61B determined by this method is ≈ 22 nm. This result coincides with results obtained by other methods.
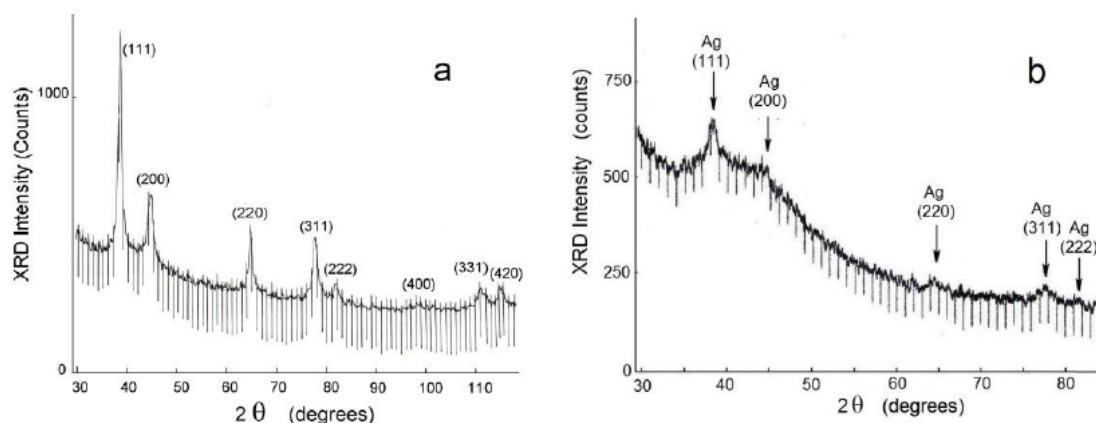
Figure 3. The XRD diffractogram for gold nanoparticles synthesized by *Arthrobacter oxydans* 61B treated with chloroauric acid for 12 days (a) and silver nanoparticles synthesized by *Spirulina platensis* treated with silver nitrate for 1 day (b).

Transmission electron microscopy (TEM) and scanning electron microscopy (SEM) were carried out for visualization and approximate assessment of sizes of the formed nanoparticles.
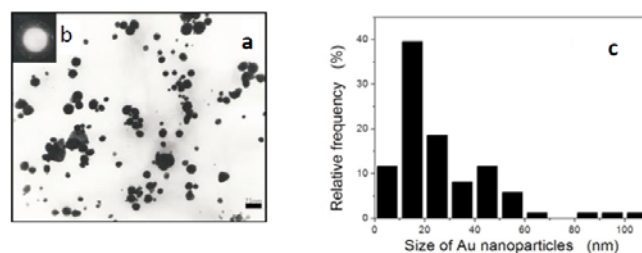

Figure 4. TEM micrographs recorded from drop-cast films of gold nanoparticles formed by the reaction of the $HAuCl_4$ solution with biomass *Thermoactinomycete spp.* 44Th after 6 days (a) the diffraction pattern of the selected area recorded from the gold nanoparticles (b) and Au nanoparticle sizes distribution (c).

Figure 4a shows the TEM image recorded from the drop-cast film of gold nanoparticles synthesized after reaction of the chloroauric acid solution with *Thermoactinomycete spp.* 44Th biomass for 6 days. The diffraction pattern of a selected area (Fig. 4b) corresponds to the face centered cubic (fcc) structure of gold nanoparticles. The particle size histogram obtained from this image (Figure 4c) shows that the size of the gold nanoparticles ranges from 5 nm to 60 nm with average 20 nm.

In Figure 5 the SEM images of silver nanoparticles formed on the surface of actinomycete *Streptomices spp.* 211A (a) and gold nanoparticles formed on the surface of actinomycete *Streptosporangium spp.* 94A (b) are shown. These SEM images illustrate that most of the particles are spherical and do not create big agglomerates.

In the EDAX spectra, the energy versus relative counts of the detected X-rays is presented. The spectra shown in Figure 6 proved the presence of silver nanoparticles in *Streptomices spp.* 211A biomass (a) and gold nanoparticles in *Arthrobacter globiformis* 151B biomass (b). The four peaks of Ag are observed for *Streptomyces spp.* 211A (Figure 6a). The signals from C, O, and P due to X-ray emission from proteins/enzymes existing in biomass are also

recorded. Several peaks of Au and the signals from C, O, K, P, and Ca are observed for *Arthrobacter globiformis* 151B (Figure 6b).
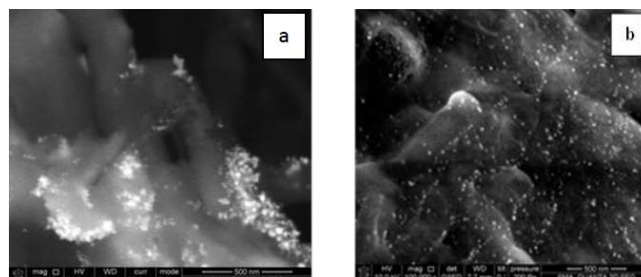

Figure 5. SEM image of silver nanoparticles formed on the surface of actinomycete *Streptomices spp.* 211A (a) and gold nanoparticles formed on the surface of actinomycete *Streptosporangium spp.* 94A (b).
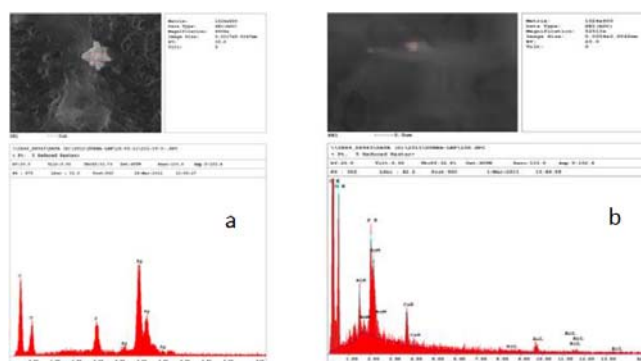

Figure 6. EDAX spectra recorded from *Streptomices spp.* 211A biomass with silver nanoparticles (a) and from *Arthrobacter globiformis* 151B biomass with gold nanoparticles (b).

To study the biosorption process on the bacterial cells at nanoparticles production the method of equilibrium dialysis and atomic absorption analysis were used. Concentrations of the metal adsorbed by bacteria in the solution at equilibrium dialysis obeyed the Freundlich equation that suggests the presence of heterogeneous sorption sites on bacteria surfaces, since the sorption depends on the nature and the composition of the cell wall.

The capacity of the adsorbent and the equilibrium relationship between adsorbent and adsorbate are described by Freundlich adsorption isotherms:

$$C_b = KC_t^n$$

where C_b is concentration of the metal adsorbed, C_t is equilibrium concentration of the metal ion in the solution, K and n are empirical constants, which may be characterized as the biosorption constant and sorptive capacity, respectively. The Figure 7 shows the Freundlich adsorption linearized isotherms for gold nanoparticles in *Streptomyces spp.* 211A biomass (A – for homogenized and B – for particulate homogenized).
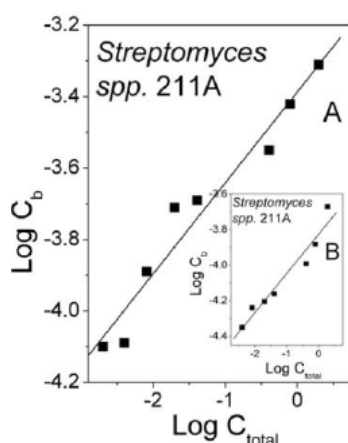

Figure 7. Freundlich adsorption isotherms for Au nanoparticles in *Streptomyces spp.* 211A biomass (A – for homogenized and B – for particulate homogenized).
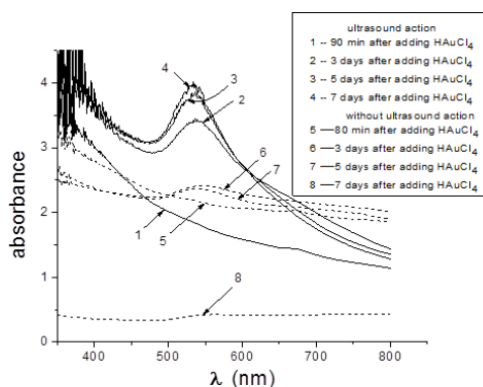

Figure 8. UV-vis spectra recorded as a function of time of reaction aqueous solution of HAuCl$_4$ with *Spirulina platensis* (after and without sonication).

To study the possibility of intensification of nanoparticle synthesis, the biomass of the blue-green alga *Spirulina platensis* with Au nanoparticles was subjected to sonication for 10 min using ultrasound generator at 35 kHz. The examination under an optical microscope shows that the biomass of *Spirulina platensis* disintegrated into small fragments. Then, for producing Au nanoparticles, an aqueous solution of the HAuCl$_4$ with a concentration of 10^{-3} M was added to the suspension. The results of measurements of UV-vis spectra for reaction at different time intervals are shown in Figure 8.

As it seen from Figure 8, the absorption peak of Au nanoparticles after the alga has been subjected to sonication is 4 times higher than without sonication. This can be caused by the increase of total surface of small bacterial fragments after sonication that also confirms the assumption about extracellular surface formation of nanoparticles.

In Figure 9a the TEM image of Au nanoparticles obtained upon subjection of the alga to the sonication is shown. The size distribution of these Au nanoparticles, given in Figure 9b shows that mean size of the Au nanoparticles is about 15 nm whereas without sonication this value was 25 nm [17]. Thus an intensification of the nanoparticles formation and reduction of their sizes take place at sonication.
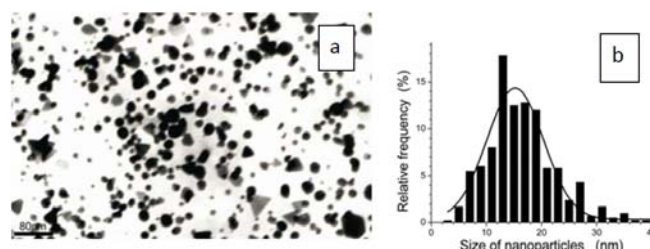

Figure 9. The TEM image of Au nanoparticles formed in the reaction of HAuCl$_4$ solution with *Spirulina platensis* biomass subjected to sonication (a) and Au nanoparticles size distribution histogram (b).
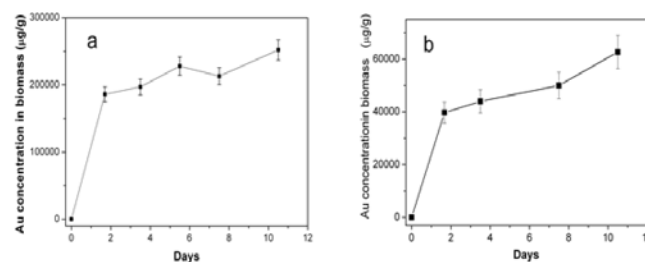

Figure 10. The total gold concentrations in biomass *Streptomyces spp.* 211A determined by NAA (a) and by AAS (b).

The analytical methods of neutron activation analysis (NAA) and atomic absorption spectrometry (AAS) were applied for determining total Au and Ag content in the biomass of studied bacteria. Examples of analytical determination (using NAA (a) and AAS (b)) of gold total concentrations in the bacterial biomass *Streptomyces spp.* 211A are given in Figure 10.

In all cases the analogical dynamic of total metal accumulation was observed: the concentration of metal increases rapidly in the first few hours and then increases slowly. In the first phase, the metal ions were mainly adsorbed onto the surface of bacterial cells extracellular. In the second phase, the metal ions were transported into the cells and accumulated intracellular.

NAA was also used to study multi-elemental content of the bacterial samples taking into account the possible medical application of the synthesized biomass with Au and Ag nanoparticles. The example is shown in Figure 11 for

Streptomyces glaucus 71MD. The NAA results show that the concentrations of some toxic elements in the obtained biomass do not exceed the permissible levels and synthesized materials with Au and Ag nanoparticles may be used for industrial, medical and pharmaceutical purposes.
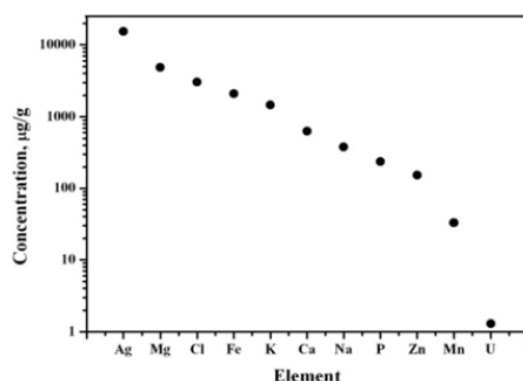

Figure 11. The distribution of elements in *Streptomyces glaucus* 71MD sample.

Conclusions

The performed investigations show that the studied microorganisms – the new strains of actinomycetes: Arthrobacter genera (*Arthrobacter globiformis* 151B and *Arthrobacter sp*.61B), extremophiles *Streptomyces spp.* 211A and *Streptomyces glaucus* 71MD, thermophiles *Thermoactinomycete spp.* 44Th and *Thermomonospora spp.* 67Th as well as the blue-green alga *Spirulina platensis* are able to produce gold and silver nanoparticles by interacting with 10^{-3} M aqueous solutions of chloroauric acid ($HAuCl_4$) and silver nitrate ($AgNO_3$).

The produced gold and silver nanoparticles formed by bacterial biomass are crystalline in nature and they are mainly produced extracellular. In general, they have the spherical shapes and sizes in the range of 5-60 nm with the average size in the range 15 – 35 nm for different bacterial strains.

The methods of UV-vis and XRD spectrometry, SEM with EDAX and TEM microscopy as well as atomic adsorption spectroscopy (AAS) and neutron activation analysis (NAA) are powerful for examining Au and Ag nanoparticles in bacterial biomass and characterizing mechanisms of their formation. The methods of equilibrium dialysis with AAS were successively used for study of surface biosorption process at formation of nanoparticles by tested microorganisms.

The performed investigations show that the studied microorganisms can be used for development of clean, simple, nontoxic and environmentally acceptable methods of synthesis gold and silver nanoparticles and have great potential in industry and medicine.

References

[1]Mohanpuria, P., Rana, N., Yadav, S. K., *J. Nanopart. Res.*, **2008**, *10*, 507-517.

[2]Bhattacharya, D. Gupta, R. K., *Crit. Rev. Biotechnol.*, **2005**, *25*, 199-204.

[3]Krumov, N., Perner–Nochta, I., Oder, S., Gotcheva, V., Angelov, A., Posten, C., *Chem. Eng. Technol.*, **2009**, *32*, 1026-1035.

[4]Mandal, D., Bolander, M. E., Mukhopadhyay, D., Sarkar, G., Mukherjee, P., *Appl. Microbiol. Biotechnol.*, **2006**, *69*, 485-492.

[5]Salata, O. V., *J. Nanobiotechnol.*, **2004**, *2*, DOI: 10.1186/1477-3155-2-3.

[6]Zang, L., Gu, F. X., Chan, J. M., Wang, A. Z., Langer, R. S., Farokhzad, O. C., *Clin. Pharm. Therap.*, **2008**, *83*, 761-769.

[7]Dykman, L. A., Khlebtsov, N. G., *Acta Naturae* **2011**, *3*, 34-55.

[8]Frontasyeva, M. V., Tsibakhashvili, N., Mosulishvili, L., Kirkesali, E. I., *Algae for the production of pharmaceuticals. In: Bioprocesses Sciences and Technology* (Ed. F. Columbus). New York: Nova Sci. Publ., **2010**, Ch. *5*, 119-142.

[9]Tsibakhashvili, N., Mosulishvili, L., Kirkesali, E., Murusidze, I., Frontasyeva, M. V., Pavlov, S. S., Zinicovscaia, I. I., Bode, P., van Meerten, Th. G., *J. Radioanal. Nucl. Chem.*, **2010**, *286,* 533-537.

[10]Tsibakhashvili, N., Murusidze, I., Kerkendjia, S., Kalabegishvili, T., Mosulishvili, L., Kirkesali, E., Holman, H.-Y., Frontasyeva, M. V., Gundorina S. F., *J. Radioanal. Nucl. Chem.*, 2008, 278, 565-569.

[11]Tsibakhashvili, N. Ya., Frontasyeva, M. V., Kirkesali, E. I., Aksenova, N. G., Kalabegishvili, T. L., Murusidze, I. G., Mosulishvili, L., M. Holman, H.-Y. N., *Anal. Chem.*, **2006**, *78*, 6285-6290.

[12]Mosulishvili, L. M., Kirkesali, E. I., Belokobilsky, A. I., Khizanishvili, A. I., Frontasyeva, M. V., Gundorina, S. F., Oprea, C. D., *J. Radioanal. Nucl. Chem.*, **2002**, *252*, 15-20.

[13]Mosulishvili, L. M., Frontasyeva, M. V., Pavlov, S. S., Belokobilsky, A. I., Kirkesali, E. I., Khizanishvili, A. I., Gundorina, S. F., *J. Pharm. Biomed. Anal.*, **2002**, *30*, 87-97.

[14]Tsibakhashvili, N. Y., Kirkesali, E. I., Pataraya, D. T., Gurielidze, M. A., Kalabegishvili, T. L., Gvarjaladze, D. N., Tsertsvadze, G. I., Frontasyeva, M. V., Zinicovscaia, I. I., Wakstein, M. S., Khakhanov, S. N., Shvindina, N. V., Shklover, V. Y., *Adv. Sci. Lett.*, **2011**, *4*, 3408-3417.

[15]Kalabegishvili, T. L., Kirkesali, E. I., Rcheulishvili, A. N., Ginturi, E. N., Murusidze, I. G., Pataraya, D. T., Gurielidze, M. A., Tsertsvadze, G. I., Gabunia, V. N., Lomidze, L. G., Gvarjaladze, D. N., Frontasyeva, M. V., Pavlov, S. S., Zinicovscaia, I. I., Raven, M. J., Seaga, N. M. F., Faanhof. A., *J. Mater. Sci. Eng. A*, **2012,** *2*, 164-173.

[16]Kalabegishvili, T., Murusidze, I., Kirkesali, E., Rcheulishvili, A., Ginturi, E., Gelagutashvili, E., Kuchava, N., Bagdavadze, N., Pataraya, D., Gurielidze, M., Tsertsvadze, G., Gabunia. V., *Nano Studies*, **2012**, *5*, 127-136.

[17]Kalabegishvili, T., Murusidze, I., Kirkesali, E., Rcheulishvili, A., Ginturi, E., Kuchava, N., Bagdavadze, N., Gelagutashvili, E., Frontasyeva, M. V., Zinicovscaia, I., Pavlov, S. S., Dmitriev, A. Y., *Ecol. Chem. Eng.,* **2013**, *20*, 621-631.

[18]Kalabegishvili, T. L., Murusidze, I. G., Kirkesali, E. I., Rcheulishvili, A. N., Ginturi, E. N., Gelagutashvili, E. S., Kuchava, N. E., Bagdavadze, N. V., Pataraya, D. T., Gurielidze, M. A., Holman, H.-Y., Frontasyeva, M. V., Zinicovscaia, I. I., Pavlov, S. S., Gritsyna, V. T., *J. Life Sci.*, **2013**, *7*, 110-122.

[19]Echlin, P., Goldstein, J., Joy, D., Lifshin, E., Liman, C., Michael, J., Newbury, D., Saver. L., *Scanning Electron Microscopy and X-ray Microanalysis.* New York: Kluver Academic/Plenum Publishers, **2003**.

[20]Frontasyeva, M. V., Pavlov. S. S., *REGATA experimental setup for air pollution studies.* In: *Problems of Modern Physics* (Eds. N. Sissakian, D. I. Trubetskov). Dubna, JINR, **1999**, 152-158.

[21]Dmitriev, A. Yu., Pavlov, S. S., *Particles Nuclei Lett.*, **2013**, *10*, 58-64.

[22]Underwood, S. Mulvaney, P., *Langmuir*, **1994**, *10*, 3427-3430

[23]Mie, G., *Ann. Phys*., **1908**, *25*, 377 − DOI: 10.1002/andp.1908 3300302.

[24]Cullity, B. D. Stock, R., *Elements of X-Ray Diffraction*. Prentice-Hall Inc., **2001**.

[25]Jenkins, R., Snyder, R. L., *Introduction to X-ray Powder Diffractometry*. John Wiley & Sons Inc., **1996**.